

Correlation dreams on a multi-configurational budget

By

Luke Bernard Roskop

A dissertation submitted to the graduate faculty
in partial fulfillment of the requirements for the degree of

DOCTOR OF PHILOSOPHY

Major: Physical Chemistry

Program of Study Committee:
Mark S. Gordon, Major Professor
James W. Evans
Monica H. Lamm
Patricia A. Thiel
Theresa L. Windus

Iowa State University

Ames, Iowa

2011

Copyright © Luke Bernard Roskop, 2011. All rights reserved.

To my mother

TABLE OF CONTENTS

ACKNOWLEDGMENTS	v
CHAPTER 1. GENERAL INTRODUCTION	1
General Overview	1
Dissertation Organization	1
Theoretical Background	2
References	14
CHAPTER 2. AN ORMAS-SCF STUDY OF SILICON (100) SURFACE CLUSTERS	17
Abstract	17
Introduction	17
Computational Methods	22
Results and Discussion	24
Conclusions	28
Acknowledgments	29
References	29
CHAPTER 3. QUASI-DEGENERATE SECOND-ORDER PERTURBATION THEORY FOR ORMAS-SCF REFERENCE FUNCTIONS	40
Abstract	40
Introduction	40
Method	44
Applications	54
Conclusions	60
Acknowledgments	62
References	62
CHAPTER 4. THE DIFFUSION OF GALLIUM ADATOMS ON THE Si(100)-2X1 RECONSTRUCTED SURFACE: AN MCSCF STUDY OF MOLECULAR SURFACE CLUSTERS	80
Abstract	80
Introduction	80
Computational Methods	84
Results and Discussion	86
Conclusions	97
Acknowledgments	99
References	99

CHAPTER 5. CAN KOHN-SHAM ORBITALS BE USED TO INTERPRET ELECTRONIC SPECTRA?	119
Abstract	119
Introduction	119
Excited state methods	120
Kohn-Sham orbital interpretations	123
Applications	124
Conclusions	128
Acknowledgments	130
References	130
 CHAPTER 6. SILICA MESOPOROUS MOLECULAR SIEVES AND THE FRAGMENT MOLECULAR ORBITAL METHOD	 138
Abstract	138
Introduction	138
Method	141
Results and Discussion	143
Conclusions	145
Acknowledgments	145
References	145
 CHAPTER 7. GENERAL CONCLUSIONS	 155

ACKNOWLEDGMENTS

First and foremost, I would like to thank my advisor Mark Gordon. I thank him for his patience, his instruction, and his friendship. His rigorous approach to science has been inspirational to me.

I thank the love of my life, Alyssa, for the support and encouragement she has given me. You are my best friend and rock.

I thank Ken Hanson, a true friend who has shown me the pleasure and importance of thinking outside of the box.

I thank my brother Nik, for showing me the humor in every situation and my brother Quincy, for teaching me how to take a break and live life.

Lastly, I thank my parents, Cheryl and David, for the support they have given me in every aspect of my life. Most importantly, for instilling in me a sense of honesty and humility that has shaped me into the individual I am today.

CHAPTER 1. GENERAL INTRODUCTION

1. General Overview

The field of quantum chemistry is generally concerned with the behavior of atomic, molecular, and crystalline systems. Over time, a variety of theoretical models have been developed to interpret chemical phenomena at this fundamental level. These models allow chemists to go beyond the limits of experiment and provide deeper insights into chemical behavior.

All theoretical models have specific strengths and weaknesses. For example, some methods are capable of treating systems composed of thousands of atoms, while others provide a high level of accuracy that can be applied to systems comprised of only a few atoms. Much of the development in quantum chemistry is directed toward the design of highly sophisticated theoretical models that require a practical amount of computational effort such that quantum computations can be performed on personal workstations.

2. Dissertation Organization

The present work contains six chapters, which are either in press, accepted, or in preparation for submission to the appropriate journals.

Chapter 2 describes an investigation of the morphology of the Si(100) surface, which is modeled using molecular clusters treated with the occupation restricted multiple active space (ORMAS) method. Chapter 3 describes the implementation of a quasi-degenerate second-order perturbation theory for ORMAS reference wavefunctions (ORMAS-PT). Chapter 4 describes an investigation into the diffusion of Ga on the Si(100) surface. Chapter 5 describes the relation between electronic molecular orbitals and excited state properties.

Chapter 6 describes an application of the fragment molecular orbital (FMO) method to a series of mesoporous silica nanoparticles.

3. Theoretical Background

The time-dependent Schrödinger equation¹ (Eq. 1) is the fundamental expression that describes the evolution of quantum systems. In Eq. 1: \hbar is Planck's constant over 2π , $i = \sqrt{-1}$, H is the Hamiltonian operator, and $\Psi(r,R,t)$ is a wavefunction. The wavefunction depends on time t and the electronic (nuclear) coordinates r (R).

$$i\hbar \frac{\partial}{\partial t} \Psi(r,R,t) = H\Psi(r,R,t) \quad (1)$$

The majority of applications in the field of quantum chemistry focus on stationary state solutions of the Schrödinger equation. Unlike the time-dependent Schrödinger equation, the time-independent analogue (Eq. 2) can be expressed as an eigenvalue problem.

$$H\Psi(r,R) = E\Psi(r,R) \quad (2)$$

The time-independent Schrödinger equation is a second-order differential equation that depends only on the nuclear and electronic degrees of freedom. The eigenfunction $[\Psi(r,R)]$ in Eq. 2 corresponds to a stationary state wavefunction that depends on the electronic (r) and nuclear coordinates (R). The associated eigenvalue (E) corresponds to the total energy of the quantum state described by the wavefunction.

The Hamiltonian operator H is expressed in atomic units as shown in Eq. 3, where: ∇_i^2 is the Laplacian of particle i , m_A is the mass of nucleus A , Z_A is the charge of nucleus A , r_i

represents the coordinates of electron i , and R_A represents the coordinates of nucleus A .

$$H = - \underbrace{\frac{1}{2} \sum_{i=1}^{\text{electrons}} \nabla_i^2}_{T_e} - \underbrace{\frac{1}{2} \sum_{A=1}^{\text{nuclei}} \frac{\nabla_A^2}{m_A}}_{T_n} + \underbrace{\sum_{A=1}^{\text{nuclei}} \sum_{i=1}^{\text{electrons}} \frac{Z_A}{|R_A - r_i|}}_{V_{en}} + \underbrace{\sum_{i>j}^{\text{electrons}} \frac{1}{|r_i - r_j|}}_{V_{ee}} + \underbrace{\sum_{A>B}^{\text{nuclei}} \frac{Z_A Z_B}{|R_A - R_B|}}_{V_{nn}} \quad (3)$$

Each component of the Hamiltonian operator is classified into one of five terms: the kinetic energy of electrons (T_e), the kinetic energy of nuclei (T_n), the electron-nuclear attraction (V_{en}), the electron-electron repulsion (V_{ee}), and the nucleus-nucleus repulsion (V_{nn}).

Relative to the electronic motion, the nuclei move at a much slower velocity, as they are roughly three orders of magnitude more massive than the electrons. This gives the impression that electrons exist in a static field of nuclei, indicating that the nuclear and electronic motions can be separated. One way to separate these interactions is by fixing the positions of the nuclei in space (eliminating the T_n term in Eq. 3) and treating the V_{nn} term as a constant, a procedure commonly referred to as the Born-Oppenheimer approximation.² Through the use of this approximation, the time-independent Schrödinger equation can be reduced to a second-order differential equation that depends on the electronic degrees of freedom only. The three terms in Eq. 3 that do not exclusively depend upon the nuclear coordinates (T_e , V_{en} , V_{ee}) comprise the electronic Hamiltonian H_{elec} (Eq. 4); however, H_{elec} depends parametrically on the nuclear coordinates. Solutions to the electronic Hamiltonian are represented as $\Psi(r)$ in Eq. 5.

$$H_{\text{elec}} = - \frac{1}{2} \sum_{i=1}^{\text{electrons}} \nabla_i^2 - \sum_{A=1}^{\text{nuclei}} \sum_{i=1}^{\text{electrons}} \frac{Z_A}{|R_A - r_i|} + \sum_{i>j}^{\text{electrons}} \frac{1}{|r_i - r_j|} \quad (4)$$

$$H_{\text{elec}} \Psi_{\text{elec}}(r) = E_{\text{elec}} \Psi_{\text{elec}}(r) \quad (5)$$

Within the Born-Oppenheimer approximation, E_{elec} corresponds to the total electronic energy of a molecule. The potential energy expression $U(R)$ requires the addition of a nuclear repulsion term to E_{elec} (Eq. 6).

$$U(R) = E_{\text{elec}} + \sum_{A>B}^{\text{nuclei}} \frac{Z_A Z_B}{|R_A - R_B|} \quad (6)$$

Since the nuclei are stationary, a classical point charge model can be used to treat the nuclear repulsion term. This gives rise to the concept of a potential energy surface (PES), a tool that describes how the energy of a system varies with the nuclear degrees of freedom.

The exact electronic wavefunction, $\Psi(r)$, is a highly complex function that depends on the coordinates of all electrons and nuclei. Since the kinetic energy (T_e) and electron-nuclear attraction (V_{en}) terms are additive with the electronic indices, it is reasonable to cast the electronic wavefunction in a form such that the electronic coordinates are separate. Unlike the T_e and V_{ne} terms, V_{ee} is not a function of a single electronic coordinate but is instead a function of a pairs of electronic coordinates (pair-wise additive). As a result, it is impossible to find solutions to H_{elec} in which the variables are separable. To avoid this problem, Hartree-Fock (HF) theory employs the mean field approximation³ to replace the two-electron repulsion term (V_{ee}) in Eq. 4 with a one-electron potential, $v^{\text{HF}}(1)$ (Eq. 7).

$$f(1) = -\frac{1}{2} \nabla_1^2 - \sum_{A=1}^{\text{nuclei}} \frac{Z_A}{|R_A - r_1|} + v^{\text{HF}}(1) \quad (7)$$

The $v^{\text{HF}}(1)$ potential accounts for the interaction of electron 1 with the effective field of all other electrons. $v^{\text{HF}}(1)$ leads to the one-electron Fock operator (Eq. 7), comprised of terms that are additive such that separation of variables is possible.

Since the Fock operator is a one-electron expression, an approximate wavefunction can be formed that is comprised of a separate function (φ_m) for each electron. These functions, called molecular spin-orbitals, are constructed as a linear combination of atomic orbitals χ_k (Eq. 8). In Eq. 8, m and k refer to the molecular and atomic orbital indices, respectively.

$$\varphi_m = \sum_k c_{km} \chi_k \quad (8)$$

The product of these molecular orbitals is referred to as a Hartree product Ψ_{HP} (Eq. 9), which is not the correct form of a wavefunction.

$$\Psi_{\text{HP}} = \varphi_1 \varphi_2 \varphi_3 \dots \varphi_N \quad (9)$$

Since an electron is a fermion, the sign of a wavefunction must change when the coordinates of any two electrons are exchanged. In order to comply with this anti-symmetry principle, the Hartree product must be antisymmetrized in order to construct a proper HF wavefunction. A HF wavefunction can be expressed in the compact form as a Slater determinant⁴ (Eq. 10).

$$\Psi_{\text{HF}} = |\varphi_1 \varphi_2 \varphi_3 \dots \varphi_N| \quad (10)$$

The HF approximation is the central *ab initio* approach to treatments of electronic structure in atomic and molecular systems. Because the HF potential in Eq. (7) depends on

knowledge of the HF orbitals, the HF equations must be solved iteratively for the orbitals and the orbital energies. The iterative process is called the self-consistent field (SCF) equations. The dependence of the HF potential on the HF orbitals is seen from the HF equations (Eqs. 11-13). In Eq. 11, $h(1)$ represents a one-electron operator that accounts for the kinetic energy of the electrons and electron-nuclear attraction, $J_b(1)$ is the coulomb operator (Eq. 12), and $K_b(1)$ is the exchange operator (Eq. 13).

$$f(1) = h(1) + v^{\text{HF}}(1) = h(1) + \sum_b J_b(1) + \sum_b K_b(1) \quad (11)$$

$$J_b(1)\varphi_a(1) = \int dx_2 \varphi_b^*(1) r_{12}^{-1} \varphi_b(1) \varphi_a(1) \quad (12)$$

$$K_b(1)\varphi_a(1) = \int dx_2 \varphi_b^*(1) r_{12}^{-1} \varphi_a(1) \varphi_b(1) \quad (13)$$

The HF equations define the energy of orbital φ_a as ε_a (Eq. 14)

$$f(1)\varphi_a(1) = \varepsilon_a \varphi_a(1) \quad (14)$$

Solutions to the HF SCF equations correspond to an optimal set of molecular orbitals that minimize the energy of a molecular system, by making use of the variational principle. This means that the calculated energy of any HF wavefunction, E_{HF} , is guaranteed to be an upper bound to the exact non-relativistic energy E_{exact} (Eq. 15).

$$E_{\text{exact}} \leq E_{\text{HF}} \quad (15)$$

Although HF theory can determine a wavefunction for complex multi-electron systems, the wavefunction may not be suitable to describe certain chemical processes (i.e. the dissociation of a chemical bond). An example of the breakdown of the HF method is

provided by the HF PES of H_2 . The HF dissociation curve for H_2 does not proceed to the correct limit. The reason for this failure is that HF theory does not correlate the motions of electrons with one another. This fact has led to the development of many post-HF methods to provide more reliable potential energy surfaces than HF. The correlation energy (Eq. 16) is defined as the difference between the energy expectation value of the exact non-relativistic (E_{exact}) and HF (E_{HF}) solutions.

$$E_{\text{corr}} = E_{\text{exact}} - E_{\text{HF}} \quad (16)$$

The HF wavefunction (Ψ_{HF}) provides the lowest variationally bound energy expectation value a single configuration can provide. To form a better approximation to the exact non-relativistic wavefunction, a natural extension of HF is to expand the wavefunction in a basis of configurations. In what is known as configuration interaction (CI), an approximate wavefunction (Φ_{CI}) is expanded within a finite basis of determinants or spin-adapted configuration state functions. The HF reference determinant (Ψ_{HF}) weighted by the appropriate CI coefficient (C_{HF}) is the leading term in this expansion (Eq. 17).

$$\Phi_{\text{CI}} = C_{\text{HF}} \Psi_{\text{HF}} + \sum_S C_S \Psi_S + \sum_D C_D \Psi_D + \dots \quad (17)$$

Each additional term corresponds to a configuration that is classified as a single (Ψ_S, C_S), double (Ψ_D, C_D), or a higher excitation from occupied to unoccupied MOs.

In the limit of CI (full CI), the wavefunction is expanded within a set of determinants that correspond to all possible excitations from occupied to unoccupied MOs. This results in exact, non-relativistic solutions (within the Born-Oppenheimer approximation and the atomic

basis set) to the time-independent Schrödinger equation. For practical reasons, applications of CI usually involve a truncated expansion.

In addition to ground state properties, CI also has the flexibility to explicitly describe excited states. The simplest level of theory in CI used for excited state properties is referred to as CI +single excitations (CIS). CIS truncates the CI expansion after the first summation in Eq. 17. The reliability of the CI method can be systematically improved if configurations that correspond to higher order excitations are used to expand Φ_{CI} . However, there is a concomitant increase in computational expense associated with these improvements, and in general a balance must be struck between the desired level of accuracy and computational requirements.

A wavefunction that corresponds to a truncated CI expansion is neither size consistent nor size extensive. Size inconsistency is seen from the disagreement in total energy between: **1)** two infinitely separated H_2 monomers and **2)** twice the energy of a single H_2 monomer. A method is size extensive if the energy calculated scales linearly with the number of particles. Aside from these shortcomings, CI has proven to be an effective tool in the recovery of correlation energy such that it is frequently used as a benchmark for other post-HF methods.

Many-body perturbation theory (MBPT) is a popular alternative to CI that considers correlation effects with better computational scaling. The conventional approach to n^{th} -order MBPT treats the exact non-relativistic Hamiltonian H (Eq. 18) as a perturbed independent particle Hamiltonian H_0 , with the energy and wavefunction expanded in n orders of the perturbation V (Eqs. 19-20).^{5,6}

$$H = H_0 + \lambda V \tag{18}$$

$$\Psi_{\text{MPn}} = \Psi_0 + \sum_{i=1}^n \lambda^i \Psi_i \quad (19)$$

$$E_{\text{MPn}} = E_0 + \sum_{i=1}^n \lambda^i E_i \quad (20)$$

The intent of n^{th} -order perturbation theory is to systematically include higher order corrections to better approximate the exact energy and wavefunction. In particular, the formalism of n^{th} -order Møller and Plesset (MPn) theory⁷ has found great importance as a reliable, size consistent, and size extensive method.

MP2 ($n = 2$) accounts for $\sim 80\text{-}90\%$ of the total correlation energy, with the total energy though second-order, $E(\text{MP2})$, computed by Eq. 21.

$$E(\text{MP2}) = E_{\text{HF}} + \sum_{\text{D}} \frac{|\langle \Psi_{\text{D}} | V | \Psi_{\text{HF}} \rangle|^2}{E_{\text{D}}^{(0)} - E_{\text{HF}}^{(0)}} \quad (21)$$

With respect to the Hartree-Fock determinant (Ψ_{HF}), the summation in Eq. 21 runs over all double excitations from occupied to unoccupied orbitals (Ψ_{D}). The denominators correspond to the zeroth-order energy differences between each doubly excited determinant (Ψ_{D}) and the HF determinant. Although higher order energy corrections are possible (MP3, MP4...), they can lead to unpredictable behavior since the MPn series is sometimes not convergent.

From system to system, the reliability of perturbation theory depends on how well the HF wavefunction approximates the exact non-relativistic wavefunction. In other words, the perturbation must be small for perturbation theory to provide reliable results. If the HF reference wavefunction is a poor description, convergence of the wavefunction and energy expansion (Eqs. 19-20) can be erratic. Compared to HF theory, the multi-configuration self-

consistent field (MCSCF) method provides a better approximation to the exact non-relativistic wavefunction. The reliability of the MCSCF approach originates from its inclusion of non-dynamic correlation effects. Non-dynamic correlation effects are important in chemical systems that exhibit near degeneracies, for example, in the vicinity of conical intersections, during bond breaking, in radical chemistry, electronic excited states, and unsaturated transition metal compounds.

Like CI, the MCSCF wavefunction is expanded within a subset of determinants. These determinants are constructed from a set of active orbitals and electrons that are deemed most important for the chemical behavior under examination. Unlike CI, the orbitals that comprise each determinant in the MCSCF expansion are re-optimized within the CI wavefunction. Since MCSCF is rooted in the CI method, it has the ability to treat excited state properties. The most common implementation of MCSCF is the complete active space self-consistent field (CASSCF) or full optimized reaction space (FORS).⁸ CASSCF/FORS employ a complete active space (CAS), which corresponds to a full-CI within a subset of active orbitals and electrons.

All occupied orbitals in HF theory contain either one or two electrons. Unlike HF theory, MCSCF permits non-integer orbital occupancies in general, and nonzero occupancies of antibonding orbitals in particular. Due to the flexibility of MCSCF wavefunctions, the ground state energy expectation value is lower than HF theory. The difference between the HF and MCSCF ground state energies is referred to as the non-dynamic correlation energy.

Since MCSCF captures only non-dynamic correlation effects, it is not suited to predict experimental observations. This has led to the development of a variety of multi-reference perturbation theory (MRPT) methods. Compared to single reference MP2, MRPT is more

reliable since the underlying MCSCF wavefunction is a better approximation to the exact wavefunction (smaller perturbation). It is also possible to apply MRPT to more than one state (simultaneously) as in the multi-configuration quasi-degenerate perturbation theory (MCQDPT) method.⁹

Although CASSCF and MRPT are highly reliable methods, they are computationally demanding as they scale with the factorial of the number of active orbitals. The occupation restricted multiple active space (ORMAS)¹⁰ method is an efficient alternative as it includes only the most important determinants in the MCSCF-CI expansion. Determinants in the ORMAS-CI expansion are specified through user-defined restrictions on the minimum and maximum electron occupation numbers for each user-defined active orbital subspace. If the CAS is appropriately partitioned with ORMAS, one can expect a high level of accuracy, while many of the ineffective electronic configurations (“*deadwood*”¹¹) are neglected. Thus, ORMAS has the ability to retain only the most important configurations in a CI space.

All of the theoretical methods presented above correspond to *ab initio* wavefunction methods. A popular alternative to wavefunction methods is first principles density functional theory (DFT).¹² Instead of a wavefunction, DFT relies on the electronic density $[\rho(x,y,z)]$ as the fundamental quantity for computing atomic and molecular properties. Regardless of the number of electrons, the electronic density $[\rho(x,y,z)]$ is dependent upon three variables such that DFT has a computational scaling similar to HF theory. As a result, DFT has found a niche as an efficient alternative to *ab initio* wavefunction methods in the study of large, highly correlated systems.

Modern implementations of DFT almost exclusively employ the Kohn-Sham formalism.¹³ The use of the one-electron Kohn-Sham operator (h^{KS}), defined in Eq. 22,

allows the electrons to be treated as independent particles moving in an external potential of the other electrons.

$$h^{KS} = -\frac{1}{2}\nabla^2 + \sum_A^{\text{nuclei}} \frac{Z_A}{|\mathbf{r}-\mathbf{r}_A|} + \int \frac{\rho(\mathbf{r}')}{|\mathbf{r}-\mathbf{r}'|} d\mathbf{r}' + V_{xc}(\mathbf{r}) \quad (22)$$

Unlike HF, correlation effects are included via an exchange-correlation functional, $V_{xc}(\mathbf{r})$. If the exact exchange-correlation functional were known, DFT would provide exact results. Unfortunately, the exact functional remains unknown, a fact that has led to a plethora of empirically fitted substitutes.

The time dependent version of DFT (TDDFT) allows for the determination of excited state properties. Compared to *ab initio* excited state methods, the relatively low computational scaling of TDDFT has made it very popular method for computing excited state properties. TDDFT involves the treatment of the eigenvalue problem shown by Eq. 23, where the left-most term is the response matrix, ω represents the excitation energies, and \mathbf{X} (\mathbf{Y}) is a vector that denotes excitation (de-excitation) coefficients.

$$\begin{bmatrix} \mathbf{A} & \mathbf{B} \\ \mathbf{B} & \mathbf{A} \end{bmatrix} \begin{bmatrix} \mathbf{X} \\ \mathbf{Y} \end{bmatrix} = \omega \begin{bmatrix} 1 & 0 \\ 0 & -1 \end{bmatrix} \begin{bmatrix} \mathbf{X} \\ \mathbf{Y} \end{bmatrix} \quad (23)$$

The response matrix is comprised of matrices \mathbf{A} and \mathbf{B} , whose elements are displayed in Eqs. 24-25.

$$A_{ia,jb} = \delta_{ij}\delta_{ab}(\epsilon_a - \epsilon_i) + 2(\text{ia}|\text{jb}) + (\text{ia}|f_{xc}|\text{jb}) \quad (24)$$

$$B_{ia,jb} = 2(\text{ia}|\text{jb}) + (\text{ia}|f_{xc}|\text{jb}) \quad (25)$$

The leading term on the diagonal of matrix **A** (Eq. 24) is the orbital energy difference between occupied orbital ‘i’ and unoccupied orbital ‘a’. The remaining terms in **A** (and **B**) correspond to two-electron integrals between occupied MOs i,j and unoccupied MOs a,b.

One simplification that is routinely applied to the TDDFT eigenvalue problem is the Tamm-Dancoff approximation (TDA).¹⁴ The TDA reduces the complexity of Eq. 23 by neglect of the **Y** component in the solution, i.e. **Y**=0, and hence neglect of the **B** matrices (Eq. 26).

$$\mathbf{AX} = \omega\mathbf{X} \quad (26)$$

It has been observed that TDA-TDDFT can often perform as well as TDDFT for excited states, especially those that have significant charge transfer or Rydberg character.¹⁵

Although the electronic structure methods presented above are commonly employed to explain chemical phenomena, they are practical for systems comprised of a modest number of heavy atoms (~ 100 heavy atoms). If there is a desire to examine a larger system, one will typically examine just the region of the system that is the most chemically important. In order to efficiently treat large molecular systems on the order of 10^4 - 10^5 atoms with only quantum mechanics, fragmentation methods provide a practical approach. Over the years, several fragmentation methods have been developed in an effort to treat such large molecular systems.^{16,17,18,19,20} In particular, the fragment molecular orbital (FMO) method has shown great promise for proteins, silicon nanowires, and zeolite materials.²¹

In the FMO method, a molecular system of interest is split into fragments, which are referred to as monomers. A QM calculation is then performed for each monomer in a

Coulomb field constructed from all other monomers. As the Coulomb field reflects the total density, the monomers are iterated until the system has converged to self-consistency. Since the sum of all monomer energies is a poor estimate of the true energy, it is necessary to include two-body (dimer) corrections. The dimer corrections are also computed in the Coulomb field of the remaining (n-2), but the dimers are not iterated to self-consistency. For increased accuracy, one can compute higher order corrections such as three-body (trimer) interactions in a similar manner. Eq. 27 is used to determine the total energy of a system treated with FMO. In Eq. 27: E_I is the monomer energy, E_{IJ} is the dimer energy, and E_{IJK} is the trimer energy.

$$E^{\text{FMO}} = \sum_I E_I + \sum_{I>J}^N (E_{IJ} - E_I - E_J) + \sum_{I>J>K}^N [(E_{IJK} - E_I - E_J - E_K) - (E_{IJ} - E_I - E_J) - (E_{JK} - E_J - E_K) - (E_{KI} - E_K - E_I)] + \dots \quad (27)$$

References

- ¹E. Schrödinger, Ann. Phys **79**, 361 (1926). E. Schrödinger, Ann. Phys **79**, 489 (1926). E. Schrödinger, Ann. Phys **79**, 734 (1926). E. Schrödinger, Ann. Phys **80**, 437 (1926). E. Schrödinger, Ann. Phys **81**, 109 (1926). E. Schrödinger, Die Naturwissenschaften **14**, 664 (1926).
- ²M. Born, R. Oppenheimer, Ann. Phys. **84**, 457 (1927).
- ³D. R. Hartree, Proc. Cambridge Philos. Soc. **24**, 89 (1928). D. R. Hartree, Proc. Cambridge Philos. Soc. **24**, 111 (1928). D. R. Hartree, Proc. Cambridge Philos. Soc. **24**, 426 (1928). V. Fock, Z. Phys. **61**, 126 (1930). V. Fock, Z. Phys. **62**, 795 (1930).

- ⁴J. C. Slater, Phys. Rev. **34**, 1293 (1929).
- ⁵J. A. Pople, S. Binkley, R. Seeger, Int. J. Quant. Chem. **10**, 1 (1976).
- ⁶P. O. Löwdin, J. Chem. Phys. **19**, 1396 (1951).
- ⁷Møller C.; Plesset M. S. Physical Review, 1934, **46**, 618. Bartlett R. J. *Annu. Rev. Phys. Chem.* 1982, **32**, 359.
- ⁸P. Seigbahn, A. Heiberg, B. Roos, B. Levy, Phys. Scr. **21**, 323 (1980). K. Ruedenberg, K. R. Sundberg, *Quantum Science* (J-L. Calais, O. Goscinski, J. Lindenberg, Y. Öhrn, Eds.) pp. 505-515 (Plenum Publ. Co., New York, 1976).
- ⁹H. Nakano, J. Chem. Phys. **99**, 7983 (1993). H. Nakano, Chem. Phys. Lett. **207**, 372 (1993).
- ¹⁰J. Ivanic, J. Chem. Phys. **119**, 9364 (2003).
- ¹¹Ivanic J.; Ruedenberg K. *Theor. Chem. Acc.* 2001, **106**, 339.
- ¹²Hohenberg P.; Kohn W. *Phys. Rev.* 1964, **136**, B864.
- ¹³Kohn W.; Sham L. J. *Phys. Rev.* 1965, **140**, A1133.
- ¹⁴Tamm I. *Journal of Physics-USSR* 1945, **9**, 449. Dancoff S. M. *Physical Review* 1950, **78**, 382.
- ¹⁵Wang Y.-L.; Wu G.-S. *Int. J. Quant. Chem.* 2008, **108**, 430.
- ¹⁶J. Gao, J. Phys. Chem. B **101**, 657 (1997). J. Gao, J. Chem. Phys. **109**, 2346 (1998). W. Xie, and J. Gao, J. Chem. Theory Comput. **3**, 1890 (2007).
- ¹⁷W. Yang, T.-S. Lee, J. Chem. Phys. **103**, 5674 (1995). T. Akama, M. Kobayashi, H. Nakai J. Comput. Chem. **28**, 2003 (2007). T. Akama, A. Fujii, M. Kobayashi, H. Nakai, Mol. Phys. **105**, 2799 (2007).
- ¹⁸V. Deev, M. A. Collins, J. Chem. Phys. **122**, 154102 (2005). M. A. Collins, V. A. Deev, J. Chem. Phys. **125**, 104104 (2006). M. A. Collins, J. Chem. Phys. **127**, 024104 (2007).

¹⁹D. W. Zhang, J. Z. H. Zhang, J. Chem. Phys. **119**, 3599 (2003).

²⁰S. R. Gadre, R. N. Shirsat, A. C. Limaye, J. Phys. Chem. **98**, 9165 (1994).

[KEM-1] Huang, L. L.; Massa, L.; Karle, J. *Int. J. Quantum Chem.*, **103**, 808, (2005).

²¹K. Kitaura, E. Ikeo, T. Asada, T. Nakano, M. Uebayasi, Chem. Phys. Lett. **313**, 701 (1999).

D.G. Fedorov, K. Kitaura, J. Chem. Phys. **120**, 6832 (2004). D. G. Fedorov, K. Kitaura, J.

Phys. Chem. A **111**, 6904 (2007). D. G. Fedorov, K. Kitaura, in: E. B. Starikov, J. P. Lewis,

S.Tanaka (Eds.), *Modern Methods for Theoretical Physical Chemistry and Biopolymers*,

Elsevier, Amsterdam, 2006, p. 3. D. G. Fedorov, D. G. Federov, J. H. Jensen, R. C. Deka, K.

Kitaura, J. Phys. Chem. A **112**, 11808 (2008). P. V. Avramov, J. H. Jensen, K. Kitaura,

Chem. Phys. Lett. **477**, 169 (2009). D. G. Fedorov, K. Kitaura (Eds.), *The Fragment*

Molecular Orbital Method: Practical Applications to Large Molecular Systems, CRC Press,

Boca Raton, FL, 2009.

CHAPTER 2. AN ORMAS-SCF STUDY OF SILICON(100) SURFACE CLUSTERS

A paper published in The Journal of Physical Chemistry A

Luke Roskop and Mark S. Gordon

An occupation restricted multiple active space (ORMAS) study of clusters that represent the silicon(100) surface (up to nine surface dimers) is discussed. The accuracy of three different active orbital ORMAS partition schemes for Si(100) surface clusters are compared. In addition to ORMAS-SCF calculations, generalized valence bond-perfect pairing (GVB-PP) properties are generated for comparison purposes. The ability of ORMAS to generate a reliable multi-configurational zeroth order wavefunction is systematically tested and when possible is compared to the full complete active space self-consistent field (CASSCF) method. This provides good benchmarks for the accuracy of ORMAS compared to CASSCF. It is demonstrated that ORMAS consistently provides a high degree of accuracy with a significantly reduced computational effort relative to a CASSCF calculation. For the largest cluster, for which a full CASSCF calculation is not possible, ORMAS predicts that the Si(100) surface dimers are symmetric.

1. Introduction

For some time it has been understood that crystalline surfaces promise to play a crucial role as a support structure for future nanodevices and organic functionalization.^{1,2} These applications will undoubtedly call for a deeper understanding regarding the electronic structure on a variety of surfaces. One such system relevant to this work is the Si(100) surface. It was first suggested through low energy electron diffraction (LEED) experiments that the reconstructed Si(100) surface is composed of rows of dimerized Si atoms.³ These

surface dimers are highly reactive to the adsorption of adatoms/molecules resulting largely from the diradical nature of the reconstructed surface dimers. Still more interesting to some is the theoretical and experimental controversy^{4,5,6} regarding whether the ground state Si(100) surface dimers are buckled^{7,8} or symmetric.^{9,10} Consequently, the computational treatment of this material is not a trivial matter and the necessity for reliable, cost effective surface methods is critical. Geometry searches performed at high levels of theory (coupled cluster theory with single, double, and perturbative triple excitations (CCSD(T)) and multi-reference second order perturbation theory (MRPT2)) confirm that the Si₉H₁₂ (single dimer) cluster ground state structure is symmetric (not buckled).¹¹ For larger surface models, it has been argued through the use of diffusion Monte Carlo (DMC) and quantum Monte Carlo (QMC) methodologies that dynamic correlation significantly influences surface dimer symmetry.^{12,13,14} These DMC simulations examined structures obtained with plane wave density functional theory (DFT). It was found that the asymmetric (buckled) structures are minima on the ground state potential energy surface (PES). A conflicting study demonstrated using MRPT2 energies on the CASSCF (complete active space self-consistent field) PES that symmetric structures are the true minima.¹⁵ The origin of this discrepancy may be attributed in part to the reference geometries that were employed, since DFT favors buckling and CASSCF prefers the symmetric structure.

The choice of reliable Si(100) surface methods requires a careful consideration of the surface dimers formed in the course of surface reconstruction. As pointed out by Redondo and Goddard,¹⁶ a single determinant wave function is not appropriate for describing these dimer bonds since they are not truly closed shell species. Rather, the surface dimers exhibit significant diradical character. Indications of multi-determinant treatments are negative π^*

RHF (restricted Hartree-Fock) singlet orbital energies and calculated Si dimer bond lengths ($\sim 2.30\text{\AA}$) that are between those of a single ($\sim 2.39\text{\AA}$) and double ($\sim 2.19\text{\AA}$) silicon-silicon bond.¹⁷ Two suitable methods for constructing appropriate zeroth order wave functions for these surface clusters are multi-configurational self-consistent field (MCSCF)^{18,19} and generalized valence bond-perfect pairing (GVB-PP).²⁰

Both MCSCF and GVB-PP possess the flexibility in the wavefunction, due to the incorporation of multiple electronic configurations, thereby permitting non-integer orbital occupancies in general, and nonzero occupancies of antibonding orbitals in particular. This is not possible in single determinant methods, such as HF or DFT. For HF and DFT the natural orbital occupation number (NOON) for an occupied molecular orbital (MO) is always 2 (doubly occupied MO) or 1 (singly occupied MO), while the NOON for an unoccupied MO is 0. For multi-configuration wavefunctions, NOONs need not be integers. A useful measure of multi-configuration character is the set of natural orbital occupation numbers.²¹ Indeed, a NOON that is significantly smaller than 2 for a supposedly doubly occupied orbital or a NOON that is significantly larger than 0 for a supposedly unoccupied orbital is a good indicator that a multi-configuration description is needed. For dimers on the Si(100) surface, the NOONs for the $\pi(\pi^*)$ orbitals are ~ 1.66 (0.33), thereby indicating significant diradical character and the need for a multi-configuration description.

The most rigorous MCSCF method available is the full optimized reactive space (FORS)^{22,23} or CASSCF.^{24,25,26} FORS/CASSCF active spaces are typically limited to the configurational mixing of 16 electrons in 16 orbitals (16,16), since the number of determinants (or configuration state functions) scale factorially. For the Si(100) surface, capturing the majority of dimer interactions for accurate reaction models, and minimizing

“edge effects”, may require large sized clusters (as many as 9 dimers or more). Practical concerns then arise dealing with model size since large surface clusters would demand impractically large active spaces. So, one quickly reaches the limitations of the CASSCF method in applications to the Si(100) surface, and is forced to settle for a truncated (perhaps less accurate) model.

Over the past 25 years, developments in approximate FORS/CASSCF methods have resulted in several alternatives, including the restricted active space self-consistent field (RASSCF),²⁷ quasi-complete active space (QCAS),²⁸ local methods such as the multi-reference weak pairs local configuration interaction²⁹ and the local configuration interaction method of Saebo and Pulay,³⁰ internally contracted multiconfigurational-reference configuration interaction (CI) method,³¹ and occupation restricted multiple active space (ORMAS).³²

RASSCF divides a complete active space (CAS) into three orbital subspaces (RAS1, RAS2, RAS3) in which all RAS1 orbitals are doubly filled and all RAS3 orbitals are unoccupied in the HF reference. The RAS2 subspace is a mixture of occupied and unoccupied orbitals. If needed, RASSCF can consider just two of the orbital subspaces. The allowed number of holes and particles in each subspace are user defined as follows: RAS1 excites 0,1,2,...,n electrons into RAS2 and RAS3 while RAS3 can accept 0,1,2,...,m electrons from RAS1 and RAS2.

QCAS divides a CAS space into any number of orbital subspaces such that each subspace itself is a CAS. The configurations are determined as products of the configurations generated from each of the orbital subspaces. In contrast to RASSCF, QCAS allows for any number of subspaces between which electrons are not permitted to excite.

Local CI methods rely on the behavior that localized orbitals separated by large distances are weakly correlated. Based on this, the CI space is reduced through elimination of configurations that result from simultaneous excitations between localized orbitals that are largely separated. The novel approach of ORMAS reduces the complexity of a computationally prohibitive CI space through greater flexibility in partitioning than RASSCF and QCAS. The determinants included in the ORMAS-CI expansion are specified through user-defined restrictions on the minimum and maximum electron occupation numbers for each user-defined orbital subspace. Using ORMAS to appropriately partition a CAS, one can eliminate many ineffective electronic configurations (“*deadwood*”³³) that contribute negligibly to the molecular energy. In this sense, the process has an analogous effect to that of the pre-screening of two-electron integrals. Thus, ORMAS has the ability to retain only the most important configurations in a CI space.

The determinants in an ORMAS calculation are selected by the (user-defined) minimum and maximum electron occupations imposed on each orbital subspace. As an example, consider a pair of Si-Si dimers on the Si(100) surface. A possible active space for such a system is a CAS(4,4) space, corresponding to two π, π^* orbital sets, one set for each dimer (36 determinants). This CAS(4,4) orbital space could be divided into two π, π^* (2,2) subspaces, one for each dimer while imposing minimum (maximum) electron occupation numbers of 2 (2) for each subspace (18 determinants). This means that in any one of the determinants used in the ORMAS-CI expansion, there will never exist one in which there are more or less than two electrons in each orbital subspace. This smaller CI space will increase the error compared to the full CAS, but if the partitioning is carried out appropriately, this

error can be negligible. If necessary, one can systematically include (at a cost) inter-subspace excitations until the desired property converges.

The present work presents a systematic test of the ORMAS method by characterizing Si(100) surface clusters of increasing size. This will demonstrate the utility of the ORMAS method to significantly expand the effective MCSCF active space. It will also provide a more extensive multi-reference treatment of this surface than has heretofore been possible.

2. Computational Methods

The accuracy of an ORMAS calculation depends on both the grouping of active orbitals into subspaces and the minimum/maximum electron occupancies imposed on each subspace. This partitioning relies on chemical intuition and on a series of tests that should be conducted to determine the essential configurations that one needs in the ORMAS wave function. The CASSCF analysis of one-, two- and three- Si-Si dimer clusters shown in Table 1 demonstrates that the natural orbital occupation numbers (NOON) of the π/π^* orbital pair remain constant as the cluster size increases. This means that in the MCSCF wave function, the surface dimers are only weakly coupled to one another.

In view of the weak dimer-dimer interactions, one can imagine three possibilities for grouping the active orbitals for a Si(100) surface cluster containing more than one dimer (summarized in Table 2). The key orbitals of each dimer, the Si-Si π and π^* orbitals and the corresponding σ and σ^* orbitals are shown in Figure 1. The first two schemes in Table 2 involve grouping the orbitals of each surface dimer into their own subspaces (number of subspaces = number of dimers) with scheme 1 involving the π and π^* orbitals only. The third possibility (scheme 3) further subdivides the orbital subspaces of scheme 2 into π - and σ -

spaces (number of subspaces = $2 \times (\text{number of dimers})$). All orbital groupings set the minimum and maximum electron occupation restrictions for each subspace to be identical (minimum = maximum).

In the present work, two (Figure 2a, 3a), three (Figure 3c), four (Figure 2b, 3b), five (Figure 3d, 3e) and nine (Figure 3f) dimer clusters are used to model the Si(100) surface. Since small Si(100) cluster calculations fail to capture effects of the bulk crystalline surface, the mechanically embedded quantum mechanics/molecular mechanics (QM/MM) method surface integrated molecular orbital molecular mechanics (SIMOMM³⁴) is employed using the MM3 force field parameters.³⁵ As the cluster models studied here can reach larger than 100 atoms, the Stevens-Basch-Krauss-Jasien-Cundari (SBKJC) effective core potentials (ECP) augmented with a set of d polarization functions (SBKJC ECP(d))³⁶ are used in this investigation. All active space orbitals are selected from a localized set of RHF orbitals determined using the Boys orbital localization procedure.³⁷ Symmetry is not imposed with ORMAS calculations since orbital localization breaks this property.

Setting CASSCF as the reference, the energy errors, NOON values, Si-Si dimer bond lengths and number of determinants are compared to the results obtained by ORMAS and GVB-PP. All reported properties for each method correspond to optimized geometries at their respective levels of theory (CASSCF, ORMAS or GVB-PP). Since the computational effort required to examine the nine-dimer cluster with CASSCF is prohibitive, ORMAS properties are compared only to GVB-PP. Due to the computational expense associated with calculating the Hessian for larger clusters, dimer buckling mode frequencies are examined for the smallest model (two-dimer) system only. ORMAS and CASSCF analytic Hessians³⁸ are used for the full QM cluster models while only semi-numerical Hessians are available for

the hybrid QM/MM SIMOMM models. All calculations are performed with the GAMESS³⁹ electronic structure code.

3. Results and Discussion

CASSCF, ORMAS and GVB-PP properties corresponding to the two-dimer Si(100) QM cluster (Figure 2a) are shown in Table 3 (top). The smaller ORMAS(4,4) orbital partition $[2(\pi\pi^*)^2]$ uses half as many determinants as the full CASSCF calculation, with only minor errors in the total energy and the dimer bond lengths (≤ 0.14 mH and ~ 0.01 Å, respectively, relative to the full CASSCF). The close agreement between CASSCF and ORMAS natural orbital occupation numbers (NOON) reinforces the notion that the surface dimers are weakly interacting with one another in the MCSCF wavefunction. Evidence for this is clear since ORMAS0 achieves chemical accuracy, while neglecting the determinants that account for electronic excitations from one subspace/dimer to another.

The characteristic ORMAS buckling mode frequencies (Table 3) are indiscernible from the CASSCF frequencies. This illustrates the success of ORMAS, since second order properties are typically more sensitive to the constructed wave function than are energies, NOON values and geometries. Identical ORMAS and CASSCF vibrational frequencies suggest that the two methods have generated similar electron densities. This in turn demonstrates that those CASSCF determinants that may be characterized as inter-dimer electronic excitations contribute little to the wave function and electron density. GVB-PP structures using two geminal pairs $[2(\pi\pi^*)^2]$ agree with CASSCF in both NOON values and buckling mode frequencies. The largest error appears in the total energy (11 mH) and likely results from the limited flexibility of the GVB-PP model.

Similar performance is found after incorporating the σ/σ^* orbital pairs. The orbital subspaces are created by grouping the active orbitals into one or two orbital subspaces per dimer (Schemes 2,3, Table 2). These partitioning schemes result in energy errors of 0.14 and 1.13mh, respectively (Table 3). All NOON values and bond lengths are in good agreement with the full CASSCF calculation. The ORMAS partitioning scheme 3 (two orbital subspaces per dimer) results in the largest error for the buckling mode frequencies ($\sim 32 \text{ cm}^{-1}$ error). Naturally, this error is reduced ($\sim 1 \text{ cm}^{-1}$) when the σ - and π -spaces are combined (scheme 2). This demonstrates the importance of including determinants that describe the excitations between π and σ orbitals within a given dimer for this system. The ORMAS(8,8) partitions (schemes 2,3) result in slightly greater errors (than ORMAS(4,4)), probably due to ignoring a larger number of determinants. Still, the best case ORMAS(8,8) (one subspace per dimer) requires less than 37% of the original CASSCF determinants to achieve chemical accuracy. The GVB-PP bond lengths and buckling mode frequencies are identical to those determined with CASSCF, while the NOON values for the π/π^* geminal pairs show slight discrepancies when including σ/σ^* geminal pairs.

Adding bulk effects onto the cluster model discussed above, by using the SIMOMM QM/MM approach (Figure 3a), results in negligible differences compared to the QM-only cluster calculations (Table 3). Again, the largest discrepancies occur in the buckling mode vibrational frequencies. The ORMAS(8,8) partitioning using two subspaces per dimer (scheme 3) provides $\sim 1 \text{ cm}^{-1}$ accuracy, in contrast to the QM-only cluster counterpart ($\sim 32 \text{ cm}^{-1}$ error). The added structural support from SIMOMM changes the vibrational behavior of the surface dimers. The cause of this, as indicated by increased predicted vibrational

frequencies ($133,138 \rightarrow 192,198 \text{ cm}^{-1}$), is likely a stiffening of the buckling mode vibrations due to the existence of the MM region of SIMOMM. In the smaller QM/MM(4,4) calculations, ORMAS reproduces the buckling frequencies to $\sim 1 \text{ cm}^{-1}$. GVB-PP shows slight differences in buckling frequencies and NOON values compared to the full CASSCF calculation.

Now consider the 4-dimer cluster shown in Figure 2b. The full CASSCF (16,16) calculation for this system approaches the practical MCSCF limit, since correlating the π and σ orbitals would create a Hamiltonian containing more than 165 million determinants (Table 4). Through sensible active space partitioning, ORMAS treats this system reasonably easily, reducing the dimension of the Hamiltonian by ~ 2 (~ 3) orders of magnitude using one (two) orbital subspace(s) per dimer. First order properties obtained using the ORMAS(16,16) partitioning schemes 1-3 (Table 2) provide excellent agreement with the CASSCF(16,16) results. The largest energy error corresponds to partitioning scheme 3 (~ 2.4 mhartree error), while the highest accuracy partition (scheme 2) has an error that is much less than 1 mh. The results shown in Table 4 were obtained with QM-only clusters.

To develop an understanding of the effects of adjacent row interactions, a 3×1 SIMOMM embedded surface model (Figure 3c) is analyzed in Table 5. There are no significant differences between the properties listed in Table 5 and those illustrated in Table 3 for the analogous 2-dimer 1×2 embedded surface model. ORMAS properties using all partitioning schemes are in reasonably good agreement with the full CASSCF results; this confirms that electronic excitations between dimers located in adjacent rows are insignificant. If the model is further increased in size to contain 5-dimers (5×1 arrangement

shown in Figure 3d) there are no significant differences in the predicted results relative to the previous 3x1 embedded system (Table 6).

To simultaneously capture same row and adjacent row dimer interactions, the embedded 2x2 cluster (Figure 3b, Table 7) is examined. As with the previous models, inter-dimer interactions have negligible influence on the surface symmetry since the surface remains symmetric. Again, there is significant savings in computational expense by treating 2-3 orders of magnitude fewer determinants, as for the 4-dimer QM cluster (Figure 2b). The larger “5+-dimer” cluster (Figure 3e, the ‘+’ in 5+ refers to the cross like arrangement of dimers) properties are summarized in Table 8. Slightly more anti-bonding character is seen here as the π^* NOON values are larger, suggesting that larger clusters might exhibit slightly more multi-reference character.

Embedding 9-dimers with SIMOMM into a 3x3 arrangement (Figure 3f) produces the largest cluster examined in this work. The results are summarized in Table 9. Note that since the full CASSCF (18,18) calculation would require more than 2.3 billion determinants, it is not a feasible calculation to perform, so no full CASSCF results are presented in the table. On the other hand, ORMAS calculations are quite feasible, and results obtained using partitioning scheme 1 (Table 2) are presented in Table 9. The goal of this 3x3 arrangement of surface dimers is to maximize the interactions on the central dimer from all nearest neighbors. Even with the central dimer experiencing the maximum number of nearest neighbor interactions, the geometry remains symmetric. The ORMAS and GVB-PP results are essentially identical. The qualitative aspects of the ORMAS NOON values and bond lengths agree with those discussed previously for the smaller, more computationally manageable clusters.

4. Conclusions

Several Si(100) cluster models have been investigated using several MCSCF methods, including full CASSCF, various ORMAS approximations, and GVB-PP. It has been systematically demonstrated that ORMAS determines properties (e.g., bond distances, vibrational frequencies, and natural orbital occupation numbers) for large Si(100) surface clusters that are in excellent agreement with those obtained with full CASSCF. When the CASSCF reference is unavailable, ORMAS properties agree with trends established for smaller, more computationally manageable systems (similar NOON values and dimer bond lengths). When only (2,2) subspaces are considered, ORMAS and GVP-PP are in close agreement with each other. As one would expect, the use of larger ORMAS subspaces (which are often necessary) can significantly reduce the error relative to a full CASSCF calculation, while the GVB-PP error remains larger.

Based on the systems examined here, it appears that the Si(100) surface is symmetric in the ground state; however, the calculations reported here do not include dynamic correlation.^{40,41,42,43,44,45} To address this issue, a second order perturbation method (ORMAS+PT2) is under development.

Based on the calculations presented here, it is unlikely that larger cluster models at the CASSCF level of theory will cause buckling of the surface dimers via inter-dimer interactions. The success of the ORMAS approach suggests that the distances between dimers is simply too large to allow inter-dimer interactions that are large enough to qualitatively alter the results presented here. This large inter-dimer distance is responsible for the negligible contributions from the excitations between dimers in ORMAS MCSCF wave

functions. It is likely that only subspaces that contain overlapping orbitals would require electronic excitations between them.

The discrepancy between buckling mode frequencies for ORMAS partitioning Schemes 2 and 3 (Table 2) indicate that reliable ORMAS Hessians require CI contributions from determinants corresponding to excitations between σ and π orbitals. This observation should be carefully considered when implementing ORMAS in mechanistic studies involving Si(100).

In general, developing an ORMAS may not be as clear-cut as it is for Si(100). For more complex systems, reliable ORMAS calculations will undoubtedly rely on chemical intuition and validation through preliminary tests. For example, a suitable ORMAS for atomic diffusion of Ga on Si(100) will incorporate dimer orbitals that are strongly interacting with Ga orbitals into the same orbital subspace. Orbitals from spectator dimers will remain in separate subspaces since their interaction with the “action region” is less significant.

Acknowledgments

This work was supported by a grant from the Air Force Office of Scientific Research. Enlightening discussions with Professor Klaus Ruedenberg and Dr. Michael Schmidt are gratefully acknowledged. Indeed, the opportunity to interact with Professor Ruedenberg has afforded us a continuing inspiration.

References

¹Albrecht P. M.; Lyding J. W. *Small* 2006, **3**, 146.

²Lopinski G. P.; Wayner D. D. M.; Wolkow R. A. *Nature* 2000, **406**, 48; Hamers T. J. *Nature* 2001, **412**, 489.

³Schlier R. E.; Farnsworth H. E. *JCP* 1959, **30**, 917.

- ⁴Shoemaker J.; Burggraf L.; Gordon M. S. JCP 2000, **112**, 2994.
- ⁵Hess J. S.; Doren D. J. JCP 2000, **113**, 9353.
- ⁶Gordon M. S.; Shoemaker J. R.; Burggraf L. W. JCP 2000, **113**, 9355.
- ⁷Konecny R.; Doren D. J.; JCP 1997, **106**, 2426.
- ⁸Robinson Broen A.; Doren D. J. JCP 1998. **109**, 2442.
- ⁹Redondo A.; Goddard W.A. J. Vac. Sci. Technol. 1982, **21**, 344.
- ¹⁰Paulus B. Surface Science 1998, **408**, 195.
- ¹¹Olson R. M.; Gordon M. S. JCP 2006, **124**, 81105.
- ¹²Paz O.; da Silva A. J. R.; Saenz J. J.; Artacho E. Surf. Sci. 2001, **482-485**, 458. Healy, S. B.; Filippi C.; Kratzer P.; Penev E.; Scheffler M. Phys. Rev. Lett. 2001, **87**, 166102.
- ¹³Yousung J.; Akinaga Y.; Jordan K. D.; Gordon M. S. 2003, Theor. Chem. Acc., **109**, 268.
- ¹⁴Lampart W. M.; Schodield D. P.; Christie R. A.; Jordan K. D. Molecular Physics 2008, **106**, 1697.
- ¹⁵Jung Y.; Akinaga Y.; Jordan K. D.; Gordon M. S. Theor. Chem. Acc. 2003, **109**, 268.
- ¹⁶Goddard, W. A.; McGill T.C. J. Vac. Sci. Technol. 1979, **16**, 1308.
- ¹⁷Bond lengths from MCSCF/6-31G(d) optimized geometries of Si₂H₄ and Si₂H₆.
- ¹⁸Shoemaker J.; Burggraf L.W.; Gordon M. S. JCP 2000, **112**, 2994.
- ¹⁹Schmidt M. W.; Gordon M. S. Annu. Rev. Phys. Chem. 1998, **4**, 233.
- ²⁰Goddard W. A.; Dunning T. H.; Hunt W. J.; Hay P. J. Accounts of Chemical Research 1973, **6**, 368. Bobrowicz F. W.; Goddard W. A. in Modern Theoretical Chemistry, Vol 3, Schaefer III, Ed., Chapter 4.
- ²¹Gordon M. S.; Schmidt M. W.; Chaban G. M.; Glaesemann K. R.; Stevens W. J.; Gonzalez C. J. Chem. Phys. 1999, **110**, 4199.

- ²²Ruedenberg K.; Sundberg K. R. in *Quantum Science*, edited by J-L. Calais; Goscinski O.; Lindenberg J.; Öhrn Y. (Plenum, New York, 1976) p. 505.
- ²³Cheung L. M.; Sundberg K. R.; Ruedenberg K. JACS 1978, **100**, 8024.
- ²⁴Cheung L. M.; Sundberg K. R.; Ruedenberg K. Int. J. Quantum Chem. 1979, **16**, 1103.
- ²⁵Seigbahn P. E.; Herberg A.; Roos B. O.; Levy B. Phys. Scr. 1980, **21**, 323.
- ²⁶Roos B. O.; Taylor P. E.; Seigbahn P. E. Chem. Phys. Lett. 1980, **48**, 156.
- ²⁷Olsen J.; Roos B. O.; Jørgensen P.; Jensen H. J. Aa. J. Chem. Phys. 1988, **89**, 2185.
- ²⁸Nakano H.; Hirao K. Chem. Phys. Lett. 2000, **317**, 90.
- ²⁹Walter D.; Carter E. A. Chem. Phys. Lett. 2001, **346**, 177.
- ³⁰Saebø S.; Pulay P. Chem. Phys. Lett. 1985, **113**, 13.
- ³¹Werner H.-J.; Knowles P. J. J. Chem. Phys. 1988, **89**, 5803.
- ³²Ivanic J. JCP 2003, **119**, 9364.
- ³³Ivanic J.; Ruedenberg K. Theor. Chem. Acc. 2001, **106**, 339.
- ³⁴Shoemaker J. R.; Burggraf L. W.; Gordon M. S. J. Phys. Chem. A 1999, **103**, 3245.
- ³⁵Lii J. H.; Allinger N. L. JACS 1989, **111**, 8566. Lii J. H.; Allinger N. L. JACS 1989, **111**, 8576. Allinger N. L.; Yuh Y. H.; Lii J. H. JACS 1989, **111**, 8551.
- ³⁶Stevens W. J.; Basch H.; Krauss M. JCP 1984, **81**, 6026. Stevens W. J.; Krauss M.; Basch H.; Jasien P. G. Can. J. Chem. 1992, **70**, 612. Cundari T. R.; Stevens W. J. JCP 1993, **98**, 5555.
- ³⁷Boys S. F., “Quantum Science of Atoms, Molecules, and Solids” Lowdin P. O., Ed, NY, 1966, pp 253-262.
- ³⁸Dudley T. J.; Olson R. M.; Schmidt M. W.; Gordon M. S. J. Comput. Chem. 2005, **27**, 352.

- ³⁹Schmidt M. W.; Baldrige K. K.; Boatz J. A.; Elbert S. T.; Gordon M. S.; Jensen J. J.; Koseki S.; Matsunaga N.; Nguyen K. A.; Su S.; Windus T. L.; Dupuis M.; Montgomery J. A. *J. Comput. Chem.* 1993, **15**, 1347. Gordon M. S.; Schmidt M. W. “Theories and Applications of Computational Chemistry, the First Forty Years”, Dykstra C. E.; Frenking G.; Kim K.S.; Scuseria G.E. Elsevier, Amsterdam, 2005, pp 1167-1189.
- ⁴⁰Hirao, K. *Chem. Phys. Lett.* 1992, 190, 374.
- ⁴¹Kozlowski, P.M.; Davidson E.R. *J. Chem. Phys.* 1993, 100, 3672.
- ⁴²Nakano, H.; Uchiyama, R.; Hirao, K. *J. Comput. Chem.* 2001, 23, 1166.
- ⁴³Nakano, H.; Nakatani, J.; Hirao, K. *J. Chem. Phys.* 2000, 114, 1133.
- ⁴⁴Malmqvist, P. Å.; Pierloot, K.; Shahi, A. R. M.; Cramer, C. J.; Gagliardi, L. *J. Chem. Phys.* 2008, 128, 204109.
- ⁴⁵Shahi, A. R. M.; Cramer, C. J.; Gagliardi, L. *PCCP* 2009, 11, 10964.

Figure 1: Si(100) surface dimer bonding and antibonding molecular orbitals

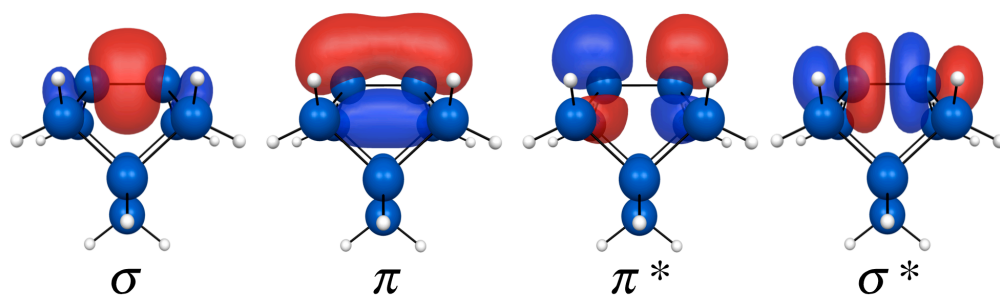


Figure 2: Models used for ORMAS, MCSCF, GVB-PP/SBKJC ECP(d) with QM-only clusters: **2a)** 2x1-Si₁₅H₁₆ and **2b)** 1x4-Si₄₂H₃₄. The model designation is axb where ‘a’ is the number of rows and ‘b’ is the number of dimers in that row.

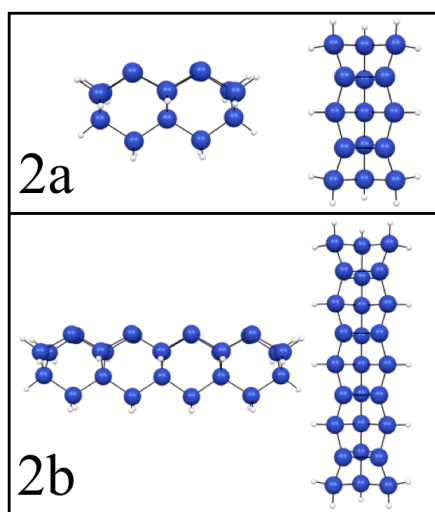


Figure 3: Models used for ORMAS, MCSCF, GVB-PP/SBKJC(d) QM/MM embedded clusters with QM[MM] regions in blue[red]: **3a)** 2x1-Si₁₅H₁₆[Si₁₉₉H₉₂], **3b)** 2x2-Si₃₃H₃₂[Si₂₆₇H₁₁₆], **3c)** 3x1-Si₃₇H₃₆[Si₂₃₂H₁₁₆], **3d)** 5x1-Si₆₅H₆₀[Si₃₂₄H₁₅₂], **3e)** 5+-Si₄₉H₄₄[Si₃₇₉H₁₄₀], and **3f)** 3x3-Si₇₁H₆₀[Si₃₇₉H₁₄₀]. Shown are the views of the QM (above) and QM/MM (below) embedded model. The model designation is axb where ‘a’ is the number of rows and ‘b’ is the number of dimers in that row. For **3e**, the 5+ in the text refers to a sequence of three adjacent dimers in the (100) direction intersecting three adjacent dimers in the (010) direction with the central dimer common to both sequences (the ‘+’ in 5+ refers to the cross like arrangement of dimers).

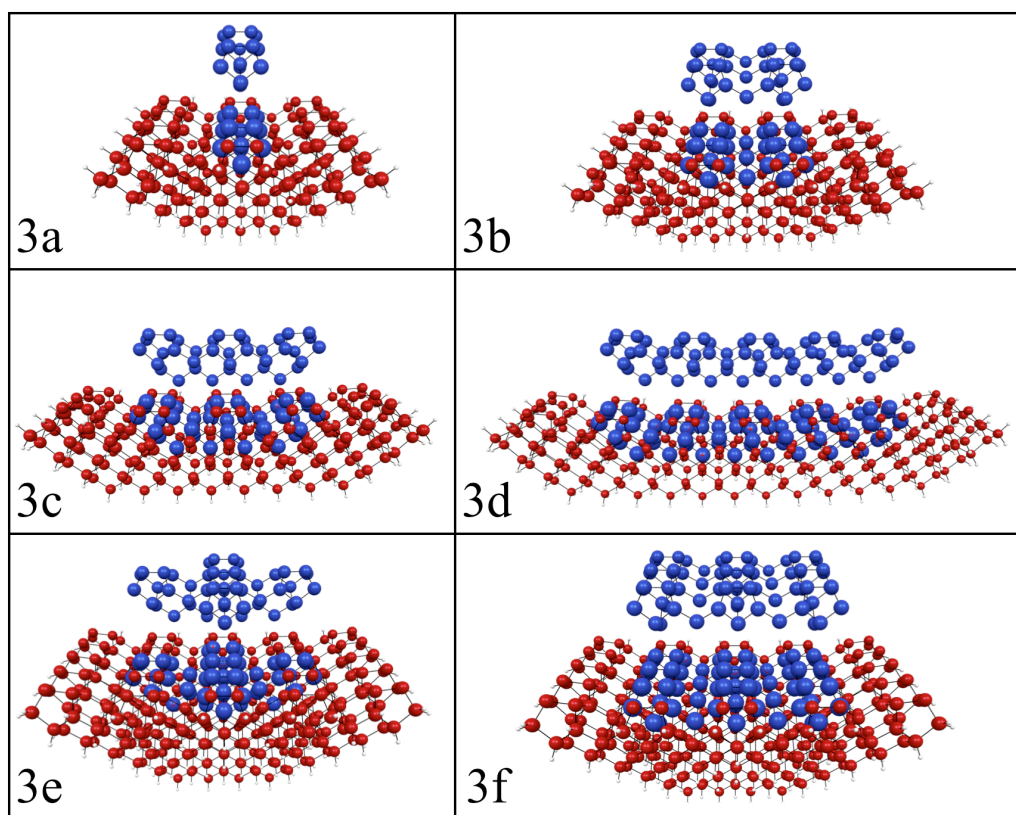


Table 1: CASSCF natural orbital occupation numbers for the π and π^* orbitals for clusters containing one (Si_9H_{12}), two ($\text{Si}_{15}\text{H}_{16}$) and three ($\text{Si}_{21}\text{H}_{20}$) dimers.

System	π_1	π_2	π_3	π_1^*	π_2^*	π_3^*
Si_9H_{12}	-	-	1.65	0.35	-	-
$\text{Si}_{15}\text{H}_{16}$	-	1.64	1.64	0.38	0.34	-
$\text{Si}_{21}\text{H}_{20}$	1.65	1.64	1.62	0.40	0.35	0.34

Table 2: Summary of partitioning schemes used.

Scheme	Orbital Subspaces	Min(Max) Electron Occupancy/Subspace
1	$2(\pi\pi^*)$	2(2)
2	$2(\pi\pi^*\sigma\sigma^*)$	4(4)
3	$2(\pi\pi^*), 2(\sigma\sigma^*)$	2(2)

TABLE 3: ORMAS, CASSCF and GVB-PP (QM and QM/MM) 2-dimer cluster energies, NOON values, buckling mode frequencies, bond lengths and the total number of required determinants.

Active space	Model Space	Energy Error (hartree)	NOON π / π^*	σ / σ^*	Buckling Mode Frequencies (cm ⁻¹)	Bond Length (Å) EXP. 2.26±0.1	Determinants
(4,4)	CASSCF	0.00000	1.64,1.64//0.36,0.36	-	192,194	2.28	36
(4,4)	$2(\pi\pi^*)^2$	0.00014	1.64,1.64//0.36,0.36	-	192,194	2.29	18
GVB-PP(2)	$2(\pi\pi^*)^2$	0.00019	1.64,1.64//0.36,0.36	-	192,194	2.29	-
(8,8)	CASSCF	0.00000	1.70,1.70//0.31,0.28	1.98,1.98//0.02,0.02	168,170	2.31	4900
(8,8)	$2(\pi\pi^*)^2 2(\sigma\sigma^*)^2$	0.00113	1.71,1.71//0.29,0.29	1.98,1.98//0.02,0.02	133,138	2.30	454
(8,8)	$2(\pi\pi^* \sigma\sigma^*)^4$	0.00014	1.70,1.70//0.30,0.30	1.98,1.98//0.02,0.02	168,169	2.30	1810
GVB-PP(4)	$2(\pi\pi^*)^2 2(\sigma\sigma^*)^2$	0.01062	1.62,1.62//0.38,0.38	1.98,1.98//0.01,0.01	193,195	2.31	-
QM/MM (4,4)	CASSCF	0.00000	1.64,1.63//0.38,0.34	-	(207 or 214),217	2.32	36
QM/MM (4,4)	$2(\pi\pi^*)^2$	0.00014	1.64,1.64//0.36,0.36	-	(207 or 214),218	2.32	18
QM/MM GVB-PP(2)	$2(\pi\pi^*)^2$	0.00019	1.64,1.64//0.36,0.36	-	(204 or 212),213	2.30	-
QM/MM (8,8)	CASSCF	0.00000	1.69,1.68//0.33,0.30	1.98,1.98//0.02,0.02	192,199	2.32	4900
QM/MM (8,8)	$2(\pi\pi^*)^2 2(\sigma\sigma^*)^2$	0.00112	1.70,1.70//0.30,0.30	1.98,1.98//0.02,0.02	192,198	2.32	454
QM/MM (8,8)	$2(\pi\pi^* \sigma\sigma^*)^4$	0.00014	1.70,1.70//0.30,0.30	1.98,1.98//0.02,0.02	192,199	2.32	1810
QM/MM GVB-PP(4)	$2(\pi\pi^*)^2 2(\sigma\sigma^*)^2$	0.01068	1.62,1.62//0.38,0.38	1.99,1.99//0.01,0.01	205,214	2.32	-

TABLE 4: ORMAS, CASSCF and GVB 4-dimer (QM-only) cluster energies, NOON values, bond lengths and total number of determinants.

Active space	Model Space	Energy Error (hartree)	π / π^*	NOON	σ / σ^*	Bond Length (Å) EXP. 2.26±0.1	Determinants
(8,8)	CASSCF	0.00000	1.69,1.69,1.68,1.62//0.40,0.37,0.35,0.34		-	2.28,2.29	4900
(8,8)	$4(\pi\pi^*)^2$	0.00037	1.65,1.65,1.63,1.63//0.38,0.38,0.36,0.36		-	2.28,2.29	454
GVB-PP(4)	$4(\pi\pi^*)^2$	0.00050	1.65,1.65,1.65//0.36,0.36,0.36,0.36		-	2.28,2.29	-
(16,16)	CASSCF	0.00000	1.71,1.71,1.69,1.69//0.33,0.31,0.29,0.28	1.98,1.98,1.98,1.98//0.02,0.02,0.02,0.02		2.30,2.31	165,636,900
(16,16)	$4(\pi\pi^*)^2 4(\sigma\sigma^*)^2$	0.00240	1.71,1.71,1.69,1.69//0.31,0.31,0.29,0.29	1.98,1.98,1.98,1.98//0.02,0.02,0.02,0.02		2.30,2.31	411,462
(16,16)	$4(\pi\pi^* \sigma\sigma^*)^4$	0.00036	1.71,1.71,1.69,1.69//0.31,0.31,0.29,0.29	1.98,1.98,1.98,1.98//0.02,0.02,0.02,0.02		2.30,2.31	6,297,030
GVB-PP(8)	$4(\pi\pi^*)^2 4(\sigma\sigma^*)^2$	0.02130	1.63,1.63,1.63,1.63//0.37,0.37,0.37,0.37	1.99,1.99,1.99,1.99//0.01,0.01,0.01,0.01		2.31,1.31	-

Table 5: ORMAS and CASSCF 3x1 embedded dimer energies, NOON values, bond lengths and number of required determinants.

Active space	Model Space	Energy Error (hartree)	π / π^*	NOON	σ / σ^*	Bond Length (Å) EXP. 2.26±0.1	Determinants
QM/MM(6,6)	CASSCF	0.00000	1.66,1.65,1.66//0.34,0.35,0.34		-	2.29,2.29	400
QM/MM(6,6)	$3(\pi\pi^*)^2$	0.00001	1.66,1.65,1.66//0.34,0.35,0.34		-	2.29,2.29	88
QM/MM GVB-PP(3)	$3(\pi\pi^*)^2$	0.00003	1.66,1.65,1.66//0.34,0.35,0.34		-	2.29,2.29	-
QM/MM(12,12)	CASSCF	0.00000	1.72,1.72,1.72//0.29,0.28,0.28	1.98,1.98,1.98//0.02,0.02,0.02		2.31,2.31	853,776
QM/MM(12,12)	$3(\pi\pi^*)^2 3(\sigma\sigma^*)^2$	0.00140	1.72,1.72,1.72//0.28,0.29,0.28	1.98,1.98,1.98//0.02,0.02,0.02		1.31,2.31	13,236
QM/MM(12,12)	$3(\pi\pi^* \sigma\sigma^*)^4$	0.00002	1.72,1.71,1.72//0.28,0.29,0.28	1.98,1.98,1.98//0.02,0.02,0.02		2.31,2.31	103,704
QM/MM GVB-PP(6)	$3(\pi\pi^*)^2 3(\sigma\sigma^*)^2$	0.01600	1.65,1.64,1.65//0.35,0.36,0.35	1.99,1.99,1.99//0.01,0.01,0.01		2.32,2.32	-

TABLE 6: ORMAS and CASSCF QM/MM 5x1-dimer cluster energies, NOON values, bond lengths and number of required determinants.

Active space	Model Space	Energy Error (hartree)	NOON π / π^*	Bond Length (Å) EXP. 2.26±0.1	Determinants
QM/MM(10,10)	CASSCF	0.00000	1.66,1.66,1.66,1.65,1.65,0.35,0.35,0.34,0.34	2.29,2.29,2.29	63,504
QM/MM(10,10)	$5(\pi\pi^*)^2$	0.00003	1.66,1.66,1.66,1.66,0.34,0.35,0.35,0.34	2.29,2.29,2.29	2,424
QM/MM GVB-PP(5)	$5(\pi\pi^*)^2$	0.00007	1.66,1.65,1.65,1.66,0.34,0.35,0.35,0.34	2.29,2.29,2.29	-

TABLE 7: ORMAS and CASSCF QM/MM 2x2-dimer cluster energies, NOON values, bond lengths and number of required determinants

Active space	Model Space	Energy Error (hartree)	NOON π / π^*	σ / σ^*	Bond Length (Å) EXP. 2.26±0.1	Determinants
QM/MM(8,8)	CASSCF	0.00000	1.64,1.64,1.63,1.62,0.39,10.39,0.35,0.35	-	2.30	4900
QM/MM(8,8)	$4(\pi\pi^*)^2$	0.00036	1.63,1.63,1.63,1.63,0.37,0.37,0.37,0.37	-	2.30	454
QM/MM GVB-PP(4)	$4(\pi\pi^*)^2$	0.00046	1.63,1.63,1.63,1.63,0.37,0.37,0.37,0.37	-	2.30	-
QM/MM(16,16)	CASSCF	0.00000	1.70,1.70,1.69,1.69,0.32,0.32,0.29,0.29	1.98,1.98,1.98,1.98,0.02,0.02,0.02,0.02	2.32	165,636,900
QM/MM(16,16)	$4(\pi\pi^*)^2$	0.00223	1.70,1.70,1.70,1.70,0.30,0.30,0.30,0.30	1.98,1.98,1.98,1.98,0.02,0.02,0.02,0.02	2.32	411,462
QM/MM(16,16)	$4(\sigma\sigma^*)^2$	0.00174	1.70,1.70,1.70,1.70,0.30,0.30,0.30,0.30	1.98,1.98,1.98,1.98,0.02,0.02,0.02,0.02	2.32	6,297,030
QM/MM GVB-PP(8)	$4(\pi\pi^*)$	0.02113	1.61,1.61,1.61,1.61,0.39,0.39,0.39,0.39	1.99,1.99,1.99,1.99,0.01,0.01,0.01,0.01	2.33	-
	$4(\sigma\sigma^*)$					

Table 8: ORMAS,CASSCF,GVB-PP/SBKJC(d) QM/MM 5+-dimer cluster energies, NOON values, bond lengths and number of required determinants. The subscripts on the π orbitals refer to the positions of the surface dimers on the cluster model. 1:center dimer, 2: outside dimer in same row as center dimer, 3: outside dimer in row parallel to center row. These subscripts do not have meaning for the CASSCF properties as the orbitals are delocalized.

Active space	Model Space	Energy Error (hartree)	NOON $\pi_1\pi_2\pi_3 / \pi_1^*\pi_2^*\pi_3^*$	Bond Length (Å) EXP. 2.26±0.1	Determinants
QM/MM(10,10)	CASSCF	0.00000	1.57,1.63,1.66/0.43,0.37,0.34	2.31,2.30,2.29	63,504
QM/MM(10,10)	5($\pi\pi^*$)	0.00032	1.57,1.63,1.66/0.43,0.37,0.34	2.32,2.30,2.30	2,424
QM/MM GVB-PP(5)	5($\pi\pi^*$)	0.00041	1.57,1.63,1.66/0.43,0.37,0.34	2.32,2.30,2.29	-

TABLE 9: ORMAS and CASSCF QM/MM 3x3-dimer cluster energies, NOON values, bond lengths and number of required determinants. The subscripts on the π/σ orbitals refer to 1:center dimer, 2:corner dimer, 3: outside dimer in same row as center dimer, 4: outside dimer in row parallel to center row. These subscripts do not have meaning for the CASSCF properties since the orbitals are delocalized.

Active space	Model Space	NOON $\pi_1\pi_2\pi_3\pi_4 / \pi_1^*\pi_2^*\pi_3^*\pi_4^*$	Bond Length (Å) EXP. 2.26±0.1	Determinants
QM/MM(18,18)	CASSCF	-	-	2,363,904,400
QM/MM(18,18)	9($\pi\pi^*$)	1.57,1.64,1.63,1.59/0.43,0.36,0.37,0.41	2.31,2.30,2.30,2.31	2,325,976
QM/MM GVB-PP(9)	9($\pi\pi^*$)	1.57,1.64,1.63,1.59/0.43,0.36,0.37,0.41	2.31,2.30,2.30,2.31	-

CHAPTER 3. QUASI-DEGENERATE SECOND-ORDER PERTURBATION THEORY FOR ORMAS-SCF REFERENCE FUNCTIONS

A paper accepted by *The Journal of Chemical Physics*

Luke Roskop and Mark S. Gordon

A multi-configuration quasi-degenerate second-order perturbation method based on the occupation restricted multiple active space (ORMAS-PT/ORMAS) reference wavefunction is presented. This approach is useful for cases in which a complete active space self-consistent field (CASSCF) wavefunction is necessary but computationally impractical. ORMAS gives one the ability to approximate an otherwise large CASSCF wavefunction using only a subset of the configurations from the CASSCF space. The essential idea behind ORMAS-PT is to use the multi-reference Møller-Plesset formalism to correct the ORMAS reference energy. A computational scheme employing direct CI methodology is presented. Several tests are presented to demonstrate the performance of the ORMAS-PT method.

1. Introduction

For any chemical system, the multi-configurational self-consistent field (MCSCF) approach provides the optimum zeroth order approximation to the exact non-relativistic wavefunction. The reliability of the MCSCF approach originates in the inclusion of non-dynamic correlation, which is important in chemical systems that exhibit near degeneracies and therefore require a multi-reference description. Near degeneracies commonly occur, for example, in the vicinity of conical intersections, during bond breaking, in radical chemistry, electronic excited states, and unsaturated transition metal compounds. The accuracy and computational demands of an MCSCF calculation depends on the active space that is

composed of a set of active orbitals and active electrons. The dimension of this active space is the limiting factor in MCSCF treatments.

Although MCSCF provides qualitatively correct zeroth order wavefunctions, the absence of dynamic correlation generally prevents quantitative agreement with experiment. Therefore, one needs to use the MCSCF wavefunction as a starting point for multi-reference configuration interaction (MRCI) or multi-reference perturbation theory (MRPT) calculations. MRPT methods, in particular, differ in the manner in which the Hamiltonian is partitioned and in the MCSCF orbital canonicalization.¹ The most popular MRPT approaches are the complete active space second-order perturbation theory (CASPT2),² multi-reference Møller-Plesset perturbation theory (MRMP),³ and multi-configurational quasi-degenerate perturbation theory (MCQDPT).⁴ The multi-state MCQDPT method reduces to MRMP for a single state problem. Both CASPT2 and MRMP/MCQDPT are accurate methods that are usually more efficient than MRCI methods.

Both CASPT2 and MRMP/MCQDPT employ a complete active space (CAS) reference wavefunction. This reference wavefunction is a full CI within the active space. Since in the CAS approach one iterates the wavefunction to self-consistency, the method is commonly referred to as a complete active space self-consistent-field (CASSCF)⁵ or full optimized reaction space (FORS)⁶ approach. The computational demands of modern MCSCF algorithms limit a CASSCF/FORS calculation to 16 electrons distributed among 16 orbitals (16,16) or possibly an (18,18) active space if symmetry can be used. Consequently, MRPT studies using a CAS reference wavefunction with active spaces that are larger than (16,16) are computationally prohibitive and only rarely performed. Another promising technique for the treatment of strongly correlated, multi-reference systems is the Density Matrix

Renormalization Group approach (DMRG).⁷ DMRG facilitates the use of significantly larger active spaces than traditional MCSCF methods, but in comparison to CASSCF/FORS and MRPT, DMRG can be more computationally demanding for a desired level of accuracy.

Over the past 15 years, developments in approximate CAS MRPT methods have facilitated the expansion of feasible CASSCF active spaces within the MRPT approach. Examples of such methods are the restricted active space perturbation theory through second order (RASPT2),⁸ quasi-complete active space quasi-degenerate perturbation theory (QCASQDPT),⁹ and general MCQDPT (GMCQDPT).¹⁰ The reference wavefunctions for RASPT2 and QCASQDPT2 are restricted active space self-consistent field (RASSCF)¹¹ and QCAS¹² wavefunctions, respectively.

One issue that is not addressed in some MRPT methods is the treatment of determinants that are present in the full CAS reference space but not in the approximate reference space. These determinants, referred to here as IECs (internally excited configurations), correspond to determinants in the full CAS that are singly and doubly excited relative to the reference determinants. IECs should be accounted for in the PT correction since they have been shown to be significant in MRPT treatments.¹⁰

The current implementations of RASPT2 do not account for the IEC contributions,⁸ while QCASQDPT and GMCQDPT do. Though QCASQDPT and GMCQDPT benefit from increased flexibility in the reference wavefunction, the computational efficiency of these methods suffers since the PT contributions are determined indirectly. That is, enumeration of the determinants that couple to the excited determinants are not directly determined. Furthermore, QCASQDPT and GMCQDPT (and MRMP/MCQDPT) require generation of the one and two particle density matrices, whereas RASPT2 (and CASPT2) also require three

particle density matrices.⁸ It would therefore be beneficial to develop a general MRPT method that takes advantage of direct PT methodology, requires only the first and second order density matrices, and accounts for the IEC contributions.

The present paper introduces an alternate MRPT method that employs the determinant based occupation restricted multiple active space (ORMAS)¹³ wavefunction as the zeroth order reference function. The novel approach of ORMAS reduces the complexity of a computationally prohibitive CI space through greater flexibility in partitioning than RASSCF and QCAS. The determinants included in the ORMAS expansion are specified through user-defined restrictions on the minimum and maximum electron occupation numbers for each user-defined orbital subspace (see Figure 1). Using ORMAS to appropriately partition a CAS, one can eliminate many ineffective electronic configurations (“*deadwood*”¹⁴) that contribute negligibly to the molecular energy. In this sense, the ORMAS approach has an analogous effect to that of the pre-screening of two-electron integrals. Thus, ORMAS has the ability to retain only the most important configurations in a CI space.

In comparison to RASPT2 and QCASQDPT, ORMAS-PT provides greater flexibility within the reference wavefunction. ORMAS can generate the RASSCF wavefunction if desired. Currently, ORMAS cannot generate the QCAS reference, but it does have the ability to generate a similar function (referred to as ORMAS0) that includes the QCAS reference determinants as a subset of the ORMAS0 CI expansion basis. Compared to configuration state function (CSF) codes, the ORMAS wavefunction is expanded within a basis of determinants, thereby eliminating I/O by efficiently calculating Hamiltonian matrix elements “on the fly” (direct CI). The direct CI methodology is adapted for the PT energy contributions described below.

2. Method

The conventional approach to n^{th} order perturbation theory considers the exact non-relativistic Hamiltonian as a perturbed independent particle (zeroth order) Hamiltonian, with the energy and wavefunction expanded in n orders of perturbation.^{15,16} In contrast to single reference perturbation theory, MRPT (including restricted open shell (ROHF) PT) is not uniquely defined. There have consequently been numerous analyses of the various MRPT formalisms. The ORMAS-PT method presented here follows the perturb-then-diagonalize¹⁷ prescription, based on the Hirao parallel direct determinant implementation^{3,18,19} for FORS/CASSCF wavefunctions. As a consequence of the underlying ORMAS reference, there are distinct differences in how ORMAS-PT is implemented compared to the MRMP/MCQDPT approach that is intended for a CAS reference. The approach taken in this section is to present the Hirao MRPT procedure in three parts, followed by a summary of the modifications that are required for ORMAS-PT. Kozłowski and Davidson²⁰ have presented a thorough review of multi-reference second-order perturbation theory methods.

(1) Orbital canonicalization: CASSCF orbitals are not uniquely defined, since the reference energy is invariant to orbital rotations within the core, the active, and the external orbital spaces. To create a consistent set of orbitals, a closed-shell-like Fock operator²¹ is constructed with the predefined MCSCF state-averaged one-particle density matrix (Equation 1). \mathbf{F} in Equation 1 is commonly called the standard Fock operator:

$$F_{pq} = h_{pq} + \sum_{rs} D_{rs}^{\text{ave}} \left[(pq|rs) - \frac{1}{2}(pr|qs) \right] \quad (1)$$

In Equation 1 p, q correspond to molecular spin orbitals, h_{pq} is an element of the bare one-electron Hamiltonian, $(pq|rs)$ is an electron repulsion integral, and \mathbf{D}^{ave} is the MCSCF state-

averaged one-particle density matrix. The standard Fock operator is block diagonalized within the core-plus-inactive, the active, and the external orbital sub-blocks. Diagonalization of \mathbf{F} produces a unique set of canonical orbitals $\{\psi\}$ and orbital energies $\{\epsilon\}$ that are required in the MRPT expansion.

(2) Zeroth-order Hamiltonian: The choice of H_0 (Equation 2) is conceptually simple in that the MRPT zeroth-order energy (E_0) is the sum of the occupied orbital energies ϵ_i weighted by the corresponding diagonal elements of the one-particle density matrix D_{ii} . Consequently, the MRMP H_0 reduces to the single reference MP2 H_0 when considering a singlet wavefunction composed one reference configuration.

$$E_{\beta}^{(0)} = \langle \Psi_{\beta}^{(0)} | H_0 | \Psi_{\beta}^{(0)} \rangle = \sum_i^{\text{occupied}} D_{ii}^{\beta} \epsilon_i \quad (2)$$

A variety of correction functions has been applied to the MRMP H_0 to improve the reliability of MRPT but a summary of these is beyond the scope of the current discussion.²⁰ The present study employs the “barycentric” definition of H_0 (Equation 2) used by Hirao³ and is equivalent to the H_0 used in the Kozłowski-Davidson MROPT1 method.²⁰

(3) Second order energy correction: Based on the approach of Löwdin,¹⁷ the scheme adopted here first performs the perturbation problem and then removes the degeneracy (if any) by solving the secular problem corresponding to the effective Hamiltonian (H_{eff}):

$$\langle \Psi_{\alpha}^{(0)} | H_{\text{eff}} | \Psi_{\beta}^{(0)} \rangle = E_{\beta}^{\text{MCSCF}} \delta_{\alpha\beta} + \sum_K^{\text{SD(CAS)}} \frac{\langle \Psi_{\alpha}^{(0)} | V | K \rangle \langle K | V | \Psi_{\beta}^{(0)} \rangle}{E_{\beta}^{(0)} - E_K^{(0)}} \quad (3)$$

In Equation 3 α and β refer to MCSCF states, E_{β}^{MCSCF} is the first order energy for MCSCF state β , $E_{\beta}^{(0)}$ is the “barycentric” energy for state β defined by Equation 2, $E_K^{(0)}$ is the zeroth

order energy for determinant K defined by Equation 4, and the summation runs over all singly and doubly excited configurations, from active orbitals into the external orbitals space of the MCSCF.

$$E_K^{(0)} = \langle K | H_0 | K \rangle = \sum_i^{\text{occupied}} D_{ii}^K \varepsilon_i = \sum_i^{\text{occupied}} \varepsilon_i \quad (4)$$

Since the diagonal elements of the one-particle density matrix for excited determinant K will be either 0 or 1 (in the molecular spin-orbital basis), $E_K^{(0)}$ is a sum of occupied orbital energies corresponding to K . The perturbation, V , comes from Equation 5 and is expressed as in Equation 6:

$$H = H_0 + V \quad \rightarrow \quad V = H - H_0 \quad (5)$$

$$V = \sum_i h(i) + \sum_{i < j} \frac{1}{r_{ij}} - \sum_i \varepsilon_i \quad (6)$$

In Equations 5-6, H_0 is the zeroth order Hamiltonian, $h(i)$ is the bare one-electron Hamiltonian for electron i , r_{ij} is the interelectronic distance between electrons i and j , and ε_i is an orbital energy. For single state MRPT (MRMP), the effective Hamiltonian (H_{eff}) is a 1x1 matrix, so the perturbative correction to that state is just the matrix itself. For more than one state, a multi-state MRPT requires the diagonalization of H_{eff} (MCQDPT).

Now consider a reformulation of the original Hirao MRPT method for the ORMAS-PT implementation. Modifications of the orbital canonicalization and the second order correction are necessary, whereas the definition of the zeroth order Hamiltonian given above is retained.

(1) ORMAS orbital canonicalization: To ensure that the ORMAS-PT energy is consistent regardless of how the reference wavefunction is constructed, the ORMAS-PT

second order energy contributions are determined from a set of orbitals that are obtained by block diagonalization of the standard Fock operator (Equation 1). The core-plus-inactive and virtual sub blocks are treated as previously described. The ORMAS reference energy is not invariant under orbital rotations *between* active subspaces. Therefore, the active orbital sub-block itself is block diagonalized according to the user defined orbital subspaces. For example, suppose an ORMAS active space is configured for 3 active subspaces. There would then be 3 active orbital sub-blocks in the standard Fock matrix, instead of a single active sub-block as is used in a MRMP/MCQDPT treatment.

(2) ORMAS-PT second order energy correction: In the limit of merging all ORMAS subspaces, the second order energy correction for an ORMAS reference wavefunction is equivalent to the corresponding FORS/CASSCF wavefunction. Since a general ORMAS employs an incomplete active space, the second order ORMAS-PT energy correction must be formulated to account for internally excited configurations (IECs). IECs are defined here as single and double excitations from active orbitals to active orbitals for which the excited occupations are not consistent with the ORMAS reference occupation restrictions. The general ORMAS-PT effective Hamiltonian is constructed according to Equation 7.

$$\begin{aligned} \langle \Psi_{\alpha}^{(0)} | H_{\text{eff}} | \Psi_{\beta}^{(0)} \rangle = & E_{\beta}^{\text{MCSCF}} \delta_{\alpha\beta} + \sum_{K \notin \text{CAS}}^{\text{SD(ORMAS)}} \frac{\langle \Psi_{\alpha}^{(0)} | V | K \rangle \langle K | V | \Psi_{\beta}^{(0)} \rangle}{E_{\beta}^{(0)} - E_K^{(0)}} \\ & + \sum_{K \notin \text{ORMAS}}^{\text{CAS}} \frac{\langle \Psi_{\alpha}^{(0)} | V | K \rangle \langle K | V | \Psi_{\beta}^{(0)} \rangle}{E_{\beta}^{(0)} - E_K^{(0)}} \end{aligned} \quad (7)$$

Similar to MRMP/MCQDPT, the first term on the right hand side (RHS) of Equation 7 contributes the MCSCF energy of state β to the diagonal of the effective Hamiltonian. The second term on the RHS of Equation 7 sums over singly and doubly excited configurations,

into the external orbital space of the MCSCF. The last term on the RHS of Equation 7 sums over the IECs. Neglecting the last term on the RHS of Equation 7 is possible and can provide good results,⁸ but for a rigorous MRPT it is essential that this last term be included. In implementing Equation 7, the main challenge is creating a scheme to directly enumerate the IECs. This is discussed next.

The IECs are determined by initially relaxing the ORMAS reference restrictions on the minimum and maximum electron occupancies for each orbital subspace. Appropriately modifying the occupation restrictions provides criteria that the IECs must satisfy. Orbital subspace specifications permitting, these modifications allow each subspace to accommodate one or two additional electrons and to lose one or two electrons. The occupation restrictions are modified as follows:

$$N_I^{*\max} = \begin{cases} N_I^{\max} + 2 & \text{if } (N_I^{\max} + 2) \leq \text{number of orbitals in subspace I} \\ N_I^{\max} + 1 & \text{if } (N_I^{\max} + 1) = \text{number of orbitals in subspace I} \\ N_I^{\max} & \text{if } N_I^{\max} = \text{number of orbitals in subspace I} \end{cases} \quad \text{For } I = 1, X \quad (8)$$

$$N_I^{*\min} = \begin{cases} N_I^{\min} - 2 & \text{if } (N_I^{\min} - 2) \geq 2 \\ N_I^{\min} - 1 & \text{if } N_I^{\min} = 1 \\ N_I^{\max} & \text{if } N_I^{\min} = 0 \end{cases} \quad \text{For } I = 1, X \quad (9)$$

In Equations 8-9, X is the number of ORMAS orbital subspaces, $N_I^{\min}(N_I^{\max})$ specifies the reference occupation restrictions on the minimum (maximum) electron occupations for subspace I, and $N_I^{*\min}(N_I^{*\max})$ is the modified minimum (maximum) electron occupation restriction for subspace I. Modified occupation restrictions are used to generate α -groups and β -groups, which describe the distribution of the α -electrons and β -electrons among the X

ORMAS orbital subspaces. These α -groups and β -groups are then combined in a pair-wise procedure to find combinations that adhere to the modified electron occupation restrictions. For each valid combination, α -strings and β -strings are directly enumerated¹³ from the α -group and β -group. These α -strings and β -strings are combined to form determinants; the α -strings and β -strings indicate which α and β molecular spin-orbitals are occupied. The resulting determinants correspond not only to the IECs, but also to the reference determinants that must be screened for.

It is necessary to categorize each IEC specifically, because a single algorithm cannot directly determine the energy contributions for all IECs. This is analogous to the need for separate treatments of determinants that correspond to valence-to-external vs. active-to-external electronic excitations, as is required in MRMP/MCQDPT formulations. The scheme introduced here classifies each IEC into one of eight types; these types are listed in Table 1 and are discussed in detail in the following paragraphs. Each IEC classification is based upon how the electron occupations in each subspace are not consistent with the minimum and maximum electron occupation restrictions of the reference specifications (N_I^{\min} and N_I^{\max} ; for $I = 1, X$). With respect to reference occupation restrictions, an inconsistency would correspond to a subspace being ‘over-occupied’ (too many electrons) or ‘under-occupied’ (too few electrons). For example, if $N_I^{\max} = 4$ for subspace I and subspace I actually contains five electrons, then subspace I is ‘over-occupied’ by one electron.

The symbol $R_I^{P,Q}$ is introduced here to monitor whether subspace I is consistent with the reference occupation restrictions when α -group P is combined with β -group Q. In

Equation 10 below, $N_{I,P}^\alpha$ ($N_{I,Q}^\beta$) is the number of α -electrons (β -electrons) assigned to subspace I from α -group P (β -group Q), N_I^{\min} and N_I^{\max} (defined above) are the minimum and maximum occupation restrictions for reference subspace I. An ‘under-occupied’ (‘over-occupied’) subspace corresponds to $R_I^{P,Q} < 0$ ($R_I^{P,Q} > 0$) while $R_I^{P,Q} = 0$ indicates subspace I is consistent with the reference occupation restrictions. For example, $R_I^{P,Q} = -2$ indicates subspace I is ‘under-occupied’ by two electrons.

$$R_I^{P,Q} = \begin{cases} (N_{I,P}^\alpha + N_{I,Q}^\beta - N_I^{\min}) & \text{if } (N_{I,P}^\alpha + N_{I,Q}^\beta - N_I^{\min}) < 0 \\ (N_{I,P}^\alpha + N_{I,Q}^\beta - N_I^{\max}) & \text{if } (N_{I,P}^\alpha + N_{I,Q}^\beta - N_I^{\max}) > 0 \\ 0 & \text{otherwise} \end{cases} \quad \text{For } I = 1, X \quad (10)$$

$R_I^{P,Q}$ can be used to compute a label, $\Delta_{P,Q}$ (employing Equations 11-14 below) that classifies a set of IECs that are generated from the combination of α -group P with β -group Q.

$$Y_{P,Q} = \sum_I^X R_I^{P,Q} \quad (11)$$

$$Z_{P,Q} = \sum_I^X |R_I^{P,Q}| \quad (12)$$

$$\gamma_{P,Q} = \begin{cases} 1 & \text{if } Y_{P,Q} \geq 1 \\ -1 & \text{if } Y_{P,Q} < 1 \end{cases} \quad (13)$$

$$\Delta_{P,Q} = \gamma_{P,Q} (|Y_{P,Q}| + 2^{Z_{P,Q}}) \quad (14)$$

In Equations 11-14, $Y_{P,Q}$ is a sum over all ‘under-occupations’ and ‘over-occupations’ ($R_I^{P,Q}$) for each subspace, $Z_{P,Q}$ is an *absolute* sum over all ‘under-occupations’ and ‘over-

occupations' for each subspace, $\gamma_{P,Q}$ is a sign transfer function, and $\Delta_{P,Q}$ is the resulting IEC label. All IEC labels are calculated on the fly since their storage can get excessive.

The first column in Table 1 corresponds to all possible $\Delta_{P,Q}$ labels (IEC type). Regardless of the how the ORMAS wavefunction is constructed, only eight values of $\Delta_{P,Q}$ correspond to single or double IECs. The value $\Delta_{P,Q}=1$ corresponds to the reference configurations. Each of these values is described next. Unless indicated otherwise, all subspaces are consistent with the reference occupation restrictions.

$\Delta_{P,Q}=1$: all subspaces adhere to reference occupation restrictions (not excited configurations)

$\Delta_{P,Q}=-3$: one subspace is 'under-occupied' by one electron.

$\Delta_{P,Q}=3$: one subspace is 'over-occupied' by one electron.

$\Delta_{P,Q}=4$: one subspace is 'over-occupied' by one electron *and* one other subspace is 'under-occupied' by one electron.

$\Delta_{P,Q}=-6$: *either* one subspace is 'under-occupied' by two electrons *or* two subspaces are both 'under-occupied' by one electron.

$\Delta_{P,Q}=6$: *either* one subspace is 'over-occupied' by two electrons *or* two subspaces are both 'over-occupied' by one electron.

$\Delta_{P,Q}=-9$: one subspace is 'over-occupied' by one electron *and either* one other subspace is 'under-occupied' by two electrons *or* two other subspaces are both 'under-occupied' by one electron

$\Delta_{P,Q}=9$: one subspace is ‘under-occupied’ by one electron *and either* one other subspace is ‘over-occupied’ by two electrons *or* two other subspaces are both ‘over-occupied’ by one electron.

$\Delta_{P,Q}=16$: (four situations are possible)

- 1) one subspace is ‘under-occupied’ by two electrons *and* one other subspace in ‘over-occupied’ by two electrons.
- 2) one subspace is ‘under-occupied’ by two electrons *and* two other subspaces are both ‘over-occupied’ by one electron.
- 3) two subspaces are both ‘under-occupied’ by one electron *and* one other subspace is ‘over-occupied’ by two electrons.
- 4) two subspaces are both ‘under-occupied’ by one electron *and* two other subspaces are both ‘over-occupied’ by one electron.

As illustrated in Table 1, the different cases for a given $\Delta_{P,Q}$ are distinguished by the corresponding values of $R_I^{P,Q}$. Configurations that have $\Delta_{P,Q}=1$ are reference configurations and are not included in the summation over the IEC (last term in Equation 7). In addition, some α -group and β -group combinations can correspond to triple and higher excited determinants. These IECs cannot couple with any of the reference configurations and are also not considered in the ORMAS-PT.

From each α -group/ β -group pair corresponding to an IEC label that characterizes a single or double excitation, α -strings and β -strings are enumerated and combined pair-wise to form the proper IECs (excited determinants). These IECs are treated with the appropriate algorithm that corresponds to their $\Delta_{P,Q}$ labels. This classification scheme provides a means

to directly enumerate the IECs, leading to a highly efficient algorithm for computing their ORMAS-PT energy contributions.

To illustrate the above scheme, consider employing ORMAS to partition a singlet system of 6 electrons and 12 orbitals into three 4-orbital subspaces. The minimum (maximum) reference occupation restrictions for the three subspaces are set to 0,0,0 (6,6,6). Thus any distribution of electrons among the subspaces is allowed. There are 28 possible distributions of the 6 electrons (seen in Table 2); the total number of electrons in subspace I for distribution J is indicated by $N_{I,J}$. These 28 distributions correspond to a total of 48,400 determinants. This is identical to a full CAS, so IECs are not relevant in this case.

Next, consider the minimum (maximum) reference occupation restrictions for each subspace to be 2,2,2 (2,2,2). These restrictions allow for just a single distribution (distribution 13) while all other distributions correspond to IECs (distributions 1-12,14-28). Not all of the distributions that correspond to IECs will contribute to the ORMAS-PT energy. For example consider distribution 2 in Table 2: subspace one is ‘over-occupied’ by three electrons, subspace two is ‘under-occupied’ by one electron, and subspace three is ‘under-occupied’ by two electrons. IECs corresponding to distribution 2 represent triple excitations since subspace one is ‘over-occupied’ by three electrons. IECs corresponding to triple excitations cannot couple to determinants in the ORMAS reference space, so these IECs will not contribute to the ORMAS-PT energy. On the other hand, consider distribution 4 in Table 2: subspace one is ‘over-occupied’ by two electrons, subspace two is consistent with the reference occupation restriction, and subspace three is ‘under-occupied’ by two electrons. Therefore, IECs from distribution 4 correspond to double excitations from the ORMAS reference space. Because of this, IECs corresponding to distribution 4 will make important

contributions to the wavefunction and energy. The numerical IEC label given to any α -group P and β -group Q combination resulting in the distribution 4 is $\Delta_{P,Q}=16$ (from Equations 10-14 or see Table 1).

An appropriate $\Delta_{P,Q}$ label is assigned for each α -group P/ β -group Q pair. Once one knows $\Delta_{P,Q}$ for a particular pair, the appropriate algorithm can be executed to directly determine the IEC contributions to the energy and wavefunction.

3. Applications

The ORMAS-PT method has been implemented in the GAMESS (General Atomic and Molecular Electronic Structure System)²² suite of programs. GAMESS has been used for all calculations that are presented here. The ORMAS-PT method is benchmarked here against MRMP/MCQDPT results for four test cases, including a state averaged MCSCF wavefunction, singlet and higher spin states, and ionic systems.

Potential energy surface of lithium fluoride:

The LiF dissociation energy curves for the two lowest $^1\Sigma^+$ states are examined to determine whether ORMAS-PT can properly account for the avoided crossing between the paths that lead to neutral and ionic products. Starting from the LiF equilibrium geometry and proceeding to dissociated products, the lower energy $^1\Sigma^+$ state before the avoided crossing may be described as ionic, or at least highly polar, while the higher energy state may be described as covalent. After the avoided crossing the lower $^1\Sigma^+$ state becomes covalent, while the upper state dissociates to ionic products. In C_{2v} symmetry, the reference CAS wavefunction is constructed from six electrons and nine active orbitals CAS(6,9): $4a_1, 5a_1, 6a_1, 1b_1, 2b_1, 3b_1, 1b_2, 2b_2, 3b_2$. Molecular orbitals $1a_1$, $2a_1$, and $3a_1$ correspond to the

fluorine 1s and 2s and lithium 1s atomic orbitals. These orbitals are chemically inactive and remain in the core.

Using ORMAS, the CAS(6,9) space is partitioned into three orbital subspaces: $\{4a_1, 5a_1, 6a_1\}$, $\{1b_1, 2b_1, 3b_1\}$, and $\{1b_2, 2b_2, 3b_2\}$. The electron occupation restrictions for each orbital subspace are set to a minimum (maximum) of 2 (2) electrons. These occupation restrictions permit only two electrons to occupy any of the subspaces, irrespective of spin. The 6-311++G(3df,3pd)²³ basis set is used for all MCQDPT and ORMAS-PT calculations. The orbitals are state-averaged over the two lowest energy $^1\Sigma^+$ states.

Figure 2 shows the two lowest $^1\Sigma^+$ potential energy curves for ORMAS-PT and MCQDPT. It is important to note in Figure 2 there are actually four curves but the ORMAS-PT and MCQDPT curves overlap making it difficult to distinguish between the two. Additionally, ORMAS-PT is able to account for the qualitative features of the two surfaces, namely the equilibrium geometry and the avoided crossing around 12-13 bohr. Figure 3 shows the relative error of the singlet-singlet energy splitting between ORMAS-PT and MCQDPT. Beyond 2.9 bohr ($r_{eq} = 2.98$ bohrs)²⁴ there is less than 0.2 kcal/mol error between ORMAS-PT and MCQDPT while at shorter distances ORMAS-PT underestimates the energy splitting

Potential energy surface of $Si_{15}H_{16}$ dimer buckling modes:

Whether or not Si(100) ground state surface dimers are buckled is an unresolved matter since highly correlated methods are impractical for the large surface models needed to eliminate edge effects. To circumvent the computational expense of large cluster models, small surface clusters are routinely used (Figure 4A). To investigate the geometry of the Si(100) surface dimers on the MRPT ground state PES, one can first calculate the MCSCF

vibrational modes that correspond to the buckling frequencies. The geometries are then perturbed along these modes while calculating MRPT single point energies.

Geometric distortions along two buckling modes of $\text{Si}_{15}\text{H}_{16}$ were performed while the potential energy surface was mapped. At both the FORS/CASSCF and ORMAS-SCF level, the cc-pVDZ basis set²⁵ was used to optimize $\text{Si}_{15}\text{H}_{16}$. Subsequently, the Hessian (matrix of second order energy derivatives) was diagonalized to determine the vibrational modes. The CASSCF active space includes one σ/σ^* and one π/π^* pair from each dimer leading to a total of 8 electrons distributed among 8 molecular orbitals (8,8). For ORMAS-SCF, each dimer is given its own subspace. This results in two subspaces each containing four molecular orbitals (one σ/σ^* and one π/π^* pair). The reference occupation restrictions for the ORMAS-SCF subspaces are set to a minimum (maximum) of 4 (4) electrons. The FORS/CASSCF and ORMAS-SCF buckling vibration modes for $\text{Si}_{15}\text{H}_{16}$ may be seen in Figure 4. The hydrogen atoms are eliminated for clarity in Figures 4B and 4C. The two buckling modes are referred to as mode-1 and mode-2.

As may be seen in Figure 5, displacements along the two buckling modes show that the ORMAS-PT surface features agree nicely with the MRMP result that the MRPT energy increases as the dimers are displaced along their buckling modes. The absolute error between mode-1 and mode-2 between the two methods is negligible (Figure 6). The energy error (kcal/mol) is small even though the displaced geometries are slightly different since the structures are perturbed along modes and minima corresponding to ORMAS-SCF or FORS/CASSCF. This good agreement attests to the reliability of a properly constructed ORMAS and that ORMAS-PT is suitable for predicting MRMP absolute energy differences.

Singlet-triplet and doublet-quartet splitting of $\text{OxoMn}(\text{salen})$ and $\text{OxoMn}(\text{salen})^{-1}$:

The catalyst chloro-4,4'-(1,2-ethanediyl)dinitrilo)bis(2-pentanonato)(2-)-N,N',O,O')-m-oxomanganese, referred to here as oxoMn(salen) (Figure 7), has been previously studied²⁶ using CAS MRPT but is reexamined here to determine the suitability of ORMAS-PT for transition metal complexes. Geometry optimizations on the singlet, doublet, and quartet species were performed using the 6-31G(d) basis set.²⁷ The triplet MCSCF state spontaneously dissociates the oxygen atom upon optimization from the bound singlet geometry.²⁸ Consequently, triplet calculations presented here were done at the corresponding optimized singlet geometries. In addition, ORMAS-PT singlet-triplet splittings were computed at both the CASSCF and ORMAS optimized geometries. ORMAS-PT doublet-quartet splittings were computed at the ORMAS optimized geometries only.

Three different active spaces are employed to treat the singlet and triplet spin states for oxoMn(salen). The first active space is a CAS with 12 electrons distributed among the 11 active orbitals depicted in Figure 8. The second active space (ORMAS-3) partitions the active orbitals into three subspaces: $\{\pi_L\pi_L^*\}$, $\{\pi_R\pi_R^*\}$, and $\{\pi_1\pi_1^*\pi_2\pi_2^*\sigma\sigma^*d_{MN}\}$ with electron occupations restricted to a minimum (maximum) of 2,2,8 (2,2,8), respectively. The final active space (ORMAS-6) partitions the active orbitals into six subspaces: $\{\pi_L\pi_L^*\}$, $\{\pi_R\pi_R^*\}$, $\{\pi_1\pi_1^*\}$, $\{\pi_2\pi_2^*\}$, $\{\sigma\sigma^*\}$, and $\{d_{MN}\}$ with electron occupations restricted to a minimum (maximum) of 2,2,2,2,2,1 (2,2,4,4,4,2), respectively.

There are only slight modifications to two of the active subspaces for anionic doublet and quartet states of oxoMn(salen)⁻¹. Here the FORS/CASSCF active space is specified to have 13 electrons distributed among the same 11 active orbitals (13,11). For ORMAS, the subspace orbitals for the anionic species are partitioned in the same way as in the neutral species. The difference between the neutral and anionic specifications concerns the electron

occupation restrictions. The electron occupation restrictions for the ORMAS-3 subspaces are set to a minimum and maximum of 2,2,9 (2,2,9), while the ORMAS-6 subspace restrictions are the same as those used for the neutral species.

Table 3 shows the singlet-triplet energy splitting of neutral oxoMn(salen) for the three selected active spaces. Using the CAS energy as the benchmark, the ORMAS-3 active space shows the best agreement for the predicted singlet-triplet splitting. If one uses the CASSCF geometry to calculate the ORMAS-3 PT singlet-triplet splitting, the ORMAS-3 PT error is ~ 1.8 kcal/mol. However, when the geometry is optimized with ORMAS-3, the ORMAS-3 PT error decreases to only ~ 0.1 kcal/mol. The ORMAS-6 PT predicted singlet-triplet splitting is in error by ~ 2.5 kcal/mol at the CASSCF geometry and by ~ 2.6 kcal/mol at the ORMAS-6 geometry. The ORMAS-6 and OMRAS-6//CAS PT prediction that the singlet state lies lower in energy than the triplet state is incorrect. Since the singlet-triplet splitting is small, this error may imply that a more complete active space is needed.

For the oxoMn(salen)⁻¹ anion, the doublet-quartet splitting (Table 4) is calculated to be much larger than the singlet-triplet splitting in the neutral species. For the anion, both ORMAS-3 PT and ORMAS-6 PT predicted splittings agree with CAS MRPT to within ~ 0.6 kcal/mol. The good agreement between both the neutral and anionic oxoMn(salen) species demonstrates the ability of ORMAS to provide a reliable reference wavefunction for the MRPT correction.

For ¹A oxoMn(salen), going from the full CAS MRPT treatment to ORMAS-3 decreases both the number of determinants and CPU time²⁹ (Table 3) by roughly half an order of magnitude. For the open shell systems, ORMAS-PT uses ~ 1 -2 orders of magnitude fewer determinants and ~ 1 order of magnitude less CPU time compared to the CAS MRPT.

The ability to use of fewer determinants through an ORMAS decreases CPU time but more importantly the system memory requirements also decrease. This makes ORMAS-PT an efficient alternative if the CAS MRPT is prohibitive.

Trans-polyacetylene ionization potentials:

ORMAS-PT vertical ionization potentials (IPs) for several *trans*-polyacetylene polymers are now examined to understand the convergence of ORMAS-PT predicted IPs to MRMP results. The IP is calculated from the difference in absolute energies of the neutral and ionized species for systems composed of 2-8 ethylene subunits (Figure 9). The energies of the ionized species are calculated at the optimized geometries of the corresponding neutral species. These systems are highly conjugated, so the active space is constructed around the π orbitals and electrons.

The MRMP calculations use a CAS reference wavefunction corresponding to an active space of size $(2n, 2n)$ for which n is the number of ethylene subunits. For the ORMAS-PT IPs, the active molecular orbitals are partitioned into two subspaces. With respect to the RHF determinant, the first subspace (space-1) corresponds to the occupied π molecular orbitals while the unoccupied π^* molecular orbitals comprise the second subspace (space-2). A maximum of two, three, or four electrons are allowed to excite from orbitals in space-1 to orbitals in space-2. The minimum (maximum) reference occupation restrictions for space-1 and space-2 are set to $2n - \text{MAX}$ and 0 ($2n$ and MAX) for which $\text{MAX} = 2, 3, 4$ depending on the level of excitation. All results presented use the cc-pVTZ basis set.²⁵

Table 5 shows ORMAS-SCF and CASSCF IPs for *trans*-polyacetylene polymers of length n . For polymers of length $n = 3-8$, the ORMAS-SCF IPs oscillate slightly from $\text{MAX} = 2$

to 3 to 4, but these variations are very small. At the highest excitation level (MAX=4) there is good agreement between the ORMAS-SCF and CASSCF (maximum error ~ 0.02 eV). Both ORMAS-SCF and CASSCF under-estimate vertical IPs compared with the experimental values for polymers of length $n=2,3,4$.³⁰ It is therefore likely that ORMAS-SCF and CASSCF IPs are also underestimated for the longer polymers ($n=5-8$).

Table 6 shows ORMAS-PT and MRMP IPs for *trans*-polyacetylene polymers of length n . The MRMP IPs for polymers of length $n=2,3,4$ are in agreement with experiment. From this it is clear that dynamic correlation is important to reliably predict IPs for *trans*-polyacetylene polymers. For polymer $n=3$, the progression from MAX=2,3,4 shows that the ORMAS-PT errors increase as MAX increases. For polymers of length $n=4-8$, ORMAS-PT predicted vertical IPs exhibit good convergence to the MRMP values. The error for these longer polymers range from 0.08-0.11 eV, 0.04-0.8 eV, and 0.01-0.05 eV for excitation levels set to MAX=2, MAX=3, and MAX=4, respectively. ORMAS-PT is an efficient alternative to MRMP as it uses 1-2 orders of magnitude fewer determinants. For *trans*-polyacetylene polymers of length $n=8$ (or larger), ORMAS-PT is the only practical approach to compute their IPs since the active space (16,16) is prohibitive for MRMP computations.

4. Conclusions

A quasi-degenerate perturbation theory based on the ORMAS reference wavefunction has been described. For a complete active space MRPT, the effective Hamiltonian considers singly and doubly excited configurations, into the external orbital space of the MCSCF. For ORMAS-PT, the effective Hamiltonian was reformulated to also include internally excited configurations (IECs). A scheme was presented that directly enumerates the IECs to allow for efficient computation of the IECs contributions to the energy and wavefunction.

The ORMAS-PT method has been applied to four different systems, with the following key conclusions:

1) For the two lowest $^1\Sigma^+$ states of LiF, ORMAS-PT reproduces the MCQDPT avoided crossing between the two state-averaged potential energy surfaces. The energy splitting between the two states shows the largest error for LiF bond lengths less than the equilibrium distance. Starting from the LiF equilibrium bond distance and longer, the energy splitting showed an error less than 0.2 kcal/mol along the reaction coordinate to the dissociated products.

2) ORMAS-PT correctly reproduces the MRMP potential energy surface along the symmetric and anti-symmetric dimer buckling modes for a $\text{Si}_{15}\text{H}_{16}$ cluster. As the $\text{Si}_{15}\text{H}_{16}$ cluster geometry is perturbed along the symmetric and anti-symmetric buckling modes, the energy increases at both the ORMAS-PT and MRMP levels of theory. This indicates the symmetric structure is the global minimum.

3) ORMAS-PT was applied to the oxoMn(salen) species to examine its performance with transition metal complexes. ORMAS-PT reproduces the MRMP neutral singlet-triplet energy splitting and anionic doublet-quartet energy splitting with errors less than 0.6 kcal/mol.

4) ORMAS-PT reproduces the MRMP ionization potentials for *trans*-polyacetylene polymers of various lengths. For the longer polymers, ORMAS-PT was shown to systematically converge to the MRMP results as the number of configurations used to construct the reference wavefunctions is systematically increased.

ORMAS-PT is an efficient approximation to the MRMP/MCQDPT level of theory. ORMAS-PT is able to attain a high level accuracy and reduce the number of determinants

required for a typical MRMP/MCQDPT by 1-2 orders of magnitude. It follows that ORMAS-PT reduces the system memory needed to handle large active spaces. The highly efficient ORMAS-PT approach opens the door for MRPT treatments of highly correlated systems that are otherwise computationally prohibited by CASSCF/FORS references.

Acknowledgements

This work was supported by a grant from the Air Force Office of Scientific Research. Enlightening discussions with Dr. Michael Schmidt and Dr. Joe Ivanic are gratefully acknowledged.

References

- ¹M. W. Schmidt, M. S. Gordon, *Annu. Rev. Chem.* **49**, 233 (1998).
- ²K. Andersson, P.-Å. Malmqvist, B. O. Roos, A. J. Sadlej, K. Wolinski, *J. Phys. Chem.* **94**, 5483, (1990). K. Andersson, P.-Å. Malmqvist, B. O. Roos, *J. Chem. Phys.* **96**, 1218 (1992). K. Andersson, *Theor. Chim. Acta.* **91**, 31, (1995). H.-J. Werner, *Mol. Phys.* **89**, 645 (1996).
- ³K. Hirao, *Chem. Phys. Lett.* **190**, 374 (1992). K. Hirao, *Chem. Phys. Lett.* **196**, 397 (1992). K. Hirao, *Int. J. Quant. Chem.* **S26**, 517, (1992).
- ⁴H. Nakano, *J. Chem. Phys.* **99**, 7983 (1993). H. Nakano, *Chem. Phys. Lett.* **207**, 372 (1993).
- ⁵P. Seigbahn, A. Heiberg, B. Roos, B. Levy, *Phys. Scr.* **21**, 323 (1980).
- ⁶K. Ruedenberg, K. R. Sundberg, *Quantum Science* (J-L. Calais, O. Goscinski, J. Lindenberg, Y. Öhrn, Eds.) pp. 505-515 (Plenum Publ. Co., New York, 1976).
- ⁷S. R. White, *Phys. Rev. Lett.* **69**, 2863 (1992).
- ⁸P.-Å. Malmqvist, K. Pierloot, A. R. M. Shahi, C. J. Cramer, L. Gagliardi, *J. Chem. Phys.* **128**, 204109 (2008). A. R. M. Shahi, C. J. Cramer, L. Gagliardi, *Phys. Chem. Chem. Phys.* **11**, 10964 (2009).

- ⁹H. Nakano, J. Nakatani, K. Hirao, J. Chem. Phys. **114**, 1133 (2001). R. Ebisuzaki, Y. Watanabe, H. Nakano, Chem. Phys. Lett. **442**, 164 (2007).
- ¹⁰H. Nakano, R. Uchiyama, K. Hirao, J. Comput. Chem. **23**, 1166 (2002).
- ¹¹J. Olsen, B. O. Roos, P. Jørgensen, H. J. Aa. Jensen, J. Chem. Phys. **89**, 2185 (1988). P.-Å. Malmqvist, A. Rendell, B. O. Roos, J. Phys. Chem. **94**, 5477 (1990).
- ¹²H. Nakano, K. Hirao, Chem. Phys. Lett. **317**, 90 (2000).
- ¹³J. Ivanic, J. Chem. Phys. **119**, 9364 (2003).
- ¹⁴J. Ivanic, K. Ruedenberg, Theor. Chem. Acc. **106**, 339 (2001).
- ¹⁵C. Møller, M. S. Plesset, Phys. Rev. **46**, 618 (1934).
- ¹⁶J. A. Pople, J. S. Binkley, R. Seeger, Int. J. Quant. Chem. **10**, 1 (1976).
- ¹⁷P. O. Löwdin, J. Chem. Phys. **19**, 1396 (1951).
- ¹⁸J. Ivanic J. (unpublished)
- ¹⁹J. M. Rintelman, M. S. Gordon, G. D. Fletcher, J. Ivanic, J. Chem. Phys. **124**, 034303 (2006).
- ²⁰P. M. Kozlowski, E. R. Davidson, J. Chem. Phys. **100**, 3672 (1994).
- ²¹B. O. Roos, P. Linse, P. E. M. Siegbahn, M. R. A. Blomberg, Chem. Phys. **66**, 197 (1982).
- ²²M. W. Schmidt, K. K. Baldridge, J. A. Boatz, S. T. Elbert, M. S. Gordon, J. J. Jensen, S. Koseki, N. Matsunaga, K. A. Nguyen, S. Su, T. L. Windus, M. Dupuis, J. A. Montgomery, J. Comput. Chem. **15**, 1347 (1993). M. S. Gordon, M. W. Schmidt, *Theories and Applications of Computational Chemistry, the First Forty Years*, C. Dykstra G. Frenking, K. S. Kim, G. E. Scuseria (Elsevier, Amsterdam, 2005) pp 1167-1189.
- ²³R. Krishnan, J. S. Binkley, R. Seeger, J. A. Pople, J. Chem. Phys. **72**, 650 (1980).
- ²⁴FORS/CASSCF(6,9) 6-311G++(3df,3dp)

- ²⁵T. H. Dunning, J. Chem. Phys. **90**, 1007 (1989). D. E. Woon, T. H. Dunning, J. Chem. Phys. **98**, 1358 (1993).
- ²⁶J. Ivanic, J. R. Collins, S. K. Burt, J. Phys. Chem. A **108**, 2314 (2004).
- ²⁷R. Ditchfield, W. J. Hehre, J. A. Pople, J. Chem. Phys. **54**, 724 (1971). W. J. Hehre, R. Ditchfield, J. A. Pople, J. Chem. Phys. **56**, 2257 (1972). P. C. Hariharan, J. A. Pople, Theor. Chim. Acta. **28**, 213 (1973). M. M. Fanci, W. J. Pietro, W. J. Hehre, J. S. Binkley, M. S. Gordon, D. J. Defrees, J. A. Pople, J. Chem. Phys. **77**, 3654 (1982). V. A. Rassolov, J. A. Pople, M. A. Ratner, T. L. Windus, J. Chem. Phys. **109**, 1223 (1998).
- ²⁸J. Ivanic, J. Chem. Phys. **119**, 9377 (2003).
- ²⁹Timing performed on two dual-quad core Intel Xeon R5420 nodes
- ³⁰K. Kimura, S. Katsumata, Y. Achiba, T. Yamazaki, S. Iwata *Handbook of Hel photoelectron Spectra of Fundamental Organic Molecules* (Halsted Press, New York, 1981). T. J. Cave, E. R. Davidson, J. Phys. Chem. **92**, 2173 (1988). R. J. Cave, E. R. Davidson, J. Phys. Chem. **92**, 614 (1988). M. Beez, G. Bieri, H. Bock, E. Heilbronner, Helv. Chim. Acta **56**, 1028 (1973). E. E. Astrup, H. Bock, K. Wittel, P. Heimbach, Acta Chem. Scand., Ser. A, **29**, 827 (1975). T. B. Jones, J. P. Maier, Int. J. Mass. Spectrom. Ion. Phys. **31**, 287 (1979).

Figure 1: Schematic representation of the ORMAS method. The full valence space orbitals are partitioned into S subspaces each containing N,M,...,O orbitals, respectively. Minimum and Maximum electron occupation restrictions are assigned to each subspace to determine which determinants from the original full valence space are used to construct the ORMAS Hamiltonian.

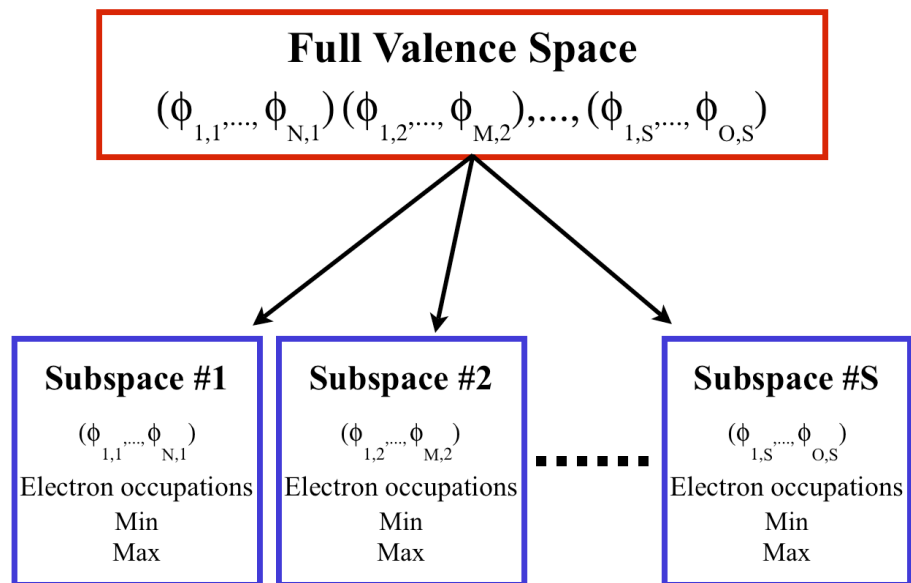


Figure 2: Potential energy curve (hartree) for the dissociation of LiF. The \circ and \triangle designate the two lowest $^1\Sigma^+$ states.

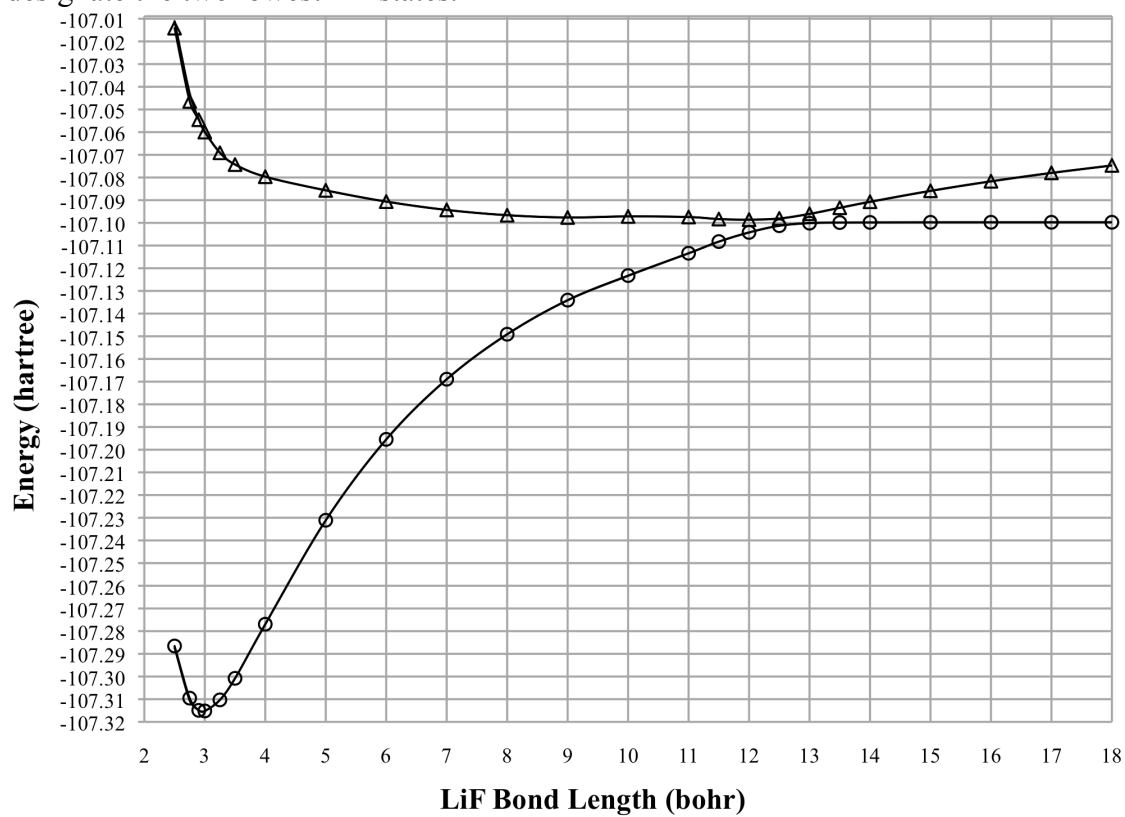


Figure 3: ORMAS-PT relative error (kcal/mol) for the energy splitting for the two lowest $^1\Sigma^+$ states compared to MCQDPT.

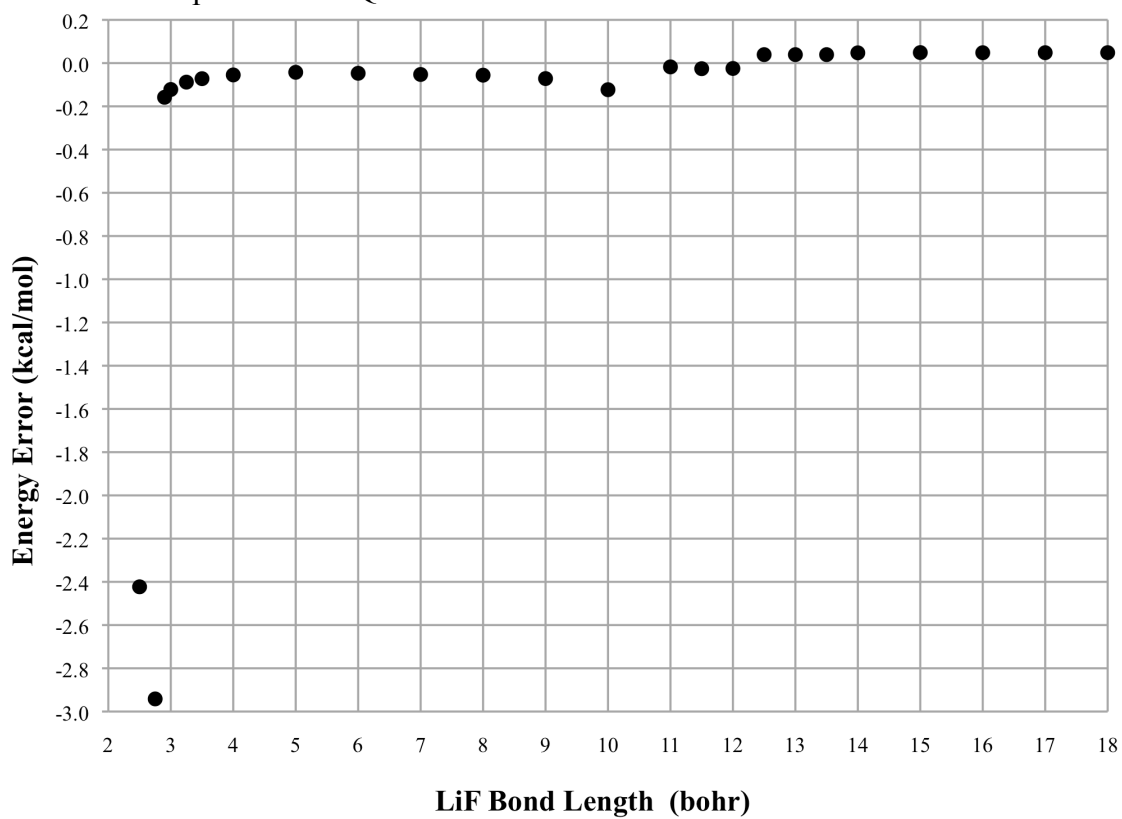


Figure 4: A) Optimized structure of $\text{Si}_{15}\text{H}_{16}$. B) buckling mode-1, C) buckling mode-2. For clarity, the hydrogen atoms in B and C been removed. The buckling mode frequencies in B and C correspond to those calculated with CASSCF and ORMAS(in parentheses).

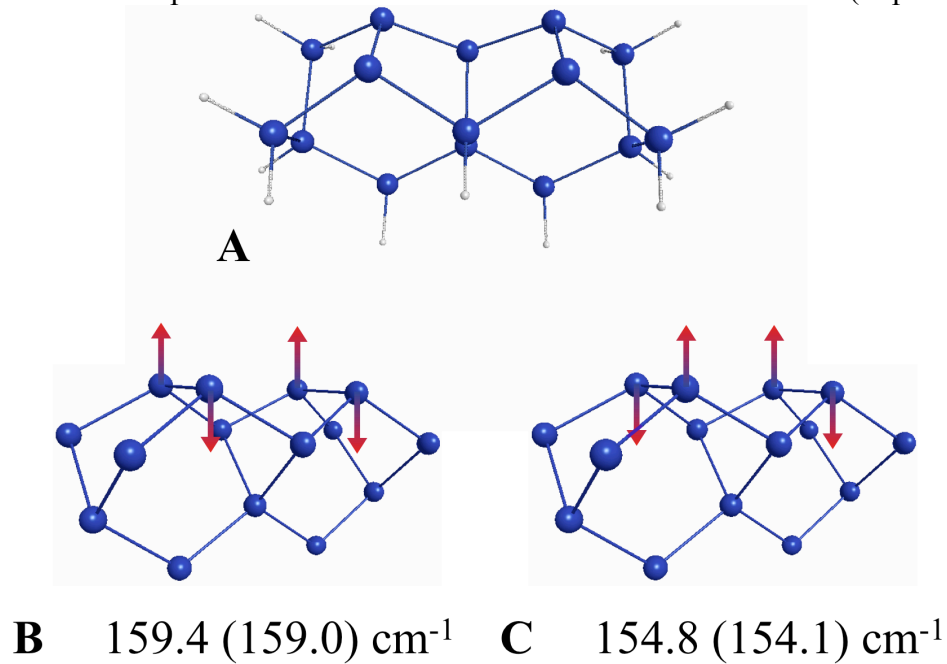


Figure 5: MRPT potential energy curves (hartree) for the displacement $\text{Si}_{15}\text{H}_{16}$ from the optimized geometries of FORS/CASSCF and ORMAS along buckling mode 1 (\bullet, \circ) and mode 2 (\blacksquare, \square). Here the filled markers refer the MRMP energy while the unfilled markers refer to ORMAS-PT.

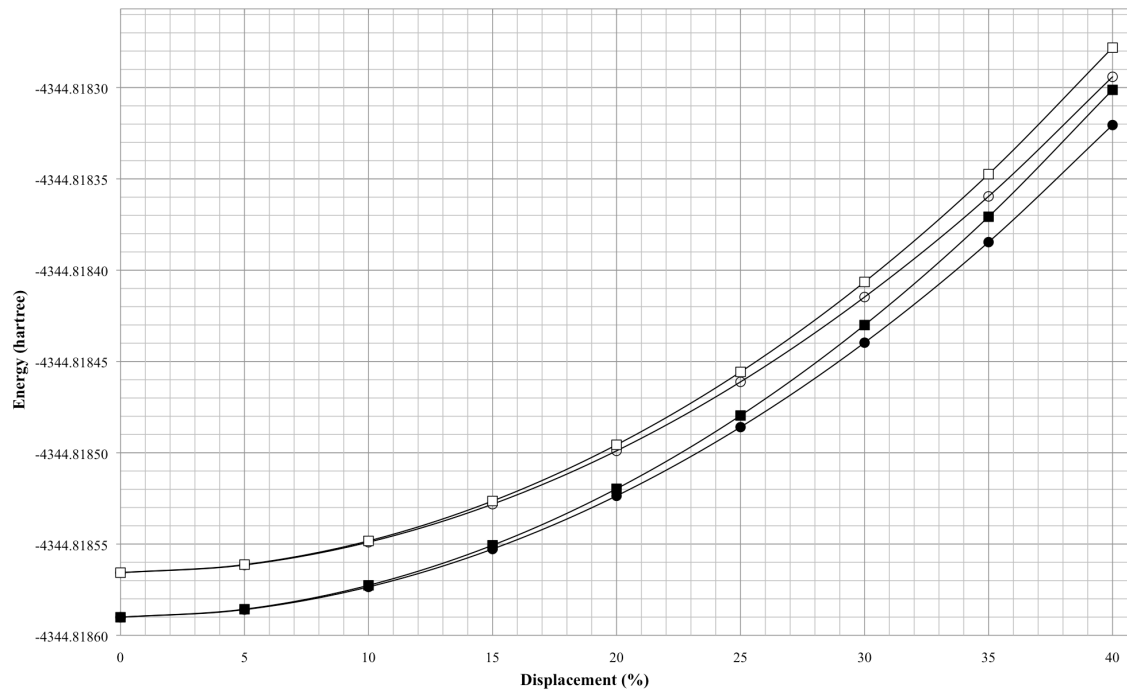


Figure 6: Relative error (kcal/mol) between mode 1 (●) and mode 2 (□) with respect to the minimum energy structure for ORMAS-PT compared to MRMP.

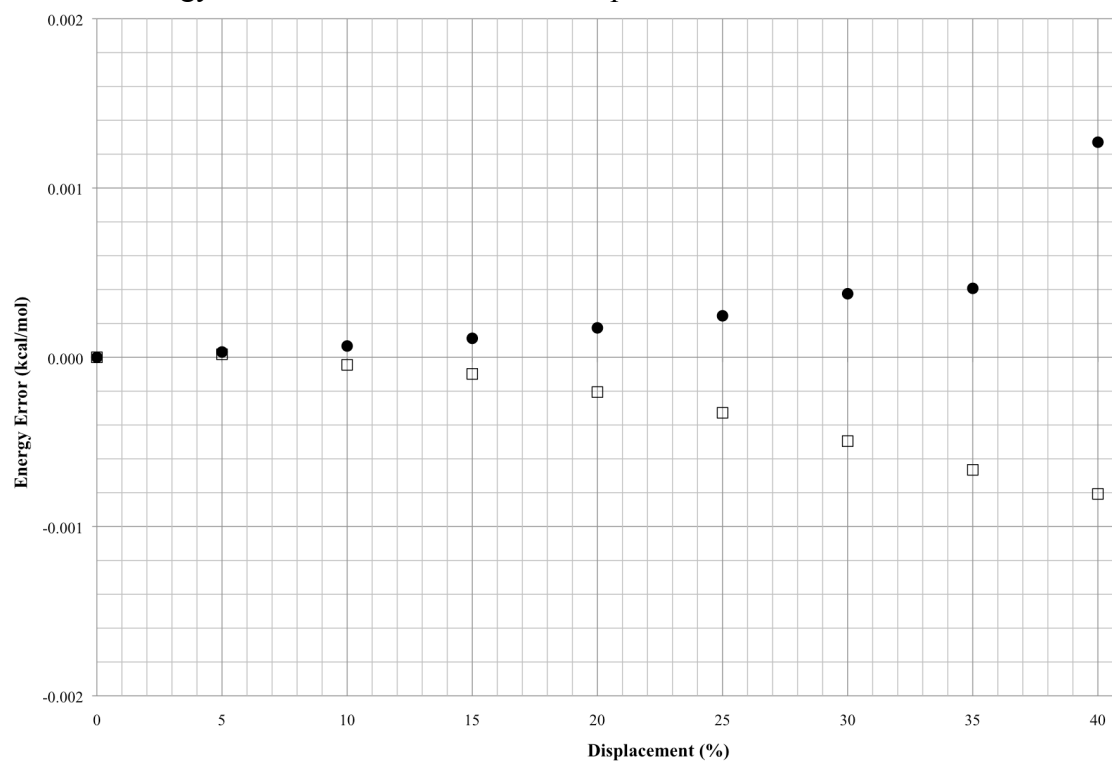


Figure 7: OxoMn(salen)

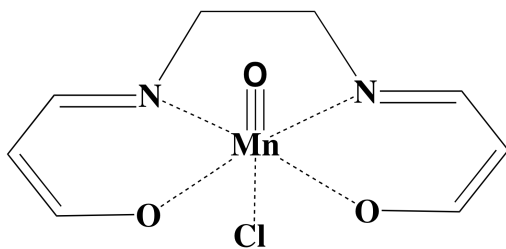


Figure 8: OxoMn(salen) CASSCF/6-31G* MCSCF optimized orbitals.

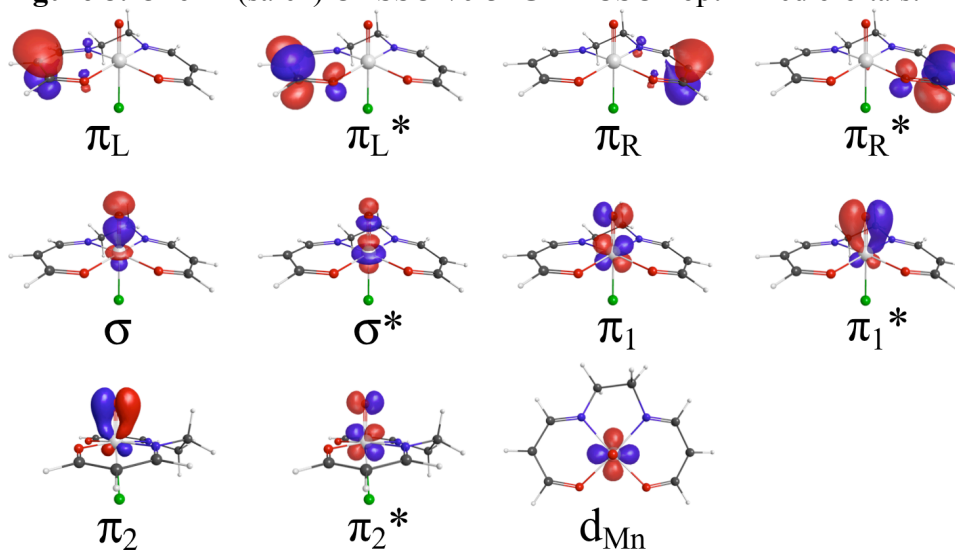


Figure 9: Schematic of *trans*-polyacetylene of length n .

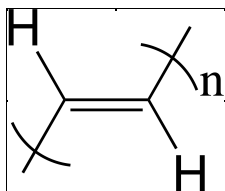


Table 1: Classification types of internally excited configurations (IEC). Type 1 IECs correspond to reference determinants. $R_I^{P,Q}$ specifies how subspace I is ‘over-occupied’/‘under-occupied’ upon combining α -group P with β -group Q (a zero integer means that subspace is consistent with the reference occupation restriction).

IEC type Δ_{PQ}	Electron ‘over-occupations’/‘under-occupations’ in subspace:							
	$R_I^{P,Q}$	$R_I^{P,Q}$	$R_I^{P,Q}$	$R_I^{P,Q}$	$R_I^{P,Q}$	$R_I^{P,Q}$	$R_I^{P,Q}$	$R_I^{P,Q}$
1 ^a	0	0	0	0	0	0...0		0
-3	-1	0	0	0	0	0...0		0
3	1	0	0	0	0	0...0		0
4	1	-1	0	0	0	0...0		0
-6	-2	0	0	0	0	0...0		0
-6	-1	-1	0	0	0	0...0		0
6	2	0	0	0	0	0...0		0
6	1	1	0	0	0	0...0		0
-9	-2	1	0	0	0	0...0		0
-9	-1	-1	1	0	0	0...0		0
9	-1	2	0	0	0	0...0		0
9	-1	1	1	0	0	0...0		0
16	-2	2	0	0	0	0...0		0
16	-2	1	1	0	0	0...0		0
16	-1	-1	2	0	0	0...0		0
16	-1	-1	1	1	0	0...0		0

Table 2: All possible distributions of 6 electrons among three four-orbital subspaces. Distribution 13 is the only allowable distribution of electrons with the minimum (maximum) electron occupation restrictions of 2 (2) for each subspace. $N_{I,J}$ is the total number of electrons assigned to subspace I from distribution J.

Distribution (J)	$N_{1,J}$	$N_{2,J}$	$N_{3,J}$	# Determinants
1	6	0	0	16
2	5	1	0	192
3	5	0	1	192
4	4	2	0	768
5	4	1	1	1664
6	4	0	2	768
7	3	3	0	1184
8	3	2	1	4416
9	3	1	2	4416
10	3	0	3	1184
11	2	4	0	768
12	2	3	1	4416
13	2	2	2	7552
14	2	1	3	4416
15	2	0	4	768
16	1	5	0	192
17	1	4	1	1664
18	1	3	2	4416
19	1	2	3	4416
20	1	1	4	1664
21	1	0	5	192
22	0	6	0	16
23	0	5	1	192
24	0	4	2	768
25	0	3	3	1184
26	0	2	4	768
27	0	1	5	192
28	0	0	6	16

Table 3: MCSCF and MRPT singlet-triplet energy splitting for oxoMn(salen) using a complete active space and two ORMAS partitions.

System	Method	Active Space	MCSCF Singlet-Triplet Splitting (kcal/mol)	MRPT Singlet-Triplet Splitting (kcal/mol)	# of Determinants	Time for PT correction (min) ^d
¹ A oxoMn(salen)	CAS	(12,11)	-	-	213,444	209
	ORMAS-3 ^b /CAS ^a	$\{d_{Mn}, \sigma^*, \pi_1, \pi_1^*, \pi_2, \pi_2^*, \pi_L, \pi_L^*, \pi_R, \pi_R^*\}$	-	-	34,104	42
	ORMAS-6 ^c /CAS ^a	$\{d_{Mn}, \{\sigma, \sigma^*\}, \{\pi_1, \pi_1^*\}, \{\pi_2, \pi_2^*\}, \{\pi_L, \pi_L^*\}, \{\pi_R, \pi_R^*\}\}$	-	-	11,520	16
	ORMAS-3 ^b	$\{d_{Mn}, \sigma^*, \pi_1, \pi_1^*, \pi_2, \pi_2^*, \pi_L, \pi_L^*, \pi_R, \pi_R^*\}$	-	-	34,104	42
	ORMAS-6 ^c	$\{d_{Mn}, \{\sigma, \sigma^*\}, \{\pi_1, \pi_1^*\}, \{\pi_2, \pi_2^*\}, \{\pi_L, \pi_L^*\}, \{\pi_R, \pi_R^*\}\}$	-	-	11,520	16
³ A oxoMn(salen)	CAS	(12,11)	-0.3	-2.2	152,460	293
	ORMAS-3 ^b /CAS ^a	$\{d_{Mn}, \sigma, \sigma^*, \pi_1, \pi_1^*, \pi_2, \pi_2^*, \pi_L, \pi_L^*, \pi_R, \pi_R^*\}$	-0.3	-0.4	24,948	51
	ORMAS-6 ^c /CAS ^a	$\{d_{Mn}, \{\sigma, \sigma^*\}, \{\pi_1, \pi_1^*\}, \{\pi_2, \pi_2^*\}, \{\pi_L, \pi_L^*\}, \{\pi_R, \pi_R^*\}\}$	-1.3	0.3	8,742	19
	ORMAS-3 ^b	$\{d_{Mn}, \sigma^*, \pi_1, \pi_1^*, \pi_2, \pi_2^*, \pi_L, \pi_L^*, \pi_R, \pi_R^*\}$	-0.2	-2.3	24,948	51
	ORMAS-6 ^c	$\{d_{Mn}, \{\sigma, \sigma^*\}, \{\pi_1, \pi_1^*\}, \{\pi_2, \pi_2^*\}, \{\pi_L, \pi_L^*\}, \{\pi_R, \pi_R^*\}\}$	-1.0	0.4	8,742	19

^aORMAS calculation performed at the singlet CAS optimized geometry

^bMinimum(maximum) electron occupation restrictions respective to active space: 8,2,2(8,2,2)

^cMinimum(maximum) electron occupation restrictions respective to active space: 1,2,2,2,2(2,4,4,2,2)

^dTotal time for computing PT energy correction on two dual-quad core Intel Xeon R5420 nodes

Table 4: MCSCF and MRPT doublet-quartet energy splitting for oxoMn(salen)⁻¹ using a complete active space and two ORMAS partitions.

System	Method	Active Space	MCSCF Double-Quartet Splitting (kcal/mol)	MRPT Singlet-Triplet Splitting (kcal/mol)	# of Determinants	Time for PT correction (min) ^c
² A oxoMn(salen) ⁻¹	CAS	(13,11)	-	-	152,460	313
	ORMAS-3 ^a	$\{d_{Mn}, \sigma, \sigma^*, \pi_1, \pi_1^*, \pi_2, \pi_2^*, \pi_L, \pi_L^*, \pi_R, \pi_R^*\}$	-	-	21,336	47
	ORMAS-6 ^b	$\{d_{Mn}\}, \{\sigma, \sigma^*\}, \{\pi_1, \pi_1^*\}, \{\pi_2, \pi_2^*\}, \{\pi_L, \pi_L^*\}, \{\pi_R, \pi_R^*\}$	-	-	12,582	28
⁴ A oxoMn(salen) ⁻¹	CAS	(13,11)	-6.9	-10.8	76,230	157
	ORMAS-3 ^a	$\{d_{Mn}, \sigma, \sigma^*, \pi_1, \pi_1^*, \pi_2, \pi_2^*, \pi_L, \pi_L^*, \pi_R, \pi_R^*\}$	-6.7	-10.2	11,193	25
	ORMAS-6 ^b	$\{d_{Mn}\}, \{\sigma, \sigma^*\}, \{\pi_1, \pi_1^*\}, \{\pi_2, \pi_2^*\}, \{\pi_L, \pi_L^*\}, \{\pi_R, \pi_R^*\}$	-7.9	-10.4	6,972	16

^aMinimum(maximum) electron occupation restrictions respective to active space: 9,2,2(9,2,2)

^bMinimum(maximum) electron occupation restrictions respective to active space:

1,2,2,2,2(2,4,4,2,2)

^cTotal time for computing PT energy correction on two dual-quad core Intel Xeon R5420 nodes

Table 5: MCSCF vertical ionization potentials (eV) and experimental ionization potentials for *trans*-polyacetylene polymers of length n subunits.

Ethylene subunits	CAS size	ORMAS-SCF			CASSCF	Exp.
		Max = 2	Max = 3	Max = 4		
2	(4,4)	8.44	-	-	8.47	9.09
3	(6,6)	7.71	7.72	7.78	7.78	8.29-8.45
4	(8,8)	7.27	7.22	7.34	7.35	7.8-8.1
5	(10,10)	6.97	6.89	7.06	7.07	-
6	(12,12)	6.77	6.66	6.86	6.87	-
7	(14,14)	6.62	6.48	6.71	6.73	-
8	(16,16)	6.51	6.35	6.60	-	-

Table 6: MRPT vertical ionization potentials (eV) and experimental ionization potentials for *trans*-polyacetylene polymers of length n subunits.

Ethylene subunits	CAS size	ORMAS-PT			MRMP	Exp.
		Max = 2	Max = 3	Max = 4		
2	(4,4)	9.27	-	-	9.11	9.09
3	(6,6)	8.36	8.59	8.62	8.34	8.29-8.45
4	(8,8)	7.92	7.57	7.86	7.88	7.8-8.1
5	(10,10)	7.65	7.62	7.57	7.58	-
6	(12,12)	7.50	7.47	7.36	7.39	-
7	(14,14)	7.41	7.36	7.22	7.27	-
8	(16,16)	7.37	7.30	7.13	-	-

CHAPTER 4. THE DIFFUSION OF GALLIUM ADATOMS ON THE Si(100)-2X1 RECONSTRUCTED SURFACE: AN MCSCF STUDY OF MOLECULAR SURFACE CLUSTERS

A paper to be submitted to *The Journal of Physical Chemistry*

Luke Roskop, James W. Evans, and Mark S. Gordon

Ab initio electronic structure theory was used to model systems that depict Ga and Ga₂ deposition on the Si(100)-2×1 reconstructed surface. A Si₁₅H₁₆ molecular cluster was used to model the Si(100)-2×1 reconstructed surface while a larger Si₁₉₉H₉₂ cluster was used to represent the role of the bulk crystal in the diffusion process. Since the Si(100)-2×1 reconstructed surface is comprised of surface dimers that exhibit a significant amount of diradical character, multi-configuration self-consistent field (MCSCF) methodology was used to treat the relevant potential energy surfaces. Hessian calculations were used to characterize all structures while intrinsic reaction coordinate (minimum energy path) computations were performed to validate the potential energy surface. Dynamic correlation effects were computed at MCSCF optimized structures by multi-reference second-order perturbation theory. Results from the two cluster models were compared to understand the need for including bulk effects in the surface model.

1. Introduction

The deposition of group III metal adatoms onto the Si(100)-2×1 reconstructed crystal surface leads to the formation of 1-D islands.^{1,2,3,4,5} These 1-D islands, which are distinguished as atomic wires, have the potential to serve as interconnects between future nanodevices that are fixed to the Si(100)-2×1 reconstructed surface. How group III metal

adatoms self-assemble into atomic wires is fundamentally a question of surface diffusion. Whether metal adatoms diffuse freely or if their diffusion is mediated by other metal adatoms is an important consideration. An appreciation for the diffusion of metal adatoms on the Si(100)-2×1 reconstructed surface is enhanced if one considers the origin of the high surface reactivity.

The Si(100)-2×1 reconstructed surface has a morphology that is dominated by rows of surface dimers. These surface dimers are comprised of two silicon atoms, each of which has an attached dangling bond that contains a single electron. As a result, each surface dimer may be thought of as a diradical. The diradicaloid nature of the dimers contributes to the high reactivity of the Si(100)-2×1 reconstructed surface (referred to henceforth as the Si(100) surface). The diradical nature of these surface dimers undoubtedly plays a central role in the diffusion process. In fact group III metal adatoms prefer adsorption sites that maximize the interaction with multiple dangling dimer bonds. In what is referred to as the parallel dimer model, rows of metal atoms (atomic wires) form in rows that are perpendicular to the dimer rows. This arrangement maximizes the interaction between each metal adatom and two dangling dimer bonds that originate from adjacent dimers in the same dimer row.^{1,6,7,8,9,10} At low coverage it is understood that no two rows of metal adatoms lie adjacent to one another. This may be the result of an effective repulsion between the atomic wires.¹¹

In effort to understand the surface mediated-diffusion of Ga on the Si(100)-C(2x4) reconstructed surface, previous studies have identified several adsorption sites. A Car-Parrinello study by Takeuchi¹² located two absorption sites referred to as a twofold and a

threefold site (Figure 1: **A**, **B**). Takeuchi predicted that the twofold site (**1B**) lies 0.17 eV (3.9 kcal/mol) lower in energy than the threefold site (**1A**).

More recently, Albao, Hsu, Putungan, and Chuang (AHPC)¹³ examined the diffusion of Ga on a periodic slab model that represented the Si(100)-C(2x4) reconstructed surface. Within the generalized gradient approximation (GGA) to density functional theory (DFT), AHPC located five structures (Figure 1: **B**, **C**, **D**, **E_u**, **E_d**). Two similar structures were reported for **1E** in which the two Si atoms that closely interact with the Ga adatom (Si₂ and Si₇) are buckled upward (**1E_u**) or downward (**1E_d**). AHPC reported that **1C** and **1E_u** are saddle points, **1D** and **1E_d** are metastable, and **1B** is the global minimum energy structure. Relative to the **1B** global minimum, the stability of the remaining structures is as follows: **1B** > **1C** > **1D** > **1E_d** > **1E_u**. Unlike the report from Takeuchi, AHPC did not find a threefold structure (**1A**). AHPC predict the diffusion barriers for Ga adatom parallel and perpendicular to the dimer row to be 6.5 and 7.7 kcal/mol, respectively.

Reliable models of complex chemical behavior must employ a level of theory that can accurately treat the potential energy surface (PES) for the processes under consideration. Since multi-reference behavior is exhibited by transition state structures and the Si(100) surface dimers, an accurate chemical model must have the capability to treat this behavior. Multi-configuration self-consistent field (MCSCF) methods are specifically used to treat chemical systems that exhibit multi-reference (i.e., diradical) behavior. MCSCF methods also have the capability to measure the multi-reference character of their constructed wavefunctions.

From the MCSCF one-particle density matrix, a set of natural orbitals and natural orbital occupation numbers (NOONs) can be generated.¹⁴ NOON values provide a

convenient metric to analyze the diradical character of a system. Diradical character is characterized by NOON values that significantly deviate from the standard restricted open-shell Hartree-Fock (ROHF) occupation numbers of zero, one, or two.¹⁵ For example, consider the π^* natural orbital of the Si_9H_{12} cluster, which is a minimalist representation of a single Si(100) surface dimer (Figure 2). The NOON value for this anti-bonding orbital reveals that it is occupied by approximately one-third of an electron, which is a significant amount of multi-reference character. On the other hand the σ^* natural orbital has a NOON value of ~ 0.02 , which indicates that a negligible amount of multi-reference character originates from this natural orbital.

A reliable surface model should also incorporate subsurface-effects from the bulk crystal as they can affect the PES. One generally attempts to use a model that is physically large enough to avoid edge effects of small molecular clusters, but remain computationally practical within the chosen level of theory. Thus, the physical size of the employed model is a practical consideration as bulk effects are introduced through it.

There are essentially two approaches that are commonly employed to represent crystal surfaces. The first approach uses molecular clusters that best mimic the bare surface. Their inherent simplicity and ability to be treated with standard computational techniques have resulted in their widespread use. The reliability of molecular clusters is questionable since, to some degree, they manifest spurious edge effects. An advantage of clusters is that the use of very accurate electronic structure methods is feasible. To circumvent the edge effects seen in molecular clusters, slab models are commonly used since they incorporate periodic boundary conditions, thereby avoiding undesirable edge effects.¹⁶ Slab models are

typically used with single reference methods like GGA DFT that do not always provide results of sufficient accuracy.

One compromise between simple cluster models and slab models with periodic boundary conditions is the embedded cluster model. One such approach, the surface integrated molecular orbital molecular mechanics (SIMOMM) method, is employed here.¹⁷ The SIMOMM method uses both quantum mechanics (QM) and molecular mechanics (MM), which allows for the treatment of large surface clusters that can be computationally impractical with QM alone. SIMOMM ameliorates the edge effects of a QM cluster by embedding it into a much larger cluster that is treated with MM. The larger MM molecular cluster compensates for the edge effects encountered within the QM molecular cluster. As a result the QM region of the QM/MM cluster better resembles the pristine surface than if one were to treat the QM cluster by itself. An important advantage of embedded cluster models like the SIMOMM method is that the QM component can use any available quantum chemistry method, ranging from GGA DFT to multi-reference techniques.

This paper examines the diffusion of Ga and Ga₂ on Si(100) surface clusters. Various minima and transition state structures are located, which are subsequently connected to map out the PES. In addition, QM and SIMOMM QM/MM results are compared to understand the extent to which the bulk crystal affects the PES.

2. Computational Methods

All results reported here have been obtained from either QM or hybrid QM/MM methodology. The QM cluster, Si₁₅H₁₆ (Figure 3A), is constructed with the minimum number of atoms that can adequately represent two Si(100) surface dimers. Bulk-effects are considered using a larger QM/MM cluster, Si₁₉₉H₉₂ (Figure 3B). The QM/MM cluster

represents a region of the Si(100) surface that is 11 layers deep and contains 12 surface dimers. The reactive region of the QM/MM cluster is the same two-dimer ($\text{Si}_{15}\text{H}_{16}$) QM cluster seen in Figure 3A, which is represented by the red atoms in Figure 3B. The QM/MM model is constructed by the SIMOMM method,¹⁷ which mechanically embeds the $\text{Si}_{15}\text{H}_{16}$ QM cluster into the larger $\text{Si}_{199}\text{H}_{92}$ QM/MM cluster. The MM component of the QM/MM cluster is optimized using the MM3¹⁸ force field parameters in the Tinker program.¹⁹ To save space, all structures that correspond to the $\text{Si}_{199}\text{H}_{92}$ QM/MM cluster are represented by the embedded QM region ($\text{Si}_{15}\text{H}_{16}$).

The complete active space self-consistent field (CASSCF)^{20,21} method is used to treat all QM atoms. For structures that correspond to the diffusion of a single Ga adatom, a complete active space (CAS) is constructed with the $\sigma, \pi, \pi^*, \sigma^*$ orbitals from each Si-Si dimer and the 3s, 3p_x, 3p_y, 3p_z orbitals from the Ga adatom. This 11 electrons in 12 orbitals active space is referred to as a CAS(11,12) active space. If this active space were expanded to accommodate orbitals and electrons from an additional Ga adatom, the resultant active space would be computationally impractical. Therefore some of the orbitals in the would-be active space must be excluded. Consider the diffusion of a single Ga adatom: when the Si-Si dimer bond is stretched farthest on the PES, the NOON values of the σ/σ^* orbitals centered on the surface dimers are $\sim 1.98/\sim 0.02$. These NOON values indicate that a negligible amount of multi-reference character originates from the σ/σ^* orbitals. Because of this, the σ/σ^* orbitals were excluded from the larger active space. For the Ga_2 calculations, a CAS was constructed with the π, π^* orbitals from each Si-Si dimer and the 3s, 3p_x, 3p_y, 3p_z orbitals from each Ga adatom. This results in a CAS(10,12) active space.

All CASSCF minima and transition state structures were confirmed as stationary points by diagonalizing the Hessian (matrix of second order energy derivatives). Transition states were connected to their respective reactants and products by computing the intrinsic reaction coordinate (IRC),²² also referred to as the minimum energy path (MEP). All IRC calculations were performed using the GS2 algorithm²³ with a range of step sizes from 0.05-0.3 amu^{1/2}-bohr. Dynamic correlation effects were computed by second-order multi-reference Møller-Plesset (MRMP2) perturbation theory^{24,25} at the final CASSCF geometries (MRMP2//CASSCF). The 6-31G(d) all electron basis set²⁶ was used for all Si and Ga atoms. The General Atomic Molecular Electronic Structure System (GAMESS)²⁷ was used for all QM calculations while the GAMESS/Tinker interface was used for all SIMOMM computations. It is important to note the model systems used here cannot determine diffusion barriers that correspond to the migration of Ga adatom between adjacent dimer rows.

3. Results and Discussion

3A. Ga adsorption on Si(100)

Figures 4 and 5 display doublet and quartet potential energy surfaces (PESs) that depict absorption sites for Ga adatom on the Si₁₅H₁₆ QM and Si₁₉₉H₉₂ QM/MM molecular clusters, respectively. Results for the smaller QM cluster are presented first. Three local minima (LM: **on-top**, **threefold**, **pseudo off-center**) and five transition states (TS) are found on the QM doublet surface at the CASSCF level of theory. All energies in Figure 4 are relative to the doublet **on-top** structure. MRMP2//CASSCF energy corrections (in parentheses) indicate that the **threefold** site is the global minimum energy structure. The MRMP2 single point energies suggest that the addition of dynamic correlation modifies the nature of the doublet potential energy surface.

The **off-center** adsorption site (Figure 1B) is similar to the structure found by Takeuchi and AHPC. Takeuchi and AHPC report that the **off-center** adsorption site is a minimum; however, the CASSCF **off-center** structure is a transition state. This discrepancy may be a consequence of the first principles methodology used by Takeuchi and AHPC, which accounted for dynamic correlation effects. The **off-center** structure may be a minimum on the MRMP2 surface as MRMP2//CASSCF relative energies predict that the **off-center** structure is 0.1 kcal/mol lower in energy than the **on-top** structure.

The **threefold** adsorption site (Figure 1A) found in this work is similar to the structure found by Takeuchi. Takeuchi reports the **off-center** structure is 3.9 kcal/mol lower in energy than the **threefold** structure. In contrast, MRMP2//CASSCF indicates the **threefold** site is 6.7 kcal/mol lower in energy than the **off-center** site.

The **on-dimer** adsorption site (Figure 1C) is similar to the structure found by AHPC. AHPC predicted the **off-center** site to be lower in energy than the **on-dimer** site by 6.5 kcal/mol, whereas MRMP2//CASSCF finds that the **on-dimer** site is lower in energy than the **off-center** site by 3.4 kcal/mol. These discrepancies are most likely related to the inability of single determinant GGA DFT methods to capture the significant diradical character of many of the species considered here.

Two paths on the QM doublet surface (Figure 4) describe the migration of a Ga adatom from one surface dimer to the other. While the minimum energy paths were determined at the CASSCF level of theory, the discussion here will refer to the MRMP2 single point energies, since they are more reliable. Both paths begin at an **on-top** structure; pass through **pseudo-off-center** and **off-center** structures; and ultimately end at an adjacent **on-top** structure. The difference between the two paths is the route from the **on-top** structure

to the **pseudo-off-center** structure. The lower-energy path proceeds through an **on-top**→**pseudo-off-center** transition state to a **pseudo-off-center** structure. The higher-energy path is a two-step process in which the Ga adatom passes through an **on-top**→**threefold** transition state to a **threefold** structure; then the Ga adatom proceeds through a **threefold**→**pseudo-off-center** transition state to the **pseudo-off-center** structure. Relative to the **on-top** structure, there appears to be no net energy barrier for the lower-energy path, while the higher-energy path encounters a net 5.7 kcal/mol MRMP2 energy barrier.

The Ga adatom also diffuses between two **on-top** sites located at either side of the same dimer (see Fig. 4). These two sites are connected by an **on-dimer** structure, which is found to be a transition state at the CASSCF level of theory. However, the MRMP2//CASSCF relative energies indicate that the **on-dimer** structure is 3.5 kcal/mol *lower* in energy than the **on-top** (CASSCF) local minimum it is connected to. This suggests that at the MRMP2 level of theory, the **on-dimer** structure may not be a transition state.

The MRMP2//CASSCF doublet potential energy surface (PES) is much flatter than is the corresponding CASSCF PES, suggesting a facile diffusion process. The doublet **on-top** site is the highest energy structure a Ga adatom will encounter for surface diffusion along a row of surface dimers. On the lower-energy doublet path, all species are within a 3.5 kcal/mol range, while on the higher energy path, only the **threefold** and the **threefold** → **pseudo-off-center** TS are outside this energy range.

Natural orbital occupation numbers (NOONs) are reported in Table 1 for all QM structures. The NOONs for a single determinant wavefunction should all be very close to integers. For doublet and quartet states, each NOON should have a value of 2 or 1 for occupied orbitals and 0 for virtual orbitals. Clearly, many NOON values deviate significantly

from integer values, indicating significant diradical character, and therefore significant multi-reference character in the corresponding wavefunctions. The **threefold** structure exhibits the least amount of diradical character, with NOONs of 1.90, 1.00, and 0.10. Interestingly, the lowest energy MRMP2 structures are those for which the Ga adatom maximizes its interaction with more than one dangling dimer bond, thereby decreasing the diradical (multi-reference) character. This is also apparent from the PT energy corrections that are listed in Table 1.

Two minima (**on-top** and **off-center**) and two transition states are found on the QM (CASSCF) quartet PES (Figure 4). Relative to the energy of the doublet **on-top** structure, MRMP2//CASSCF relative energies predict that the **off-center** structure is the quartet global minimum energy structure. The MRMP2 relative energies of the quartet **on-dimer**, **on-top**→**pseudo-off-center TS**, and **off-center** structures are lowered relative to the CASSCF energies. These three structures correspond to arrangements in which the Ga adatom interacts with two dangling dimer bonds. The relative energy of the **on-top** structure, which interacts with just a single dangling dimer bond, increases when dynamic correlation is introduced.

NOON values (Table 1) indicate that the CASSCF structures on the quartet surface are tri-radicals, with three NOON=1.0. The quartet NOON values do not significantly deviate from the restricted open shell Hartree-Fock occupation numbers (two, one, zero). This indicates that a multi-reference treatment is less critical for the quartet structures.

Now, consider the QM/MM SIMOMM clusters. Figure 5 displays the doublet and quartet PESs that depict adsorption sites of a single Ga adatom on the Si₁₉₉H₉₂ QM/MM cluster (Figure 2B). Two minima and one transition state are found on the doublet surface. Attempts to locate a **threefold** structure have been unsuccessful; however, it may exist on the

MRMP2 surface since MRMP2//CASSCF relative energies indicate that it is the global minimum for the smaller QM cluster (Figure 4).

The CASSCF **on-dimer** structure is a minimum on the QM/MM doublet surface. This observation is in contrast with the QM-only model in which the CASSCF **on-dimer** structure is a transition state. Attempts to locate a QM/MM **on-dimer**→**on-top** transition state were unsuccessful. The difficulty associated with the location of an **on-dimer**→**on-top** transition state is probably the result of a small energy barrier (< 0.1 kcal/mol) relative to the **on-dimer** structure. Since MRMP2//CASSCF relative energies indicate that the **on-dimer** site is the global minimum energy structure, it is likely that the **on-dimer**→**on-top** TS structure will have a relative energy that is similar to that of the **on-dimer** site.

There is a 0.7 kcal/mol energy barrier that connects **on-top** sites on adjacent surface dimers. This is in contrast to the QM-only cluster results, since the order of the MRMP2//CASSCF relative energies between the **on-top** and **off-center** structures is switched. However this is not unreasonable since the energy difference between the **on-top** and **off-center** structures in the QM and QM/MM models is small (≤ 0.7 kcal/mol). It is clear that both the QM and QM/MM doublet PESs are flat in the region between the **on-top** and **off-center** structures, which indicates that the Ga adatom readily diffuses along the dimer rows.

Two minima and two transition states are reported on the QM/MM quartet surface (Figure 5). Attempts to locate an **on-dimer**→**on-top** TS on this PES have also been unsuccessful. MRMP2//CASSCF relative energies indicate that the **off-center** adsorption site is the global minimum energy structure. Relative to the energy of the **on-top** site, the relative energies of those structures that associate Ga adatom with more than one dangling dimer

bond are lowered when dynamic correlation is introduced, while the relative energy of the **on-top** structure associated with one dangling dimer bond increases. The QM/MM NOON values (Table 1) for all structures indicate little need for a multi-reference treatment.

3B. Ga₂ on Si(100)

This section is split into three subsections: First, the diffusion of two Ga adatoms that are not bonded to one another is considered. Next, the formation of Ga₂ dimer is examined. The last subsection examines the rotation of the Ga₂ dimer. Each subsection presents QM cluster results followed by the SIMOMM QM/MM cluster results. The red numbers in Figure 6 are used to identify structures that involve two Ga adatoms. These numbers specify the position of each Ga adatom relative to the Si₁₅H₁₆ QM cluster. For example, the **5-6** label (see Figure 7) refers to the local minimum structure in which one Ga adatom is at the ‘5’ position and another is at the ‘6’ position. If the label contains a ‘→’ then the structure is a transition state. For example, the **5-2→5-1** label refers to the transition state structure that connects local minima **5-2** and **5-1**.

Potential Energy Surface for adsorption. Figure 7 displays the stationary points on the singlet and triplet potential energy surfaces for adsorption of two separated Ga adatoms on the Si₁₅H₁₆ QM cluster. These PESs describe the diffusion of one Ga adatom *while* the other Ga adatom is fixed at the ‘5’ position. Four minima and three transition states were found on both the singlet and triplet PESs. All energies in Figure 7 are reported relative to the singlet **5-6** structure.

There are significant differences in the CASSCF and MRMP2//CASSCF potential energy surfaces. On the former, the global minimum is the **5-6** structure, but the relative energy of this diradicaloid species is likely to increase when dynamic correlation is

introduced, and this is indeed the case. Interestingly, the MRMP2//CASSCF global minimum is the **5-6→5-4** structure, which is a TS on the CASSCF PES. Relative to the **5-6→5-4** structure, the singlet surface becomes increasingly repulsive (up to 17.6 kcal/mol) as the system evolves to the **5-1** structure. The high relative energies of most of the structures along this reaction path correlate with an increase in diradical character (Table 2). The high relative energies of the **5-2** (16.7 kcal/mol), **5-2→5-1** (14.4 kcal/mol), and **5-1** (17.6 kcal/mol) structures indicate that the two Ga adatoms prefer arrangements that maximize their interaction with the same surface dimer (or with each other).

Except for the **5-6** structure itself, the impact of dynamic correlation on the triplet PES is much less than that on the singlet PES. The MRMP2//CASSCF relative energies indicate that the **5-4** structure is the triplet global minimum. Both the CASSCF and MRMP2//CASSCF levels of theory predict that the singlet and triplet PESs are essentially degenerate at the **5-2**, **5-2→5-1** TS, and **5-1** structures. The singlet and triplet NOON values (Table 2) indicate that all three species are nearly pure diradicals on the singlet surface and pure diradicals on the triplet PES.

Now consider the QM/MM cluster. Figure 8 displays singlet and triplet surfaces that depict absorption sites of two separated Ga adatoms on the QM/MM cluster. All energies in Figure 8 are reported relative to the singlet **5-6** structure. Unlike the Si₁₅H₁₆ QM cluster, attempts to locate both a **5-6→5-4** and **5-4** structure on the singlet QM/MM surface have been unsuccessful. It is possible that bulk effects influence the CASSCF surface such that it is very flat in this region. MRMP2//CASSCF energies indicate that the **5-6** structure is the global minimum. This agrees with the notion that the more stable structures correspond to geometrical arrangements in which Ga adatoms interact with the same surface dimer.

Four minima and three transition states are found on the triplet QM/MM surface. These transition states and minima closely correspond with those found for the QM cluster. MRMP2//CASSCF energies indicate the **5-4** structure is the triplet global minimum. The stability of this structure may be related to the **5-4** arrangement of Ga adatoms such that they optimally interact with three of the four dangling dimer bonds.

Ga₂ dimer formation. Figure 9 displays singlet and triplet CASSCF surfaces that depict the formation of the Ga₂ dimer on the QM cluster. Whenever a structure corresponds to a situation in which the Ga adatoms are considered to be bonded to each other, a “**B**” is added to the label. For example, **5-4B** (see Figure 9) indicates that the adatoms at the **4** and **5** positions are bonded to one another. All energies in Figure 9 are relative to the singlet **5-6** structure.

The singlet QM surface illustrates that the Ga adatoms in the **5-4** structure can form a Ga₂ dimer via the **5-4**→**5-4B** transition state structure. Relative to the **5-4** structure, the **5-4B** structure is lower in energy by 25.6 kcal/mol. Once dynamic correlation is introduced via MRMP2 calculations, there appears to be no barrier that prevents the formation of the Ga₂ dimer. This suggests that the two Ga adatoms will spontaneously form Ga₂ dimer when they approach each other on the Si(100) surface. NOON values (Table 2) show that the **5-4B** structure has little multi-reference character, which is consistent with the large energy lowering upon the Ga-Ga bond formation.

The triplet QM surface is much flatter than the singlet surface, demonstrating little energetic preference for the bonded vs. nonbonded structures. For example, the **5-4B** triplet species is less than 10 kcal/mol lower in energy than **5-4**, and there is a small barrier separating the two species. The triplet surface also has a second route, in which the two Ga

adatoms diffuse from the **5-4** species to the **3-4** structure. This pathway has no intervening MRMP2//CASSCF energy barrier. At this level of theory, the **3-4** structure is higher in energy than the **5-4B** structure by just 0.3 kcal/mol.

Figure **10** displays singlet and triplet CASSCF surfaces that depict the formation of Ga₂ dimer on the QM/MM cluster. All energies in Figure **10** are reported relative to the singlet **5-6** structure. On the QM/MM singlet surface, the **5-4B** structure is formed from the **5-6** structure via the **5-6**→**5-4B** transition state. Both the QM and QM/MM pathways form a Ga₂ dimer without an energy barrier. The **5-4B** structure is favored over the **5-6** structure by 11.1 kcal/mol. As for the QM-only species, the **5-4B** structure has little multi-reference character, as shown in Table **2**. The MRMP2//CASSCF energies indicate that the most favorable arrangement of the Ga adatoms occurs when: **1)** Ga adatoms are dimerized and **2)** the Ga₂ dimer maximizes its interaction with the dangling dimer bonds.

The triplet QM/MM surface is similar to the triplet QM-only surface, showing little preference for bonded vs. diradicaloid species. From the **5-4** local minimum, the Ga adatoms dimerize to form the **5-4B** structure (Ga₂ dimer) without a MRMP2//CASSCF energy barrier. The Ga adatoms can also form triplet **3-4** without an energy barrier. The lowest energy structure on the triplet surface is predicted to be **5-4B** (-2.3 kcal/mol), but this structure is only 1 kcal/mol lower in energy than the **3-4** structure.

Ga₂ dimer rotation. Figure **11** displays the singlet and triplet CASSCF potential energy surfaces that depict the rotation of a Ga₂ dimer on the QM cluster. These surfaces examine the rotational mobility of a Ga₂ dimer on the Si(100) surface. All energies in Figure **11** are reported relative to the singlet **5-6** structure.

The **5-4B** structure is the singlet global minimum. From **5-4B** the Ga₂ dimer can rotate into either the **3-4B** or **7-9B** structures. The MRMP2//CASSCF energies increase by about 5 kcal/mol as the Ga₂ dimer rotates from the **5-4B** structure through the **5-4B**→**3-4B** transition state to the **3-4B** structure. Although a QM transition state that connects the **5-4B** structure to the **7-9B** structure has yet to be found, it may exist as this transition state was found on the QM/MM CASSCF surface. Singlet NOON values, summarized in Table 2, demonstrate that the structures that contain the Ga₂ dimer have less diradical character than do structures that have separated Ga adatoms, and therefore these Ga-Ga bonded species have lower MRMP2//CASSCF energies. On the triplet PES, starting from **5-4B**, the Ga₂ dimer can rotate to form the **5-7B** structure, with an energy increase of about 12.5 kcal/mol. No other stationary points have been found on the triplet PES.

Figure 12 displays the singlet and triplet CASSCF QM/MM PESs for the rotation of the Ga₂ dimer. All energies in Figure 12 are reported relative to the singlet **5-6** structure. From the **5-4B** structure, the Ga₂ dimer can rotate to the singlet global minimum **3-4B** structure without a MRMP2//CASSCF energy barrier. The **3-4B** structure closely resembles the parallel dimer model, consistent with experimental observations. Alternatively, the Ga₂ dimer in the **5-4B** structure can also rotate to the **7-9B** structure, but this rotation must surmount a 10.5 kcal/mol MRMP2//CASSCF energy barrier.

As noted above for the QM-only species, and for similar reasons, the **7-9B** and **3-4B** NOON values (Table 2) demonstrate little multi-reference character. The triplet QM/MM surface is very similar to the triplet QM-only surface. As the Ga₂ dimer rotates from the **5-4B** structure to the **5-7B** structure the energy of the system increases.

5. Comparison of QM and QM/MM treatments.

Table 3 displays differences in relative energies between doublet and quartet structures that are common to both the QM-only and QM/MM models. The largest relative MRMP2//CASSCF energy difference for the doublet (quartet) structures is -0.8 kcal/mol (-2.1 kcal/mol). The mean absolute differences (MAD) in the CASSCF and MRMP2//CASSCF relative energies are 1.3 kcal/mol and 0.8 kcal/mol, respectively. These small energy differences suggest that adding bulk via the MM atoms has only a modest effect on the relative energies. The largest energy difference occurs for the **off-center** structure, due in part to the more rigid QM/MM surface. In the QM **off-center** structure, the Si₁₅H₁₆ cluster can collapse to allow for a more favorable interaction between the dangling dimer bonds at each Si(100) surface dimer and the Ga adatom.

Table 4 displays differences in relative energies between singlet and triplet structures that are common to QM and QM/MM models. The largest relative MRMP2//CASSCF energy difference for the singlet (triplet) structures is -15.2 kcal/mol (7.3 kcal/mol). The mean absolute difference in both the CASSCF and MRMP2//CASSCF relative energies is 2.3 kcal/mol. The largest energy difference occurs for structure **5-4B**.

The QM/MM model predicts the **3-4B** structure to be the global minimum energy structure, which corresponds to the parallel dimer model, whereas the QM model predicts the **5-4B** structure to be the global minimum energy structure. This suggests that bulk effects are necessary to stabilize the **3-4B** structure and to bring the calculations into agreement with experimental observations.

Figure 13 compares the QM part of the QM and QM/MM singlet **5-4B** structures. The QM-only structure appears to be twisted. The bulk support structure (MM region) in the

QM/MM model corrects the QM region and the surface cluster looks more symmetric. This demonstrates the importance of incorporating bulk effects in the surface model.

5. Conclusions

Ab initio electronic structure calculations were performed to develop an understanding of the diffusion of Ga and Ga₂ on the Si(100)-2×1 reconstructed surface. These processes were modeled using QM (Si₁₅H₁₆) and SIMOMM QM/MM (Si₁₉₉H₉₂) molecular clusters. The diffusion of Ga adatoms and the Ga₂ dimer along the Si(100) dimer row was investigated.

Structures similar to the ones found by Takeuchi and AHPC were observed in this work, with differences primarily in the energy ordering among the structures. Both Takeuchi and AHPC reported the off-center structure as a minimum energy structure, but in the present work the off-center structure is found to be a transition state by both the QM and QM/MM cluster models. Both Takeuchi and AHPC predicted that the off-center structure is the global minimum; here the three-fold structure is found to be the QM minimum while the on-dimer structure is predicted to be the QM/MM minimum. AHPC predict that the on-dimer structure is a transition state, which agrees with the QM cluster model used here. On the other hand, the QM/MM cluster model predicts the on-dimer site to be a minimum energy structure. In any event, the low MRMP2 relative energies from both the QM and QM/MM models would seem to indicate that the on-dimer site is a minimum on the potential energy surface.

The order of stability for structures that are common to both QM and QM/MM models is inconsistent. QM/MM energies predict that the **3-4B** structure is the singlet global minimum. No QM/MM energy barriers were found for structures that lead to the **3-4B** structure. This indicates Ga adatoms self-assemble into atomic wires, consistent with

experimental observations. On the other hand, MRMP2//CASSCF relative energies indicate an energy penalty in the QM-only cluster as the Ga₂ dimer is rotated from the **5-4B** position to the **3-4B** position. This demonstrates the need for surface models that consider bulk effects.

The doublet/quartet surfaces that depict Ga adatom diffusion indicate the QM-only **on-dimer** sites (Figure 4,5) are transition states while the QM/MM model indicates they are minima. In addition, the QM-only and QM/MM geometries have noticeable differences, because the QM cluster does not have sufficient structural rigidity. Compared to the SIMOMM model, the QM structures in which a Ga adatom or a Ga₂ dimer span more than one surface dimer have the largest distortions in geometries.

Some aspects of the QM-only and QM/MM potential energy surfaces are in qualitative agreement. Relative energies for structures in which Ga adatoms are separated appear to be insensitive to the presence of bulk MM atoms. Both the QM and QM/MM models demonstrate that pairs of Ga adatoms spontaneously form a Ga₂ dimer when they approach one another. Both models also predict that a Ga adatom freely diffuses along the dimer row.

In both QM and QM/MM models, the most energetically stable structures correlate with small diradical (i.e., nearly closed shell) character. These structures correspond to arrangements of Ga adatoms or Ga₂ dimer that maximize the interaction with the dangling dimer bonds. In addition, the formation of the Ga₂ dimer bond surely plays an important role in the stabilization of the surface clusters investigated here.

Acknowledgements

This work was supported by grants from the Air Force Office of Scientific Research (LR) and from the Basic Energy Sciences Division of the Department of Energy (MSG, JWE) to the Ames Laboratory, administered by Iowa State University. Enlightening discussions with Dr. Deborah Zorn and Professor Yingbin Ge are gratefully acknowledged.

References

- ¹J. Nogami, A. A. Baski, C. F. Quate, Phys. Rev. B **44**, 1415 (1991).
- ²J. Nogami, S.-I. Park, C. F. Quate, Appl. Phys. Lett. **53**, 2086 (1988).
- ³J. Nogami, “Atomic and Molecular Wires”, C. Joachim, S. Roth (Eds.), NATO ASI Series E, Kluwer, Dordrecht, 1997; Vol. 341, p 11.
- ⁴M. M. Evans, J. Nogami, Phys. Rev. B, **59**, 7644 (1999).
- ⁵H. Itoh, J. Itoh, A. Schmid, T. Ichinokawa, Phys. Rev. B **48**, 14663 (1993).
- ⁶G. Brocks, P. J. Kelly, R. Car, Phys. Rev. B **70**, 2786 (1993).
- ⁷J. E. Northrup, M. C. Schabel, C. J. Karlsson, R. I. G. Uhrberg, Phys. Rev. B **44**, 13799 (1991).
- ⁸B. G. Adams, I. F. Sankey, J. Vac. Sci. Technol. A **10**, 2046 (1992).
- ⁹H. Sakama, K. Murakami, K. Nishikata, A. Kawazu, Phys. Rev. B **50**, 14977 (1994).
- ¹⁰B. E. Steele, L. Li, J. L. Stevens, I. S. T. Tsung, Phys. Rev. B **47**, 9925 (1993).
- ¹¹M. A. Albao, M. M. R. Evans, J. Nogami, D. Zorn, M. S. Gordon, J. W. Evans, Phys. Rev. B **72**, 35426 (2005).
- ¹²N. Takeuchi, Phys. Rev. B **63**, 35311 (2000).
- ¹³M. A. Albao, C. Hsu, P. B. Darwin, C. Chuang, Surface Science **604**, 396 (2010).
- ¹⁴P.-O. Löwdin, Phys. Rev. **97**, 1474 (1955).

- ¹⁵M. S. Gordon, M. W. Schmidt, G. M. Chaban, K. R. Glaesemann, W. J. Stevens, C. J. Gonzalez, *Chem. Phys.* **110**, 4199 (1999).
- ¹⁶R. Dovesi, B. Civalleri, R. Orlando, C. Roetti, V. R. Saunders, "Reviews in Computational Chemistry" edited by K. B. Lipkowitz, R. Larter, T. R. Cundari, Wiley, New York, 2005, Vol. 21, Chap. 1.
- ¹⁷J. R. Shoemaker, L. W. Burggraf, M. S. Gordon, *J. Chem. Phys. A.* **103**, 3245 (1999).
- ¹⁸J. H. Lii, N. L. Allinger, *J. Am. Chem. Soc.* **111**, 8566 (1989). J. H. Lii, N. L. Allinger, *J. Am. Chem. Soc.* **111**, 8576 (1989). N. L. Allinger, Y. H. Yuh, J. H. Lii, *J. Am. Chem. Soc.* **111**, 8551 (1989).
- ¹⁹C. E. Kundrot, J. W. Ponder, F. M. Richards, *J. Comput. Chem.* **12**, 402 (1991). J. W. Ponder, F. M. Richards, *J. Comput. Chem.* **8**, 1016 (1987).
- ²⁰P. E. Seigbahn, A. Herberg, B. O. Roos, B. Levy, *Phys. Scr.* **21**, 323 (1980).
- ²¹K. Ruedenberg, K. R. Sundberg, "Quantum Science" edited by J-L. Calais, O. Goscinski, J. Lindenberg, Y. Öhrn (Plenum, New York, 1976) p 505.
- ²²B. C. Garrett, M. K. Redmon, R. Steckler, D. G. Truhlar, K. K. Baldridge, D. Bartol, M. W. Schmidt, M S. Gordon, *J. Phys. Chem.* **92**, 1476 (1988).
- ²³C. Gonzales, H. B. Schlegel, *J. Chem. Phys.* **90**, 2154 (1989).
- ²⁴K. Hirao, *Chem. Phys. Lett.* **190**, 375 (1992).
- ²⁵C. Møller, M. S. Plesset, *Physical Review* **46**, 618 (1934).
- ²⁶W. J. Hehre, R. Ditchfield, J. A. Pople, *J. Chem. Phys.* **56**, 2257 (1972). M. S. Gordon, *Chem. Phys. Lett.* **76**, 163 (1980). V. A. Rassolov, M. A. Ratner, J. A. Pople, P. C. Redfern, L. A. Curtiss, *J. Comp. Chem.* **22**, 976 (2001).

²⁷ M. W. Schmidt, K. K. Baldridge, J. A. Boatz, S. T. Elbert, M. S. Gordon, J. H. Jensen, S. Koseki, N. Matsunaga, K. A. Nguyen, S. Su, T. L. Windus, M. Dupuis, J. A. Montgomery, J. Journal of Computational Chemistry **14** 1347 (1993). M. S. Gordon, M. W. Schmidt, “Theories and Applications of Computational Chemistry, the First Forty Years” C. E. Dykstra, G. Frenking, K. S. Kim, G. E. Scuseria (Eds.) Elsevier, Amsterdam, 2005, pp 1167-1189.

Figure 1: A) Threefold structure predicted by Takeuchi, B) twofold structure predicted by Takeuchi and AHPC, C) on-dimer structure predicted by AHPC, D) hollow site predicted by AHPC, and E) cave site predicted by AHPC. In E there are two possible structures in which atoms Si₂ and Si₇ are buckled upward (E_u) or buckled downward (E_d).

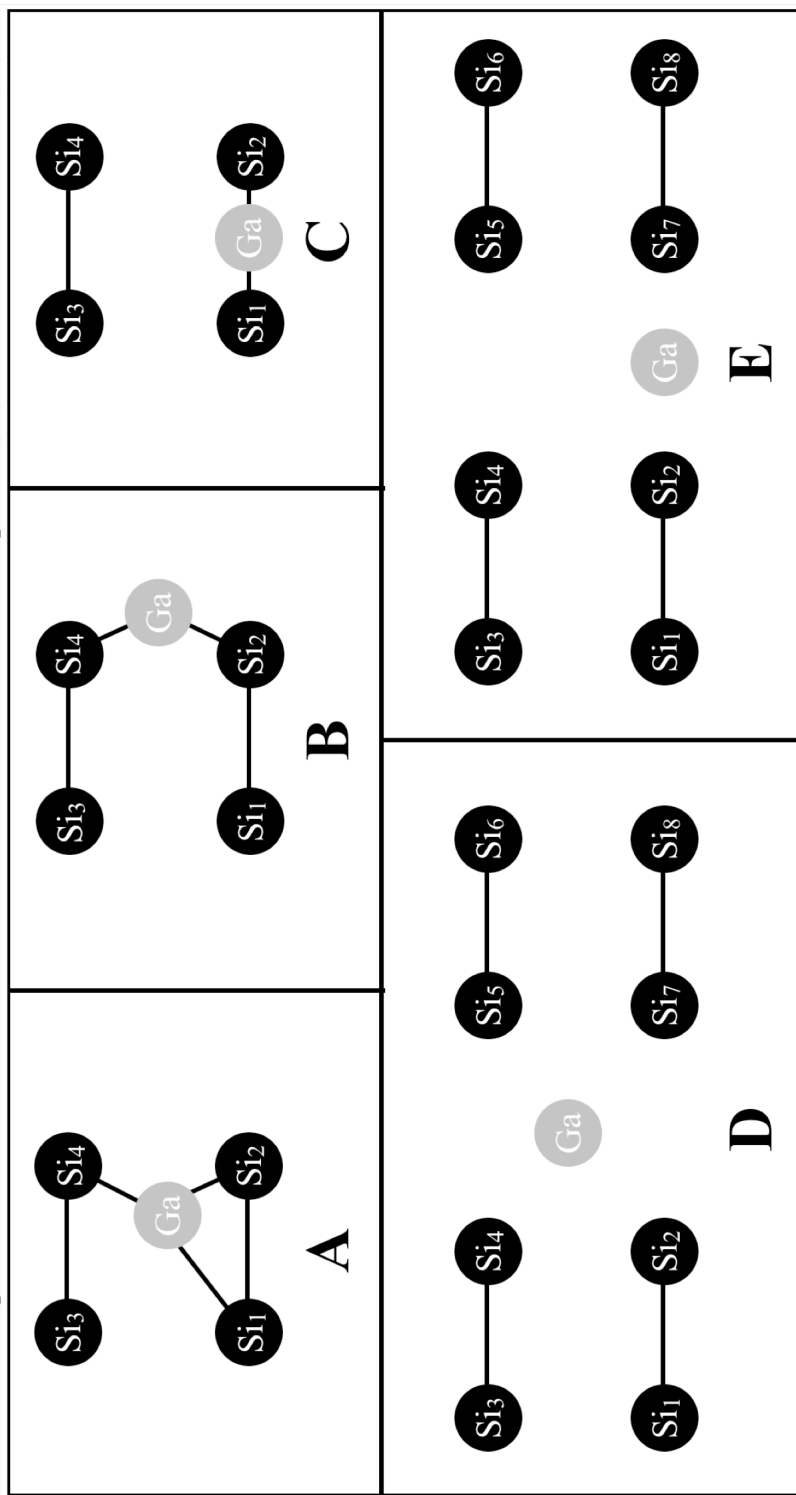


Figure 2: $\sigma, \pi, \pi^*, \sigma^*$ natural orbitals of Si_9H_{12} . The π (π^*) natural orbital has a NOON value of ~ 1.66 (~ 0.33). The σ (σ^*) natural orbital has a NOON value of ~ 1.98 (~ 0.02).

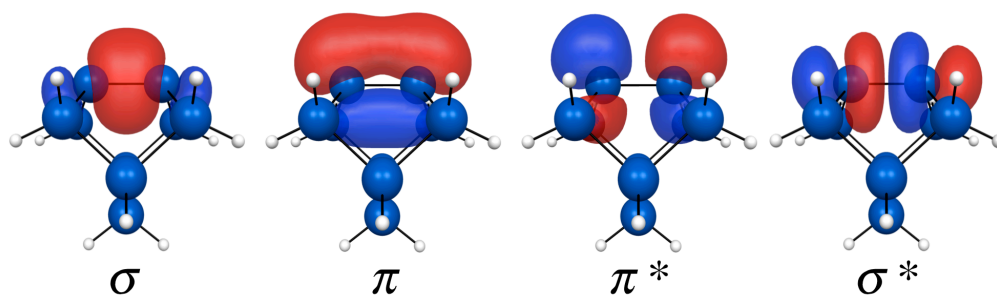


Figure 3: Molecular clusters used to examine Ga and Ga₂ surface diffusion. **A)** Si₁₅H₁₆ cluster treated with QM only. **B)** Si₁₉₉H₉₂ cluster treated with QM/MM. In model **B** the Si₁₅H₁₆ QM region is indicated by red colored atoms.

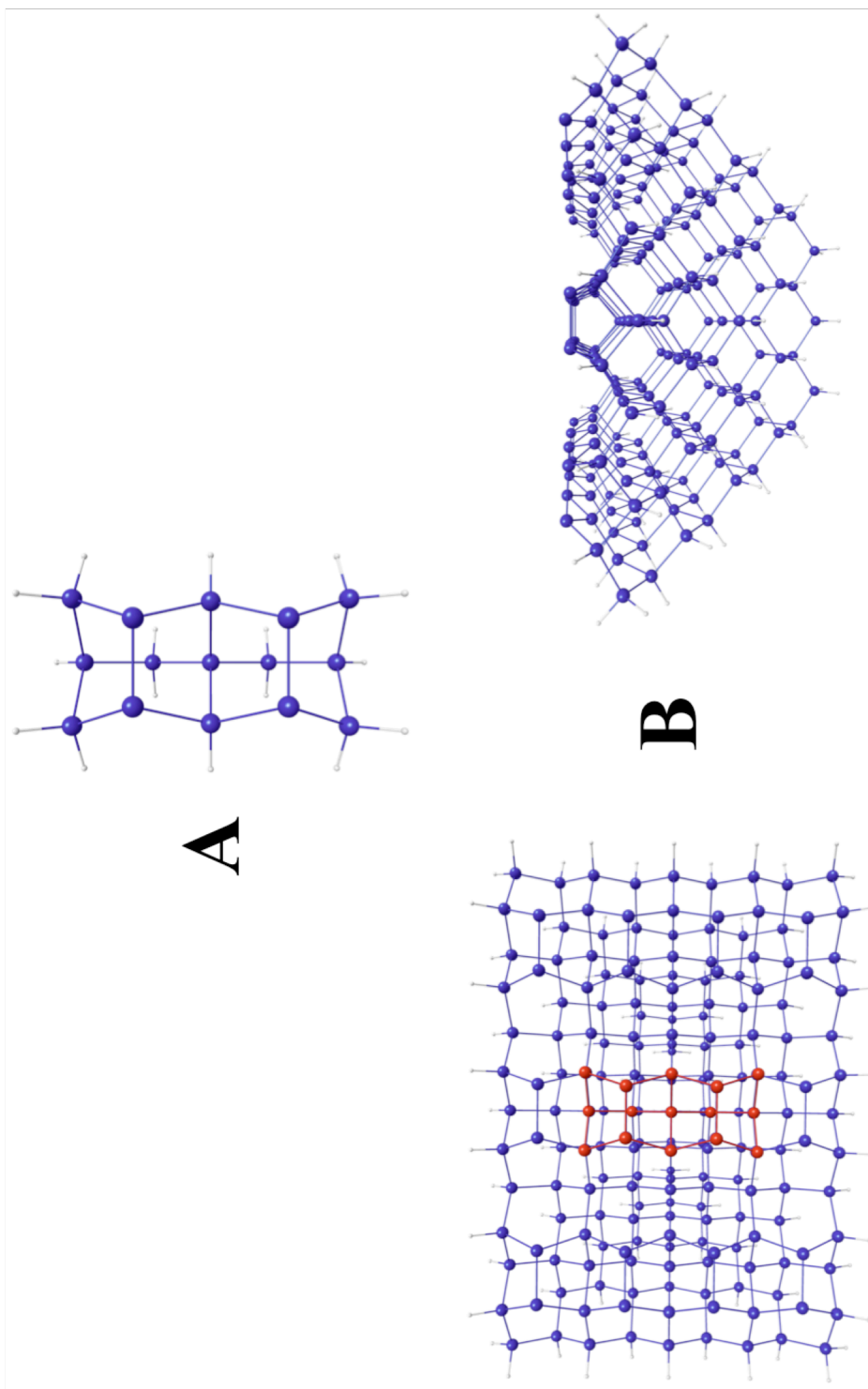


Figure 4: Doublet and quartet potential energy surfaces that depict the diffusion of Ga adatom on the $\text{Si}_{15}\text{H}_{16}$ QM cluster. MRMP2//CASSCF energies are in parentheses. All energies are relative to the doublet **on-top** structure. Energies are in kcal/mol.

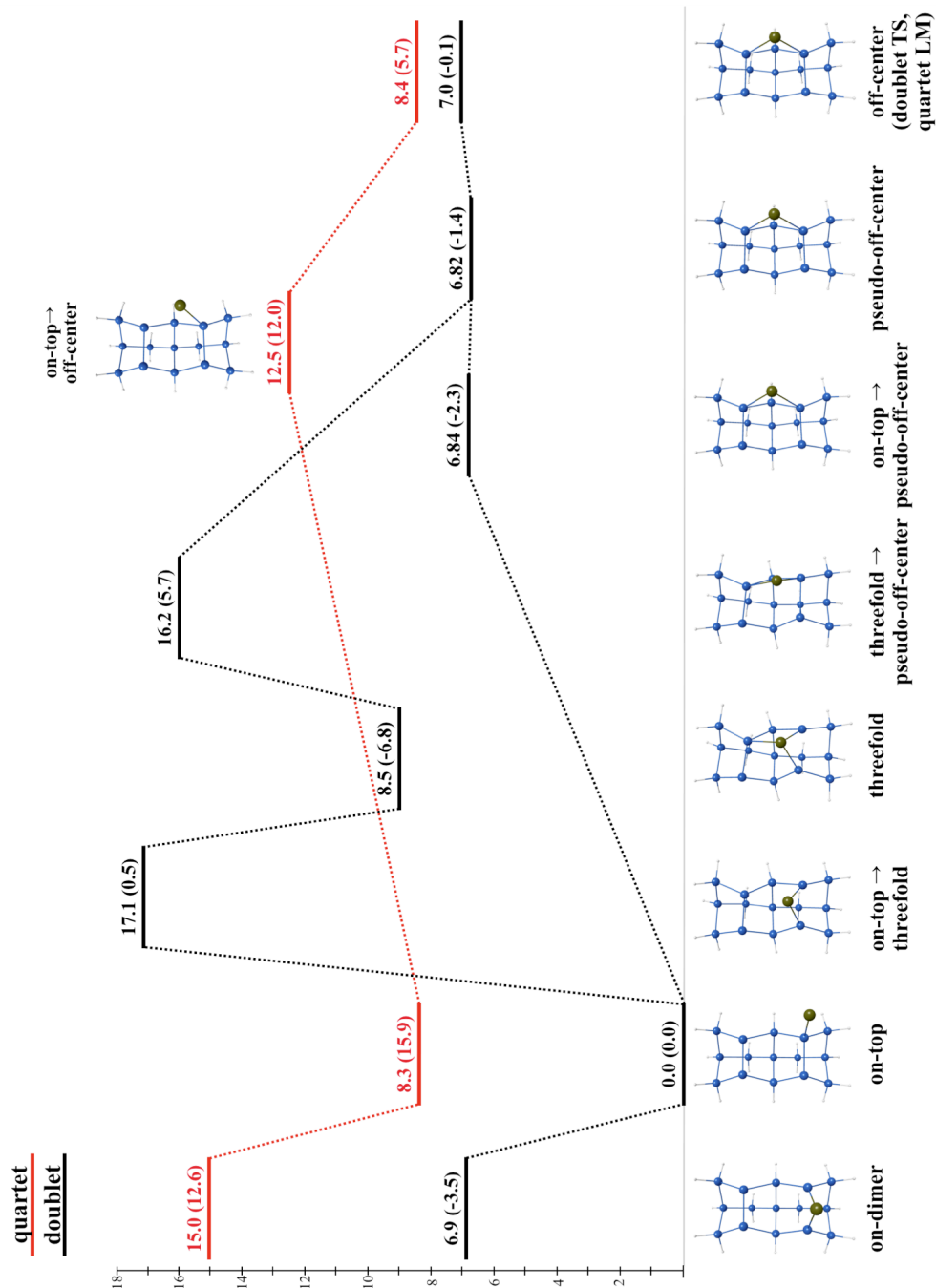


Figure 5: Doublet and quartet potential energy surfaces for the diffusion of Ga adatom on the $\text{Si}_{199}\text{H}_{92}$ QM/MM cluster. MRM2//CASSCF energies are in parentheses. All energies are relative to the doublet **on-top** structure. Energies are in kcal/mol. † indicates no CASSCF transition state structure was found. The MM region of QM/MM model is not shown.

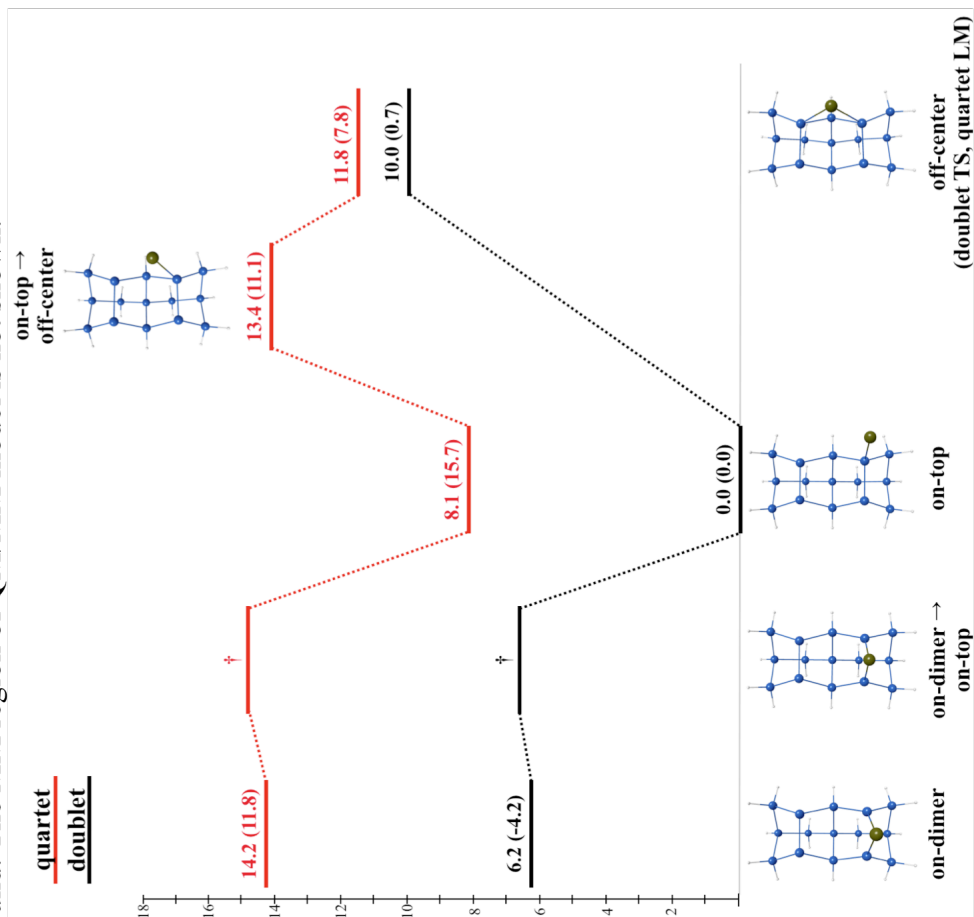


Figure 6: Two-dimer QM cluster used by QM and QM/MM models. The labels in red refer to the positions of Ga adatoms in the Ga_2 dimer structures.

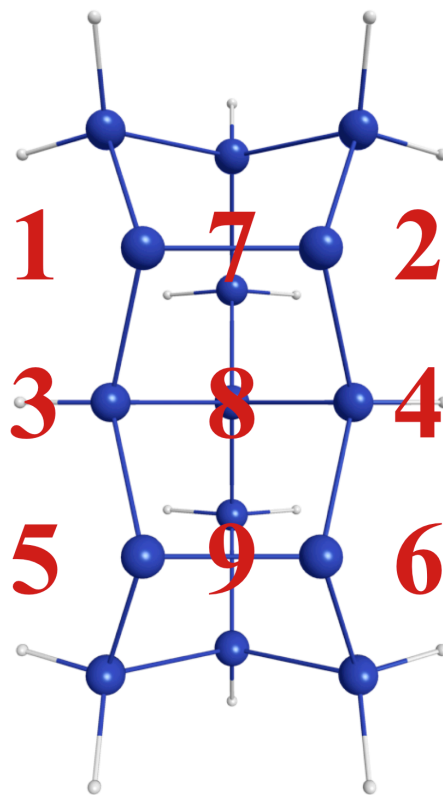


Figure 7: Singlet and triplet potential energy surfaces that depict the diffusion of two separated Ga adatoms on the $\text{Si}_{15}\text{H}_{16}$ QM cluster. MRMP2//CASSCF energies are in parentheses. All energies are relative to the singlet **5-6** structure. Energies are in kcal/mol.

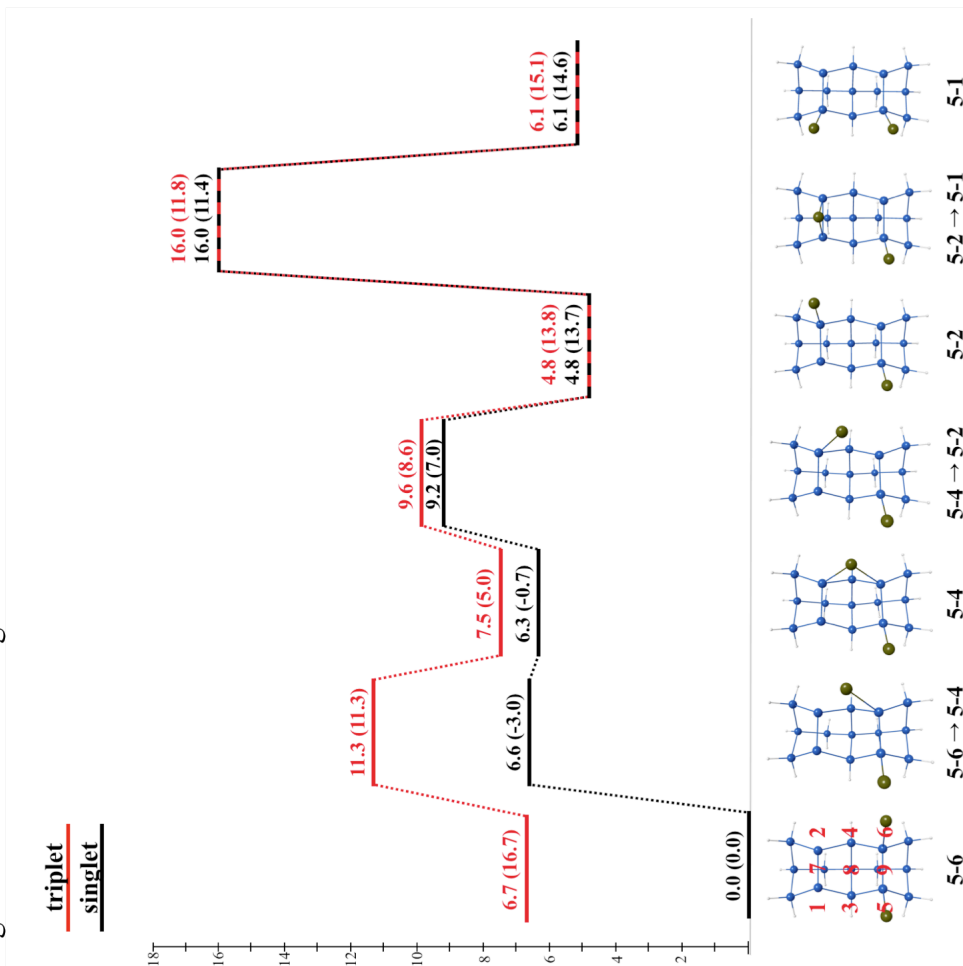


Figure 8: Singlet and triplet potential energy surfaces for the diffusion of two separated Ga adatoms on the $\text{Si}_{199}\text{H}_{92}$ QM/MM cluster. MRMP2//CASSCF energies are in parentheses. All energies are relative to the singlet **5-6** structure. Energies are in kcal/mol. Note: MM region of QM/MM model is not shown.

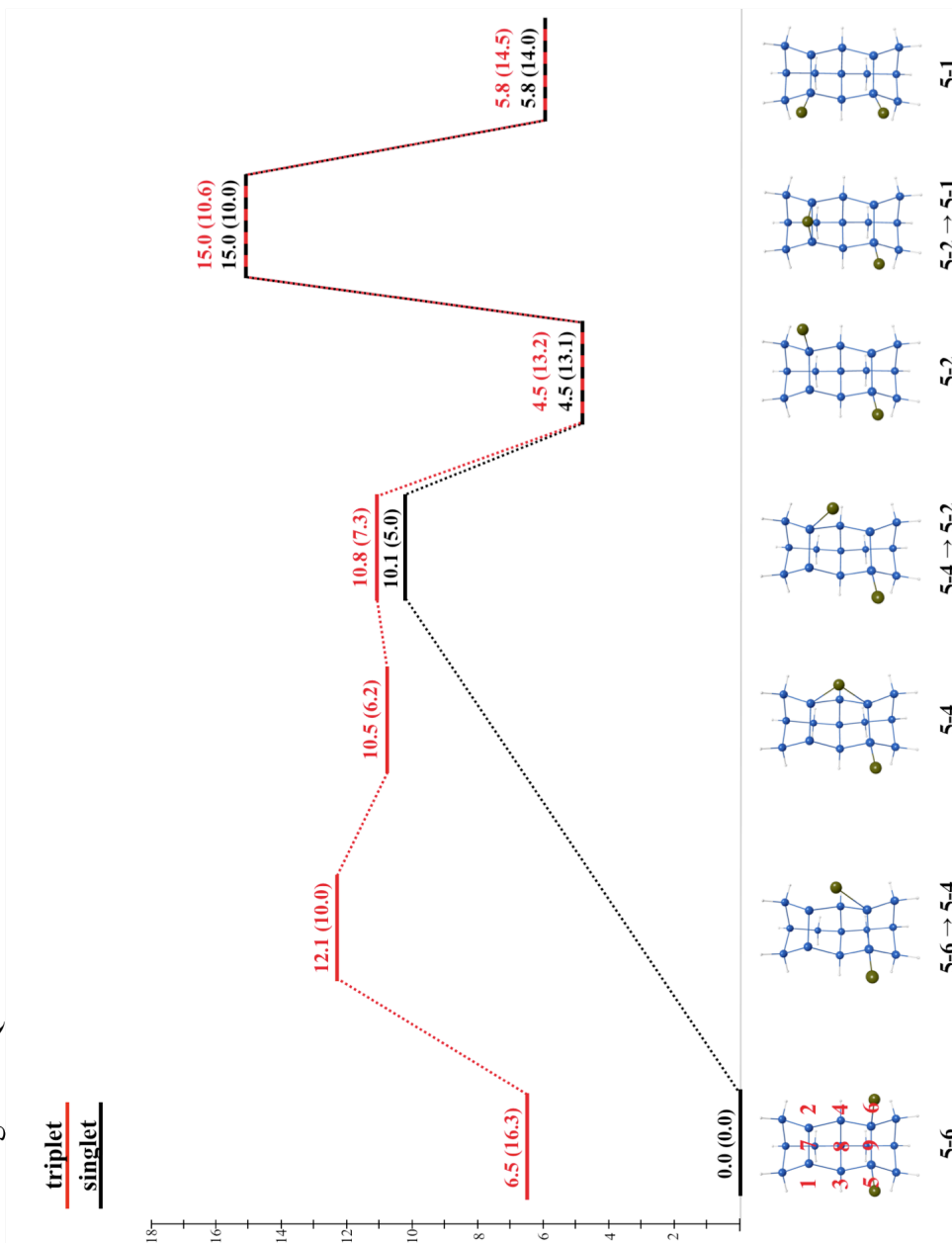


Figure 9: Singlet and triplet potential energy surfaces for the formation of Ga₂ dimer from two separated Ga adatoms on the Si₁₅H₁₆ QM cluster. MRMP2//CASSCF energies are in parentheses. All energies are relative to the singlet **5-6** structure. Energies are in kcal/mol.

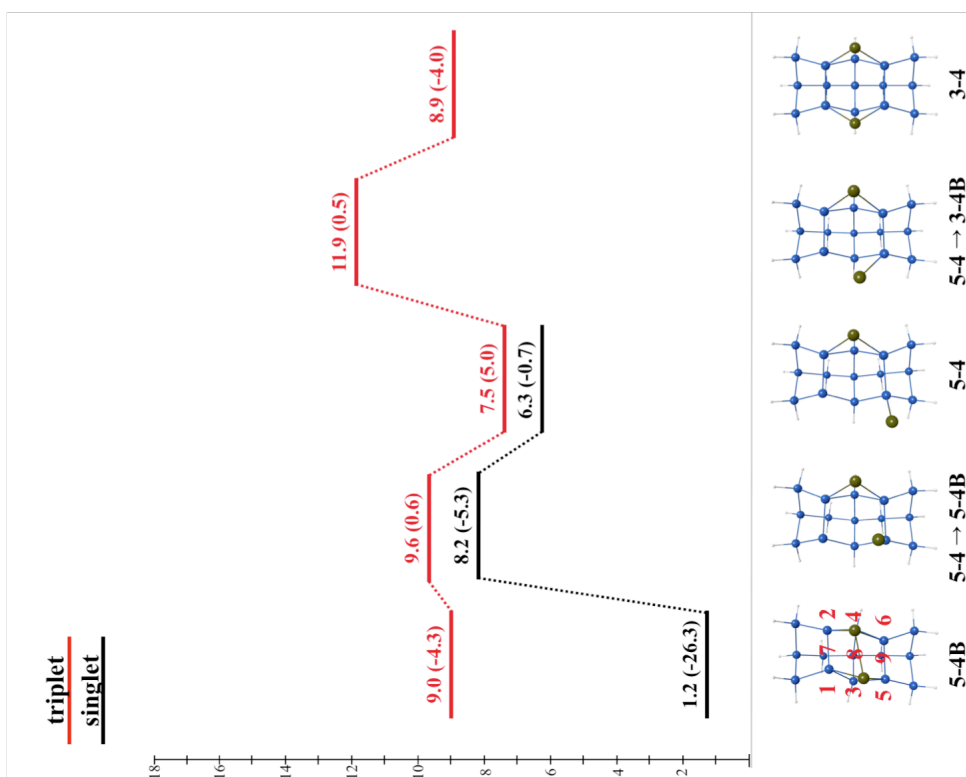


Figure 10: Singlet and triplet potential energy surfaces for the formation of Ga₂ dimer from two separated Ga adatoms on the QM/MM Si₁₉₉H₉₂ cluster. MRMP2//CASSCF energies are in parentheses. All energies are relative to the singlet **5-6** structure. Energies are in kcal/mol. Note: MM region of QM/MM model is not shown.

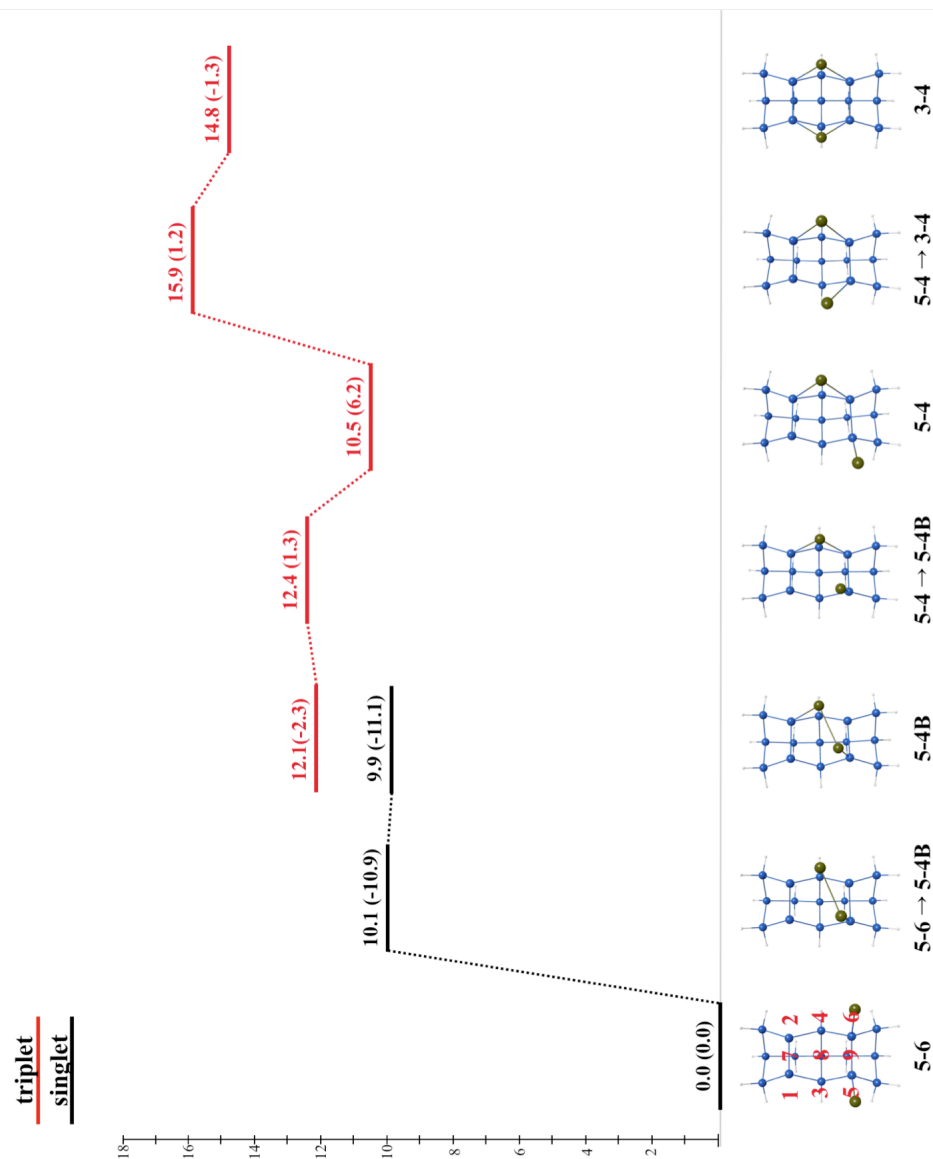


Figure 11: Singlet and triplet potential energy surfaces for the rotation of Ga₂ dimer on the QM Si₁₅H₁₆ cluster. MRMP2//CASSCF energies are in parentheses. All energies are relative to the singlet **5-6** structure. Energies are in kcal/mol.

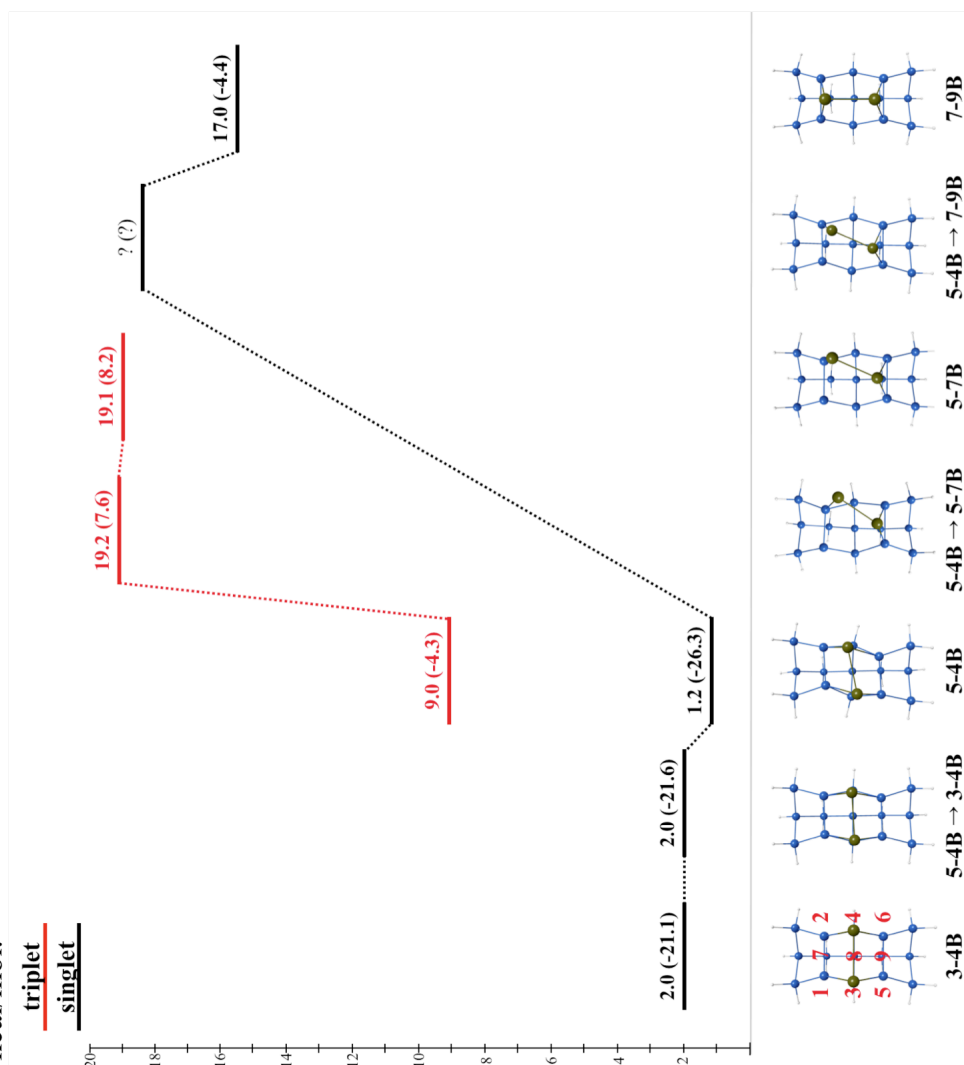


Figure 12: Singlet and triplet potential energy surfaces for the rotation of Ga₂ dimer on the QM/MM Si₁₉₉H₉₂ cluster. MRMP2//CASSCF energies are in parentheses. All energies are relative to the singlet **5-6** structure. Energies are in kcal/mol. Note: MM region of QM/MM model is not shown.

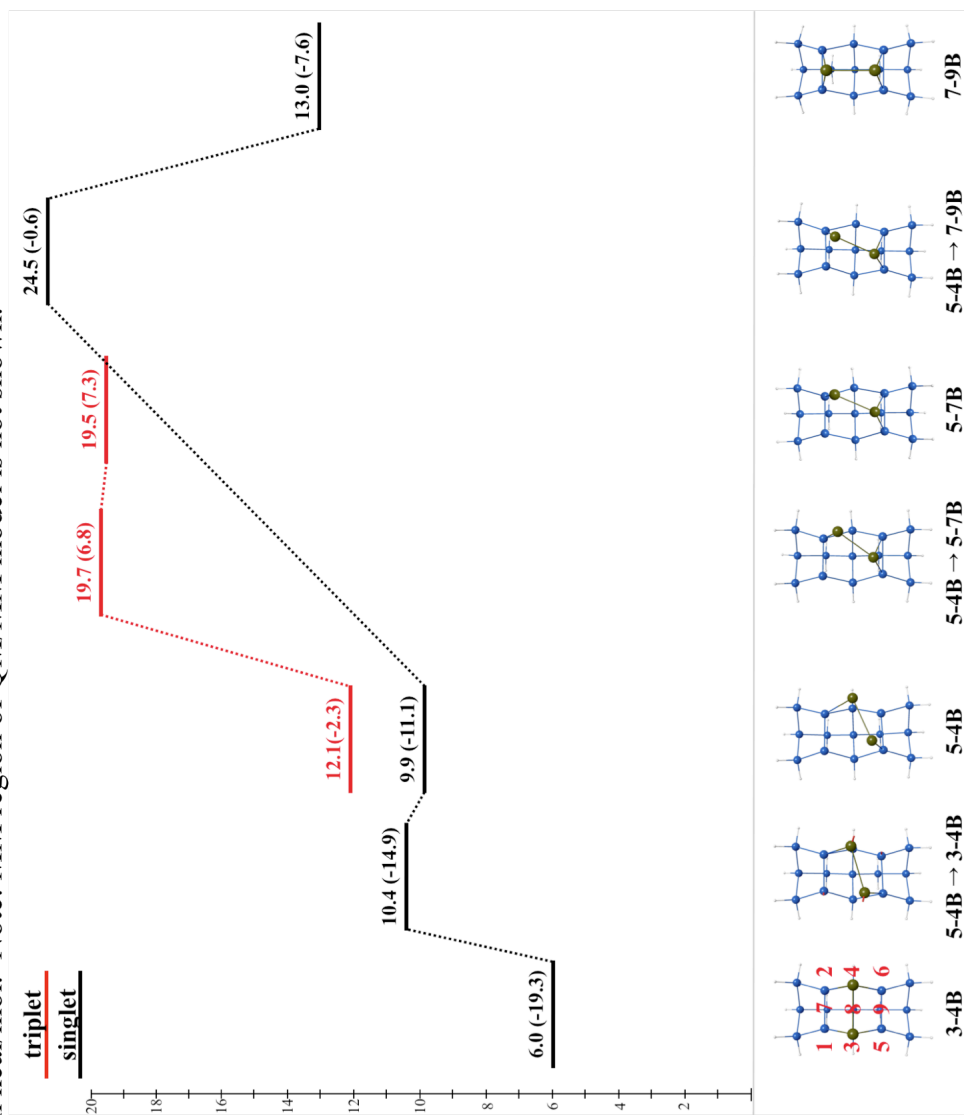


Figure 13: Geometries of optimized QM and QM/MM **5-4B** structures.
Note: MM region of QM/MM model is not shown.

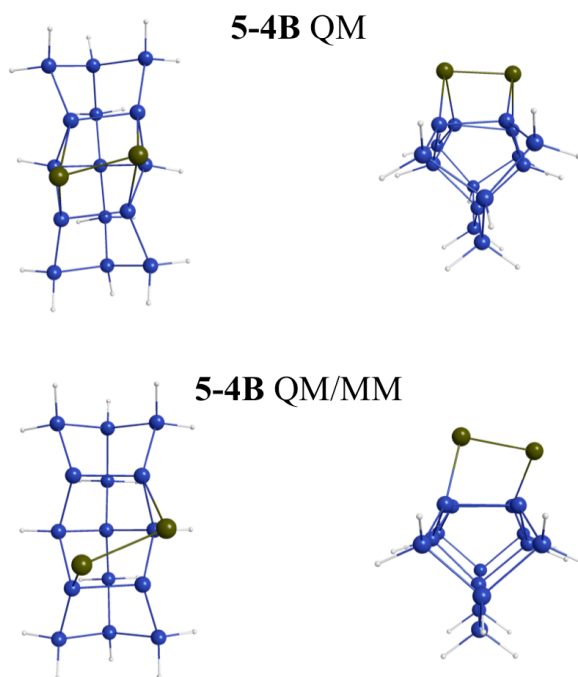


Table 1: NOON values for all structures that involve Ga adatom on QM ($\text{Si}_{15}\text{H}_{16}$) and QM/MM ($\text{Si}_{199}\text{H}_{92}$) clusters. The NOON values reported correspond to natural orbitals that exhibit the largest amount of multi-reference behavior (critical NOON range: 1.90-0.10).

Structure	2S + 1	QM NOON Values			PT correction (kcal/mol)			QM/MM NOON Values			PT correction (kcal/mol)		
on-dimer	2	1.73	1.01	0.27	-	-10.4	-	1.73	1.01	0.27	-	-10.4	-
on-top	2	1.90	1.73	1.00	0.27	0.0	-	1.90	1.72	1.00	0.28	0.0	0.0
on-top→pseudo-off-center	2	1.55	1.00	0.44	-	-9.1	-	N/A	N/A	N/A	N/A	N/A	N/A
pseudo-off-center	2	1.47	1.00	0.53	-	-8.2	-	N/A	N/A	N/A	N/A	N/A	N/A
off-center	2	1.35	1.00	0.65	-	-7.1	-	1.39	1.00	0.61	-	-9.3	-
pseudo-off-center→threefold	2	1.45	1.00	0.56	-	-10.5	-	N/A	N/A	N/A	N/A	N/A	N/A
threefold	2	1.90	1.00	0.12	-	-15.3	-	N/A	N/A	N/A	N/A	N/A	N/A
threefold→on-top	2	1.62	1.00	0.39	-	-16.6	-	N/A	N/A	N/A	N/A	N/A	N/A
on-dimer	4	1.01	1.00	1.00	-	-2.4	-	1.01	1.00	1.00	-	-2.4	-
on-top	4	1.90	1.00	1.00	1.00	7.6	-	1.90	1.00	1.00	1.00	7.6	-
on-top→off-center	4	1.90	1.00	1.00	1.00	-0.5	-	1.00	1.00	1.00	-	-2.3	-
off-center	4	1.00	1.00	1.00	-	-2.7	-	1.00	1.00	1.00	-	-4.0	-

Table 2: NOON values for Ga₂ structures on QM (Si₁₅H₁₆) and QM/MM (Si₁₉₉H₉₂) clusters. The NOON values reported correspond to natural orbitals that exhibit the largest amount of multi-reference behavior (critical NOON range: 1.90-0.10).

Structure	2S+1	QM NOON Values				PT correction (kcal/mol)				QM/MM NOON Values				PT correction (kcal/mol)				
		1.90	1.90	1.68	0.33	0.0	-9.6	-7.0	-2.2	8.9	-4.6	8.5	-13.5	1.90	1.90	1.67	0.33	0.0
5-6	1	1.90	1.90	1.54	0.45	-	-	-	-	-	-	-	-	N/A	N/A	N/A	N/A	N/A
5-6→5-4	1	1.90	1.90	1.37	0.63	-	-	-	-	-	-	-	-	N/A	N/A	N/A	N/A	N/A
5-4	1	1.90	1.90	1.90	1.18	0.82	0.96	0.90	0.90	0.90	0.90	0.90	0.90	1.89	1.23	0.77	-	-5.1
5-4→5-2	1	1.90	1.90	1.90	1.04	0.96	0.90	0.90	0.90	0.90	0.90	0.90	0.90	1.90	1.90	1.04	0.96	8.6
5-2	1	1.90	1.90	1.10	0.91	-	-	-	-	-	-	-	-	1.90	1.11	0.89	-	-5.0
5-2→5-1	1	1.90	1.90	1.90	1.11	0.90	0.90	0.90	0.90	0.90	0.90	0.90	0.90	1.90	1.11	0.89	-	8.2
5-1	1	1.90	1.90	1.41	0.59	-	-	-	-	-	-	-	-	N/A	N/A	N/A	N/A	N/A
5-4→5-4B	1	1.90	1.90	1.41	0.59	-	-	-	-	-	-	-	-	N/A	N/A	N/A	N/A	N/A
3-4B	1	1.90	0.12	-	-	-	-	-	-	-	-	-	-	1.90	0.12	-	-	-25.3
5-4B→3-4B	1	1.89	0.12	-	-	-	-	-	-	-	-	-	-	1.90	1.67	0.33	-	-25.3
5-6→5-4B	1	N/A	N/A	N/A	N/A	N/A	N/A	N/A	N/A	N/A	N/A	N/A	N/A	1.90	1.55	0.45	-	-21.0
5-4B	1	1.87	0.15	-	-	-	-	-	-	-	-	-	-	1.90	1.50	0.50	-	-21.0
5-4B→7-9B	1	?	?	?	?	?	?	?	?	?	?	?	?	1.89	1.89	0.15	-	-25.1
7-9B	1	0.11	-	-	-	-	-	-	-	-	-	-	-	0.10	-	-	-	-20.6
5-6	3	1.90	1.90	1.90	1.00	1.00	1.00	1.00	1.00	1.00	1.00	1.00	1.00	1.90	1.90	1.00	1.00	9.8
5-6→5-4	3	1.90	1.90	1.90	1.00	1.00	1.00	1.00	1.00	1.00	1.00	1.00	1.00	1.91	1.90	1.00	1.00	-2.1
5-4	3	1.90	1.00	1.00	1.00	-	-	-	-2.5	-	-	-	-	1.90	1.00	1.00	-	-4.3
5-4→5-2	3	1.90	1.90	1.90	1.00	0.98	1.00	1.00	-1.0	9.0	-4.2	9.0	9.0	1.90	1.00	1.00	-	-3.5
5-2	3	1.90	1.90	1.90	1.00	1.00	1.00	1.00	9.0	9.0	-4.2	9.0	9.0	1.90	1.90	1.00	1.00	8.7
5-2→5-1	3	1.90	1.00	1.00	1.00	-	-	-	-4.2	-	-	-	-	1.90	1.00	1.00	-	-4.4
5-1	3	1.90	1.90	1.90	1.00	1.00	1.00	1.00	9.0	9.0	-11.4	9.0	9.0	1.90	1.90	1.00	1.00	8.7
5-4→3-4	3	1.90	1.00	1.00	1.00	-	-	-	-11.4	-	-	-	-	1.00	1.00	-	-	-14.7
5-4B	3	1.90	1.00	1.00	1.00	-	-	-	-13.3	-	-	-	-	1.90	1.00	1.00	-	-14.4
3-4	3	1.00	1.00	-	-	-	-	-	-12.9	-	-	-	-	1.00	1.00	-	-	-16.1
5-4→5-4B	3	1.90	1.00	1.00	1.00	-	-	-	-9.0	-	-	-	-	1.90	1.00	1.00	-	-11.1
5-4B→5-7B	3	1.00	1.00	-	-	-	-	-	-11.6	-	-	-	-	1.00	1.00	-	-	-12.9
5-7B	3	1.00	1.00	-	-	-	-	-	-10.9	-	-	-	-	1.00	1.00	-	-	-12.2

Table 3: Relative energy difference between structures common to Ga QM and QM/MM .

Structure	2S+1	E[QM] ^a – E[QM/MM] ^b (kcal/mol)	
		CASSCF	MRMP2//CASSCF
on-dimer	1	0.7	0.7
on-top	1	0.0	0.0
off-center	1	-3.0	-0.8
on-dimer	3	0.8	0.8
on-top	3	0.2	0.2
on-top→off-	3	-0.9	0.9
off-center	3	-3.4	-2.1
MAE		1.3	0.8

^aenergy relative to singlet QM **on-top** structure^benergy relative to singlet QM/MM **on-top** structure

Table 4: Relative energy difference between structures common to Ga₂ QM and QM/MM models that describe.

Structure	2S+1	E[QM] ^a – E[QM/MM] ^b (kcal/mol)	
		CASSCF	MRMP2//CASSCF
5-6	1	0.0	0.0
5-4→5-2	1	-0.9	2.0
5-2	1	0.3	0.6
5-2→5-1	1	1.0	1.4
5-1	1	0.3	0.6
3-4B	1	-4.0	-1.8
5-4B→3-4B	1	-8.4	-6.7
5-4B	1	-8.7	-15.2
5-4B→7-9B	1	?	?
7-9B	1	4.0	3.2
5-6	3	0.2	0.4
5-6→5-4	3	-0.8	1.3
5-4	3	-2.5	-1.2
5-4→5-2	3	-1.2	1.3
5-2	3	0.3	0.5
5-2→5-1	3	1.0	1.2
5-1	3	0.3	0.5
5-4→3-4B	3	-4.0	-0.7
5-4B	3	-4.6	7.3
3-4	3	-5.9	-2.7
5-4→5-4B	3	-2.8	-0.7
5-4B→5-7B	3	-0.5	0.8
5-7B	3	-0.4	0.9
MAE		2.3	2.3

^aenergy relative to QM singlet **5-6** structure^benergy relative to QM/MM singlet **5-6** structure

CHAPTER 5. CAN KOHN-SHAM ORBITALS BE USED TO INTERPRET ELECTRONIC SPECTRA?

Luke Roskop, Federico Zahariev, Kenneth Hanson, and Mark S. Gordon

The validity of the use of orbital interpretations in excited state chemistry is discussed. In particular, a set of criteria is suggested to validate the use of Kohn-Sham (KS) orbitals to interpret electronic excited states and photochemistry. Time dependent density functional theory (TDDFT) and the Tamm-Dancoff approximation to TDDFT are the primary tools that can be employed to assess the efficacy of using KS orbitals to interpret electronic excited states. The limitations on orbital interpretations is considered, together with examples that illustrate both a successful and unsuccessful application of such interpretations.

1. Introduction

Molecular orbitals (MOs) are often used to interpret chemical phenomena.^{1,2} Strictly speaking, this approach, while time-honored and frequently useful, is only approximate, because the total energy of a system is not the sum of the orbital energies, and because MOs are not physical observables. Indeed, MOs arise from invoking the independent particle (orbital) model when the many-body problem is encountered in attempting to solve the many-electron time-independent Schrödinger equation. That is, the exact wavefunction is approximated as a determinant (more generally, as a linear combination of determinants) of one-electron functions (MOs):

$$\Psi(x_1, x_2, \dots, x_N) \approx \frac{1}{\sqrt{N!}} |\varphi(x_1), \varphi(x_2), \dots, \varphi(x_N)| \quad (1)$$

One can generate a set of orbitals from single reference electronic structure methods

like Hartree-Fock (HF)³ and density functional theory (DFT)⁴,...). Whether these orbitals can provide any substantial insight into electronic spectroscopy or photochemical behavior is not apparent from the orbitals alone. Comparisons with experiment are useful, but not generally sufficient, because one can obtain apparent agreement with experiment for specific cases for the wrong reason; that is, even though the underlying physics may be incorrect. It would therefore be beneficial to have a sound theoretical analysis of the validity of simple orbital interpretations that is easily applied to electronic spectroscopy and photochemistry. This paper proposes a set of criteria that, when satisfied, provides credence for orbital interpretations within the very popular DFT approximation.

2. Excited state methods

Many methods are routinely used to predict and interpret electronic absorption spectra of chemical systems. A brief review of a few of these methods is presented here.

2A. MO energy differences

Orbital based discussions of electronic excited states often focus on excitations from the highest occupied molecular orbital (HOMO) to the lowest unoccupied molecular orbital (LUMO). Of the three most commonly used methods to determine MOs, extended Hückel theory (EHT),⁵ Hartree-Fock (HF) theory, and DFT, only in EHT can the total energy be correctly written as a sum of the orbital energies. Because HF and DFT include electron repulsions, a sum of all orbital energies double-counts these repulsions.⁶ So, only in EHT can excitation energies be expressed as LUMO-HOMO energy differences. Although HF MO energies and DFT Kohn-Sham (KS) orbital energies cannot by themselves be used to make quantitative predictions of excitation energies, they can be useful for rationalizing observed phenomena, as HF MOs (and KS orbitals) capture characteristic attributes of the

wavefunction. These attributes, for example, may be described in terms of orbital nodes, orbital phases, and orbital symmetry. As demonstrated by Woodward and Hoffman,² MOs can be routinely applied to understand chemical reactivity.

2B. Configuration interaction

Configuration interaction (CI) constructs excited state wavefunctions, usually from a set of HF orbitals, by taking a linear combination of one-electron replacements from HF occupied orbitals into virtual orbitals (CI singles = CIS) plus double replacements (CISD), etc. So, the CI wavefunction is a linear combination of determinants:

$$\Phi_{\text{CI}} = C_{\text{HF}} \Psi_{\text{HF}} + \sum_{\text{S}} C_{\text{S}} \Psi_{\text{S}} + \sum_{\text{D}} C_{\text{D}} \Psi_{\text{D}} + \dots \quad (2)$$

If all possible replacements are included in Eq. (2), the resulting wavefunction is called Full CI (FCI) and is the exact wavefunction for a given atomic basis set. Generally, FCI is not computationally tractable, so one truncates the expansion in Eq. (2). The simplest CI level of theory is CIS. The CIS expansion coefficients (C_{S} in Eq. (2)) quantify the contribution of an occupied-unoccupied MO pair for a particular excited state wavefunction. For example, if there is a dominant CIS expansion coefficient ($C_{\text{S}} \sim |1.0|$) that corresponds (for example) to a HOMO→LUMO excitation, then the frontier MO pair would be useful for interpreting electronic excited states. Of course, since CIS only includes single excitations, this method cannot describe excited states that have double excitation character. The latter require at least double excitations.

2C. Time dependent HF, time dependent DFT and the Tamm-Dancoff Approximation

Time dependent HF (TDHF) is used to directly compute excitation energies from the HF single-determinant wavefunction, by solving the linear response equations summarized in

Eq. (3), below. In Eq. (3), the left-most term is the response matrix, ω represents the excitation energies, and \mathbf{X} (\mathbf{Y}) is a vector that denotes excitation (de-excitation) coefficients. The elements of the singlet (triplet) \mathbf{A} (\mathbf{B}) matrix are given in Eq. (4)-(5) (Eq. (6)-(7)). The leading term of the diagonal of matrix \mathbf{A} (Eq. 4) is an orbital energy difference between occupied MO i and unoccupied MO a . The remaining terms in \mathbf{A} and \mathbf{B} are two-electron integrals over occupied MOs i, j and unoccupied MOs a, b . The excitation and de-excitation coefficients can be interpreted as the weight of a particular excitation ($i \rightarrow a$) and de-excitation ($a \rightarrow i$), respectively, in the computed excitation energy.

$$\begin{bmatrix} \mathbf{A} & \mathbf{B} \\ \mathbf{B} & \mathbf{A} \end{bmatrix} \begin{bmatrix} \mathbf{X} \\ \mathbf{Y} \end{bmatrix} = \omega \begin{bmatrix} 1 & 0 \\ 0 & -1 \end{bmatrix} \begin{bmatrix} \mathbf{X} \\ \mathbf{Y} \end{bmatrix} \quad (3)$$

$$\text{Singlet} \begin{cases} A_{ia,jb}^{\text{TDHF}} = \delta_{ij} \delta_{ab} (\epsilon_a - \epsilon_i) + 2(ia|bj) + (ib|aj) \\ B_{ia,jb}^{\text{TDHF}} = 2(ia|bj) + (ib|aj) \end{cases} \quad (4)$$

$$\quad \quad \quad (5)$$

$$\text{Triplet} \begin{cases} A_{ia,jb}^{\text{TDHF}} = \delta_{ij} \delta_{ab} (\epsilon_a - \epsilon_i) + (ib|aj) \\ B_{ia,jb}^{\text{TDHF}} = (ib|aj) \end{cases} \quad (6)$$

$$(7)$$

Time dependent DFT (TDDFT) also computes excitation energies using Eq. (3).

Unlike TDHF, the TDDFT equations include an exchange-correlation term (f_{xc}^σ) in \mathbf{A} and \mathbf{B} (Eq. (8)-(11)). The superscript σ on f_{xc}^σ is used to indicate whether the exchange-correlation functional was derived for a singlet (S) or triplet (T) state. The weighting factor c_{DFT} ($c_{\text{HF}} = 1 - c_{\text{DFT}}$) is a DFT on/off switch for the matrix elements in \mathbf{A} and \mathbf{B} . For example, if $c_{\text{DFT}} = 0$ ($c_{\text{HF}} = 1$) Eqs. (8)-(11) reduce to TDHF (Eqs. (4)-(7)). If $c_{\text{DFT}} = 1$ ($c_{\text{HF}} = 0$), Eqs. (8)-(11) are appropriate for a generalized gradient approximation (GGA) DFT. If both c_{DFT} and c_{HF} are nonzero, then Eqs. (8)-(11) apply to hybrid functionals.

$$\text{Singlet} \begin{cases} A_{ia,jb}^{\text{TDDFT}} = \delta_{ij} \delta_{ab} (\epsilon_a - \epsilon_i) + 2(ia|jb) + c_{\text{HF}}(ij|ab) + c_{\text{DFT}}(ia | f_{\text{XC}}^S | jb) & (8) \\ B_{ia,jb}^{\text{TDDFT}} = 2(ia|bj) + c_{\text{HF}}(ib|aj) + c_{\text{DFT}}(ia | f_{\text{XC}}^S | bj) & (9) \end{cases}$$

$$\text{Triplet} \begin{cases} A_{ia,jb}^{\text{TDDFT}} = \delta_{ij} \delta_{ab} (\epsilon_a - \epsilon_i) + c_{\text{HF}}(ij|ab) + c_{\text{DFT}}(ia | f_{\text{XC}}^T | jb) & (10) \\ B_{ia,jb}^{\text{TDDFT}} = c_{\text{HF}}(ib|aj) + c_{\text{DFT}}(ia | f_{\text{XC}}^T | bj) & (11) \end{cases}$$

One simplification that can be applied to both the TDHF and TDDFT linear response equations (Eq. 3) is the Tamm-Dancoff approximation (TDA).^{7,8} The TDA reduces the complexity of Eq. (3) through neglect of the **B** matrices, which reduces Eq. (3) to Eq. (12). The application of TDA to the TDHF method (TDA-TDHF) leads to the CIS method. Analogously, the TDA-TDDFT method can be thought of as the DFT equivalent to the CIS method.

$$\mathbf{AX} = \omega \mathbf{X} \quad (12)$$

3. Kohn-Sham orbital interpretations

Interpretations of chemical behavior based on KS orbitals must be applied only to obtain qualitative guidance, such as how the stabilization or destabilization of the HOMO or LUMO might affect the absorption energy. If one wishes to understand electronic spectroscopy or photochemical behavior using KS orbitals, then the conditions described in the following paragraphs should be satisfied.

Solutions to the linear response TDDFT equations contain coefficients that describe both excitations and de-excitations. The coefficient $X_{i \rightarrow a}$ (see Eq. (3)) refers to an electronic excitation from an occupied orbital (i) to a virtual orbital (a), and $Y_{a \rightarrow i}$ is the complementary de-excitation coefficient. The TDDFT normalization condition (Eq. (13)) involves both $X_{i \rightarrow a}$ and $Y_{a \rightarrow i}$, where the summation runs over all occupied orbitals (i) and virtual orbitals (a). This

coupling between $X_{i \rightarrow a}$ and $Y_{a \rightarrow i}$ complicates the TDDFT normalization condition. Thus, the TDDFT coefficients cannot definitively indicate the importance of a KS orbital pair in a particular excited state transition.

$$1 = \sum_i^{\text{occ}} \sum_a^{\text{virt}} \left((X_{i \rightarrow a})^2 - (Y_{a \rightarrow i})^2 \right) \quad (13)$$

On the other hand, the TDA-TDDFT approximation may be simply interpreted in terms of single excitations from occupied to virtual KS orbitals, in analogy with CIS. Therefore, the TDA-TDDFT coefficients can clearly identify the probability that a KS orbital pair contributes to a particular excited state transition. The coefficient $X_{i \rightarrow a}$ gives the importance of the particular excitation $i \rightarrow a$ to the excited state wavefunction. For the TDA approximation to TDDFT, TDA-TDDFT, to be reliable, *the TDA-TDDFT properties must be in good agreement with the full TDDFT method* (criterion #1). If this is the case, simple orbital interpretations may be viable. *If criterion #1 is satisfied and if there is a dominant TDA-TDDFT coefficient (e.g., $X_{i \rightarrow a} > |0.9|$), then the excited state may be interpreted in terms of the corresponding excitation $i \rightarrow a$* (criterion # 2). The final criterion (criterion #3) is the simplest: *The spectrum predicted by TDDFT and TDA-TDDFT must be in good agreement with experiment*. Then, the shape, symmetry, and nodal planes of the KS orbitals can be useful features to aid in the understanding of spectroscopy and photochemistry.

4. Applications

The criteria presented above to validate a KS orbital interpretation of photochemical behavior are now applied to several systems to illustrate situations in which it is and is not appropriate to employ a KS orbital analysis. These systems include five 1,3-bis(2-

pyridylimino)isoindolate platinum chloride derivatives and three magnesium-centered porphyrin derivatives. All structures were optimized by DFT using the hybrid B3LYP functional.⁹ All stationary points were confirmed as minima on the ground state potential energy surface by diagonalizing the Hessian (matrix of energy second derivatives). Both TDDFT and TDA-TDDFT excitation energies were calculated using the B3LYP functional. All properties are computed with the General Atomic Molecular Electronic Structure System (GAMESS).¹⁰

4A. 1,3-bis(2-pyridylimino)isoindolate platinum chloride derivatives

Five previously reported platinum(II) complexes (Figure 1)¹¹ of the form $(N^{\wedge}N^{\wedge}N)PtCl$ are reexamined, where $N^{\wedge}N^{\wedge}N$ represents the tridentate monoanionic ligands 2,5-bis (2-pyridylimino)3,4-diethylpyrrolate (**1A**), 1,3-bis(2-pyridylimino)isoindolate (**1B**), 1,3-bis(2-pyridylimino)benz(f)isoindolate(**1C**), 1,3-bis(2-pyridylimino)benz(e)isoindolate(**1D**) and 1,3-bis(1-isoquinolylimino) isoindolate (**1E**). Platinum and chlorine are described using the MCPtzp and MCPdzp small-core model core potentials, respectively,¹² whereas all other atoms are treated with the cc-pVDZ all-electron basis set.¹³ The effects of solvent (CH_2Cl_2) on the excitation energies are considered with the conductor-like polarizable continuum model (CPCM).¹⁴

Table 1 displays the lowest TDDFT excitation energies for both gas and solution phase. Relative to **1A**, TDDFT confirms that **1B** and **1C** exhibit a blue-shift in absorption with each successive benzannulation at the pyrrole position. Although complexes **1D** and **1E** are also benzannulated versions of **1B**, they display a red-shift in absorption relative to **1B**, as opposed to the blue-shift observed for **1C**. This computed absorption trend agrees with the experimental results.

The TDA-TDDFT excitation energies qualitatively agree with the trend established by TDDFT. The squares of the TDA-TDDFT excitation coefficients indicate the HOMO→LUMO transition dominates the lowest energy excitations (85-90%) among all structures. The qualitative agreement between TDA-TDDFT and TDDFT combined with the large HOMO→LUMO excitation coefficient validates a KS orbital interpretation of the observed trend. Since TDA-TDDFT indicates that the lowest energy excitation is dominated by the HOMO→LUMO transition, any orbital interpretation of the observed trends must consider these two frontier orbitals.

The KS HOMO and LUMO energies for the ground state of each system are also listed in Table 1. It is apparent the KS HOMO energies remain relatively constant while the LUMO energies increase (decrease) from **1A** to **1B** to **1C** (**1B** to **1D** to **1E**). The theoretical results suggest that this uncharacteristic blue-shift in absorption from **1A** to **1B** to **1C** is due to destabilization of the LUMO with each successive expansion of the π -system off the pyrrolate moieties. This destabilization of the LUMO can be understood through a simple KS orbital interpretation, as discussed in the next paragraph.

One can visualize the formation of the frontier molecular orbitals of **1B** by combining the valence orbitals of **1A** with those of 1,3-butadiene as illustrated in Figure 2. The HOMO makes virtually no contribution at the site of benzannulation of **1A** by 1,3-butadiene, thus no orbital mixing is observed, and the HOMO energy remains essentially unchanged in **1B**. The LUMO of **1A** is localized primarily on the π -system of the ligand. If one ignores the out of plane distortion of the chloride atom, **1A** can be idealized as having C_{2v} symmetry. In this point group, the LUMO of **1A** can be considered to have b_2 symmetry. *Cis*-1,3-butadiene also

has C_{2v} symmetry, with the HOMO and LUMO belonging to the irreducible representations b_2 and a_2 , respectively. The a_2 symmetry of the LUMO of 1,3-butadiene cannot mix with the b_2 LUMO of **1A**. However, both the HOMO of 1,3-butadiene and the LUMO of **1A** have the same b_2 symmetry, so they can combine to create an occupied bonding MO (not shown) and an unoccupied antibonding orbital (LUMO of **1B**) with the addition of a new nodal plane at the site of attachment. The favorable orbital symmetry enables the HOMO of 1,3-butadiene to act as an effective electron donating group to the LUMO of **1A**. The net consequence of these interactions is an unaltered HOMO and a destabilized LUMO that results in the observed blue-shifted absorption upon benzannulation of **1A**. Likewise, a similar combination of the frontier orbitals of **1B** and 1,3-butadiene leads to an unaltered HOMO and a destabilized LUMO as seen in **1C**. Even when the geometry deviates somewhat from the idealized C_{2v} symmetry, the nodal behavior of the orbitals at the site of butadiene addition can be used to make reasonable qualitative arguments.

The symmetry of interacting orbitals can also be used to interpret the effects of benzannulation at other positions of **1B**. When **1B** is benzannulated at either the 5,6-positions or the 3,4-positions (to form **1D** and **1E**, respectively) the LUMO is stabilized, illustrated in Figure 3. The orbitals of **1B** can be characterized by the presence or absence of a bisecting nodal plane at the site of benzannulation. The absence of a perpendicular bisecting nodal plane at either of the relevant positions of the LUMO of **1B** favors a cooperative interaction with the LUMO of 1,3-butadiene that leads to a bonding/antibonding pair of MOs. The end result is a stabilized LUMO in both **1D** and **1E**.

For the five platinum(II) complexes, a KS orbital interpretation is valid, since the three criteria discussed above are satisfied: **1**) the absorption trends established by TDA-

TDDFT agree with TDDFT and experiment, **2)** the TDA-TDDFT indicates the dominant transition is HOMO→LUMO, and **3)** the orbital interpretation supports the observed behavior.

4B. Magnesium porphyrin derivatives

Three Magnesium porphyrin derivatives (Figure 4) are examined to illustrate a system for which an orbital interpretation of photochemical behavior is not appropriate. Complexes **4B** and **4C** are substituted versions of **4A**. All DFT ground state optimizations and TDDFT excited state computations used the 6-31G (d,p) basis set.¹⁵

Table 2 displays TDDFT and TDA-TDDFT excitation energies for the lowest energy transition of **4A**, **4B**, and **4C**. TDA-TDDFT predicts a red-shift (relative to **4A**) in the absorption spectrum for structure **4B** and structure **4C**. The TDA-TDDFT absorption energy of **4C** (relative to **4A**) red-shifts by 36 nm while TDDFT indicates **4B** and **4C** have similar absorption energies.

The TDA-TDDFT coefficients listed in Table 2 demonstrate that the excited state transitions for **4A-4C** are much more complicated than a simple HOMO→LUMO transition. The coefficients for the HOMO-LUMO contribution to the excitation are on the order of 0.5, so the HOMO-LUMO excitation contributes only about half of the excitation energy. Thus, the trend of the lowest energy Mg-porphyrin excited state transitions for structures **4A-4C** cannot be interpreted with a simple orbital analysis.

5. Conclusions.

Three criteria were presented as guidelines to validate KS orbital interpretations in excited state chemistry:

- 1) The TDA-TDDFT properties, particularly the excitation energy, must be in good agreement with the full TDDFT method*
- 2) If criterion 1 is satisfied and if there is a dominant TDA-TDDFT coefficient (e.g., $X_{i \rightarrow a} > |0.9|$), then the excited state may be interpreted in terms of the corresponding excitation $i \rightarrow a$.*
- 3) The spectrum predicted by TDDFT and TDA-TDDFT must be in good agreement with experiment.*

Since KS orbitals are not physical observables, the use of KS orbitals in the interpretation of photochemical behavior must be carefully considered. Like CIS, TDA-TDDFT coefficients can clearly indicate which orbital pairs contribute to a particular excited state transition.

For the platinum(II) complexes, the TDA-TDDFT predictions of the lowest absorption energies were in agreement the TDDFT absorption frequencies (criterion #1). The lowest energy transitions for the series of platinum(II) complexes were shown to be dominated by a single excitation (HOMO \rightarrow LUMO) (criterion #2). Both the TDA-TDDFT and TDDFT calculated absorption energies of the platinum(II) complexes are in agreement with experimental measurements (criterion #3). Since all three criteria were satisfied for the platinum(II) complexes, a Kohn-Sham orbital interpretation of the absorption trend is valid and shown to successfully predict the trend in absorption energies. Conversely, a series of Mg-porphyrins was shown to have double excitation character. Thus, the series of Mg-porphyrin systems does not satisfy criterion #2 for an orbital interpretation of the absorption trends.

Acknowledgments

LR, FZ and MSG are grateful for the support of the Air Force Office of Scientific Research.

References

- ¹K. Fukui, T. Yonezawa, H. Shingu, J. Chem. Phys. **20**, 722 (1952). K. Fukui, *Angew. Chem. Int. Ed. Engl.* **21**, 801 (1982).
- ²R. B. Woodward, R. Hoffmann, JACS **87**, 395 (1965). R. Hoffmann, R. B. Woodward, JACS **87**, 2046 (1965). R. B. Woodward, R. Hoffmann, JACS **87**, 2511 (1965).
- ³D. R. Hartree, Proc. Camb. Phil. Soc. **25**, 89 (1928). F. Fock, Zs. f. Phys. **61**, 126 (1930). A. Szabo, N. S. Ostlund, “*Modern Quantum Chemistry*”. Mineola, New York: Dover Publishing (1996).
- ⁴P. Hohenberg, W. Kohn, Phys. Rev. **136**, B864 (1964). W. Kohn, L. J. Sham, J. Phys. Rev. **140**, A1133 (1965).
- ⁵R. Hoffmann, J. Chem. Phys. **39**, 1397 (1963).
- ⁶I. Levine, “*Quantum Chemistry*”, fifth edition, (Prentice Hall Inc. Upper Saddle River, New Jersey, 2000)
- ⁷I. Tamm, Journal of Physics-USSR **9**, 449 (1945). S. M. Dancoff S. M. Physical Review **78**, 382 (1950).
- ⁸A. Dreuw, M. Head-Gordon, Chem. Phys. Rev. **105**, 4009 (2005).
- ⁹A. D. Becke, Journal of Chemical Physics **98**, 5648 (1993). R. H. Hertwig, W. Koch, Chemical Physics Letters **268**, 345 (1997). P. J. Stephens, F. J. Devlin, C. F. Chabalowski, M. J. Frisch, The Journal of Physical Chemistry **98**, 11623 (1994).

- ¹⁰M. S. Gordon, M. W. Schmidt, "Theories and Applications of Computational Chemistry, the First Forty Years", C. E. Dykstra, G. Frenking, K. S. Kim, G. E. Scuseria, Elsevier, Amsterdam, 2005, pp 1167-1189. M. W. Schmidt, K. K. Baldridge, J. A. Boatz, S. T. Elbert, M. S. Gordon, J. H. Jensen, S. Koseki, N. Matsunaga, K. A. Nguyen, S. Su, T. L. Windus, M. Dupuis, J. A. Montgomery, *Journal of Computational Chemistry* **14**, 1347-1363 (1993).
- ¹¹K. Hanson, L. Roskop, P. I. Djurovich, F. Zahariev, M. S. Gordon, M. E. Thompson, *JACS* **132**, 16247 (2010).
- ¹²H. Mori, K. Ueno-Noto, Y. Osanai, T. Noro, T. Fujiwara, M. Klobukowski, E. Miyoshi, *Chem. Phys. Lett.* 2009, in press.
- ¹³T. H. Dunning Jr., *Journal of Chemical Physics* **90**, 1007 (1989).
- ¹⁴M. Cossi, V. Barone, *Journal of Chemical Physics* **115**, 4708 (2001).
- ¹⁵W. J. Hehre, R. Ditchfield, J. A. Pople, *J. Chem. Phys.* **56**, 2257 (1972). M. M. Francl, W. J. Petro, W. J. Hehre, J. S. Binkley, M. S. Gordon, D. J. DeFrees, J. A. Pople, *J. Chem. Phys.* **77**, 3654 (1982).

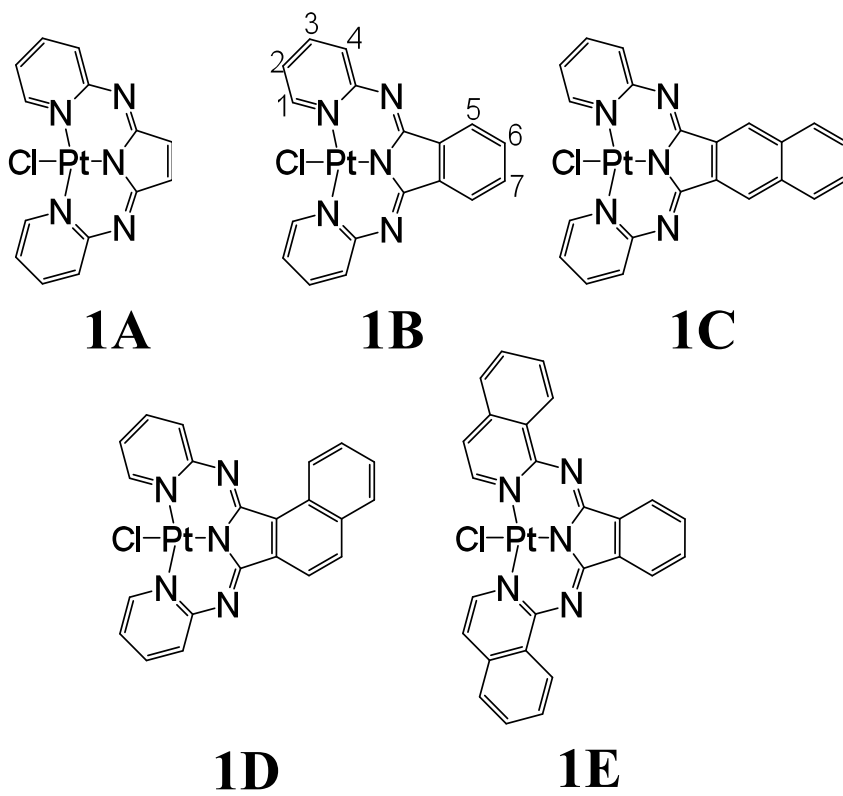
Figure 1: Series of substituted platinum complexes.

Figure 2: Qualitative orbital diagram of the valence orbitals for complexes **1A**, **1B**, and **1C**. The HOMO (bottom, solid) and LUMO (top, transparent) surfaces are displayed as viewed above the π -symmetric orbitals, with opposite phases above and below the plane of the molecule. All orbital energies are presented in eV.

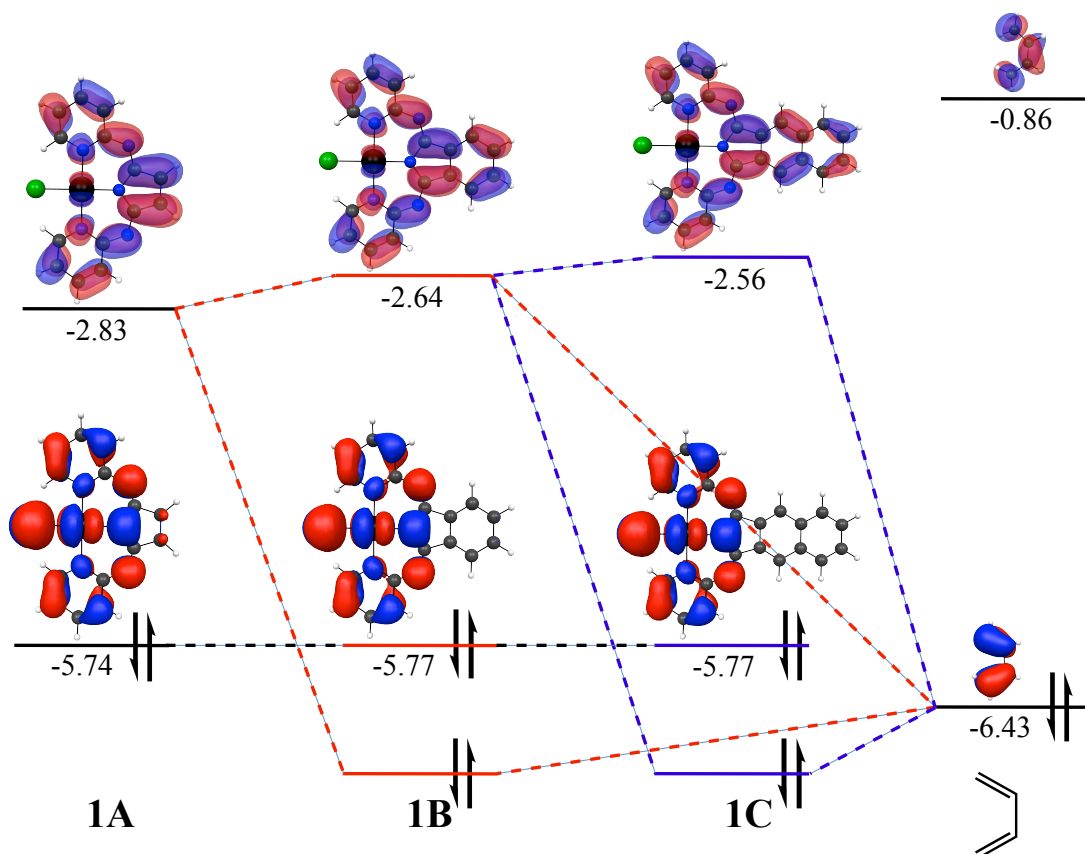


Figure 3: Qualitative orbital diagram of the valence orbitals for complexes **1B**, **1D**, and **1E**. The HOMO (bottom, solid) and LUMO (top, transparent) surfaces are displayed as viewed above the π -symmetric orbitals, with opposite phases above and below the plane of the molecule. All orbital energies are presented in eV.

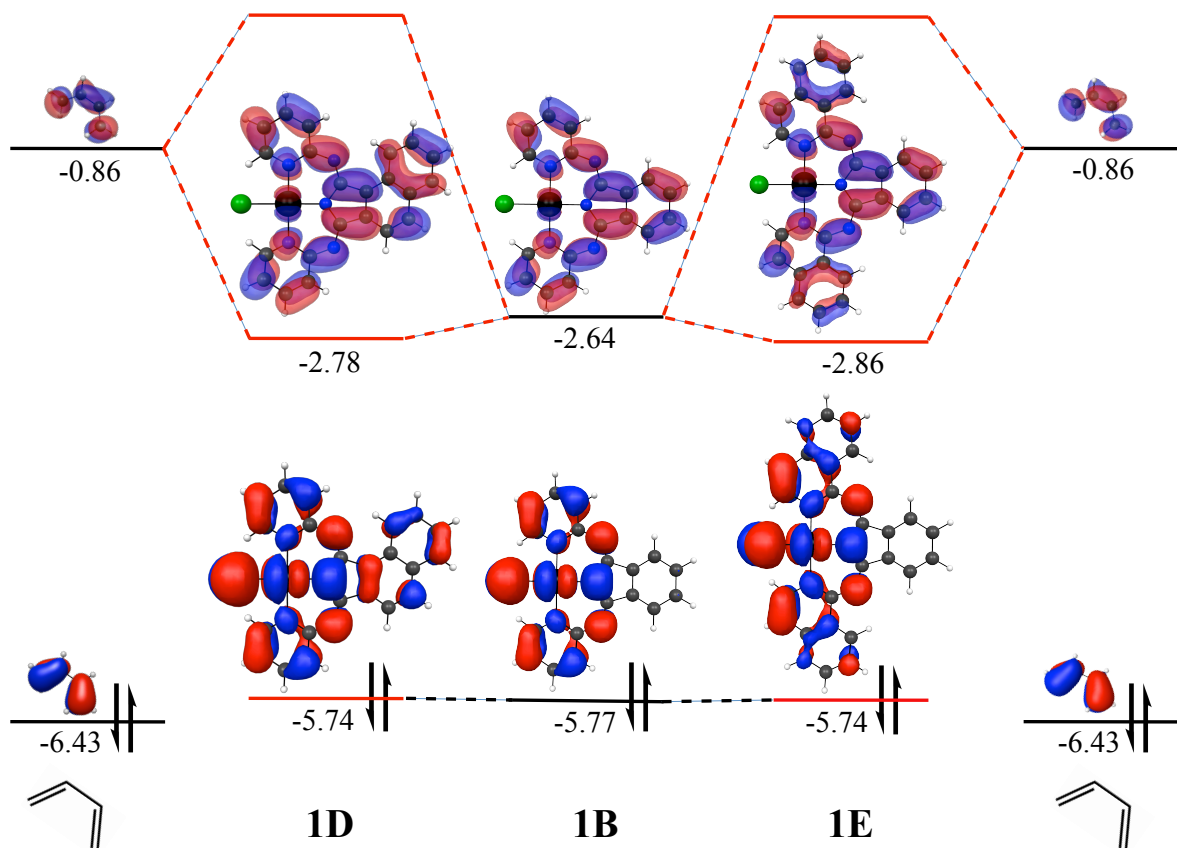


Figure 4: Series of substituted magnesium porphyrin substituted complexes.

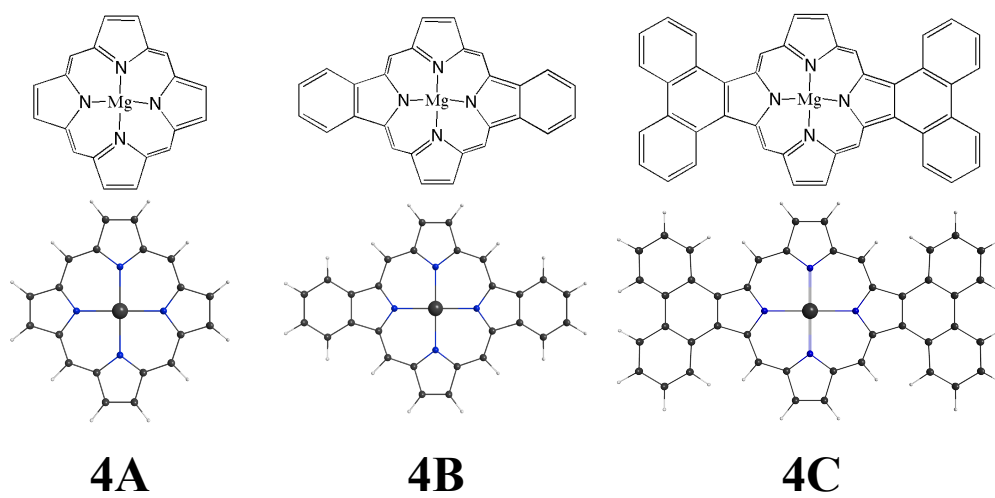


Table 1: TDDFT and TDA-TDDFT vertical excitation energies for gas phase and CPCM solvated complexes. The absolute difference between calculated and experimental transitions, reported in nm, is given in parentheses. HOMO/LUMO energies and the Kohn-Sham Shifts (HOMO-LUMO gap) for the gas phase and CPCM solvated complexes.

Structure	TDDFT		TDA-TDDFT		TDA-TDDFT		KS orbital energy (eV)		HOMO-LUMO energy difference (eV)
	vertical excitation energy nm (error) ^a		vertical excitation energy nm (error) ^a		HOMO→LUMO coefficient ^b	squared	HOMO	LUMO	
1A	541 (-)		566 (-)		0.87		-5.55	-2.78	2.78
1B	519 (32)		508 (21)		0.88		-5.55	-2.56	2.99
1C	498 (21)		488 (11)		0.88		-5.52	-2.45	3.07
1D	564 (35)		553 (24)		0.90		-5.52	-2.69	2.83
1E	575 (39)		564 (28)		0.85		-5.52	-2.78	2.75
CPCM-1A	541 (-)		525 (-)		0.86		-5.74	-2.83	2.91
CPCM-1B	489 (2)		478 (9)		0.87		-5.77	-2.64	3.13
CPCM-1C	472 (5)		462 (15)		0.89		-5.77	-2.56	3.21
CPCM-1D	533 (4)		522 (7)		0.88		-5.74	-2.78	2.96
CPCM-1E	540 (4)		527 (11)		0.85		-5.74	-2.86	2.88

^aerror relative to experimental solution phase (CH₂Cl₂) UV measurements for complexes **2-4**

^bcoefficients correspond to HOMO→LUMO transition

Table 2: TDDFT and TDA-TDDFT vertical excitation energies for gas phase and CPCM magnesium porphyrin complexes. The absolute difference between calculated and experimental transitions, reported in nm, is given in parentheses. HOMO/LUMO energies and the Kohn-Sham Shifts (HOMO-LUMO gap) for the gas phase and CPCM solvated complexes.

Structure	TDDFT vertical excitation energy (nm)	TDA-TDDFT vertical excitation energy (nm)	TDA-TDDFT coefficients ^a squared	KS orbital energy (eV)			HOMO-LUMO energy difference (eV)
				HOMO-1	HOMO	LUMO	
4A	523	508	0.50, 0.48	-5.11	-5.05	-2.07	2.98
4B	556	537	0.63, 0.36	-5.11	-4.80	-2.21	2.59
4C	556	544	0.49, 0.49	-5.12	-4.98	-2.25	2.73

^acoefficients correspond to transitions between the HOMO-1, HOMO, LUMO, LUMO+1

CHAPTER 6. SILICA MESOPOROUS MOLECULAR SIEVES AND THE FRAGMENT MOLECULAR ORBITAL METHOD

Luke Roskop, Dmitri G. Fedorov, and Mark S. Gordon

The fragment molecular orbital (FMO) method is applied to model systems that mimic amorphous silica nanopores. FMO-RHF (restricted Hartree-Fock) is shown to reliably approximate the RHF energy, the dipole moment, and the energy gradient. The application of the FMO method to mesoporous silica nanopores (MSNs) of the MCM-41 type is discussed and an error analysis is given. A fragmentation scheme for MSNs is illustrated to provide guidance for future applications of the FMO method to these systems.

1. Introduction

Mesoporous silica nanoparticles (MSNs)¹ promise to play an important role in heterogeneous catalysis, separations, sensing, drug delivery, imaging, and controlled release/sequestration.^{2,3,4,5} These potential applications benefit from the many unique properties of MSNs, which include high surface area ($>700 \text{ m}^2\text{g}^{-1}$), large pore volume ($>0.9 \text{ cm}^3\text{g}^{-1}$), good thermal stability, and low reactivity. Although MSNs are comprised of amorphous silica, at the mesoscopic level they are ordered into structures that are best described as hexagonal, cubic, or lamellar. For example: MCM-41 is a hexagonal array of uniform mesopores that have a tunable pore size ranging from 2-30 nm.

Applications of MSNs involve the functionalization of the interior surface of a mesopore with the appropriate chemical groups. These applications call for a comprehensive understanding of the interactions of functional groups among each other and the interior surface of the mesopore. The techniques of solid state nuclear magnetic resonance (NMR)^{6,7} and vibrational spectroscopy⁸ can indicate the proximity of functional groups to the interior

surface of the mesopore and other functional groups. Though these experimental methods are highly credible, computational models are frequently used to interpret experimental results. In addition, computational models are frequently designed from experimental insights.

There are not many reliable computational methods that can efficiently treat large molecular systems like MCM-41 ($>10^3$ atoms). Molecular mechanics (MM) is commonly used to treat large biological, condensed phase, or crystalline systems. On the other hand, MM methods do not allow for connectivity changes between atoms while a chemical system evolves. One model potential that treats both chemical reactivity and polarization effects is the reactive force field (ReaxFF).⁹ From distance dependent bond orders, ReaxFF is able to modify the connectivity between atoms “on the fly.” This enables ReaxFF to properly account for bond dissociation/formation while a reaction progresses.

The more sophisticated quantum mechanical (QM) methods allow chemical systems to be treated in a general manner that is free of empirically fitted parameters. Since QM methods become computationally prohibitive for systems comprised of large numbers of atoms (> 50 heavy atoms), it is common to examine only the chemically important region of a large molecular system.¹⁰ An Efficient QM treatment of large molecular systems usually employs a so-called fragmentation method. Over the years, much effort has been spent on development of various fragmentation methods.^{11,12,13,14,15} In particular, the fragment molecular orbital (FMO) method has shown great promise in applications that involve proteins, silicon nanowires, and zeolite cages.¹⁶

In the FMO method, one divides a chemical system into fragments, also called monomers. A modified Fock operator is constructed for each monomer, so that the Coulomb field that originates from all of the other monomers is incorporated into this monomer Fock

operator. Hartree-Fock equations are then solved in the usual iterative manner for each monomer. This level of theory is referred to as FMO1. To obtain more accurate energies and properties, one can explicitly include in the calculation all pairs of fragments (dimers). The dimer corrections are also computed in the Coulomb field of the remaining fragments, but the dimer calculations are not iterated to self-consistency. For even greater accuracy, one can include higher order corrections such as three-body (trimer) interactions in a similar manner. Equation 1 is used to determine the total energy of a system treated with FMO. In Eq. 1: E_I is the energy of monomer I, E_{IJ} is the energy of dimer IJ, and E_{IJK} is the energy of trimer IJK.

$$\begin{aligned}
 E^{\text{FMO}} = & \sum_I E_I + \sum_{I>J}^N (E_{IJ} - E_I - E_J) + \\
 & \sum_{I>J>K}^N [(E_{IJK} - E_I - E_J - E_K) - (E_{IJ} - E_I - E_J) - \\
 & (E_{JK} - E_J - E_K) - (E_{KI} - E_K - E_I)] + \dots
 \end{aligned} \tag{1}$$

This paper examines the suitability of the fragment molecular orbital method (FMO) for the study of MSN materials of the MCM-41 type. In the FMO method, the bonds that interconnect monomers are detached, and subsequently frozen in the SCF calculation. The FMO adaptive frozen orbital (AFO)¹⁶ bond detachment scheme, which was designed to describe solids and surfaces, is used here to detach bonds between monomers. In the AFO scheme, a bond detached atom (BDA) and bond attached atom (BAA) are defined to specify which of the monomers retains the detached bond in their model space. A useful approach for fragmenting MSNs is suggested, and its performance is examined.

2. Method

The FMO method is used to examine four isomers that are intended to mimic a portion of a single MSN mesopore that is consistent with the MCM-41 morphology. Each isomer (A, B, C and D) in Figure 1 is functionalized with four (pentafluorophenyl)propyl substituents (Figure 2) and comprised of 1770 atoms ($\text{Si}_{392}\text{O}_{954}\text{C}_{36}\text{F}_{20}\text{H}_{368}$) in which each isomer differs by the arrangement of the substituents. Each isomer was fully optimized with molecular mechanics using the MM3 force field parameters¹⁷ in the Tinker program.¹⁸ In Figure 1, the various colors that label different regions of each structure indicate each of the monomers if the system were fragmented into 32 monomers. Each model has a pore diameter of $\sim 28\text{\AA}$ (which is consistent with the experimental parameters) and a pore length of $\sim 17.5\text{\AA}$ (farthest heavy-heavy atom distance along interior surface of the pore). All dangling bonds are terminated with hydroxide groups since a truncated pore structure is used.

In the case of separating a Si-O bond that connects two monomers that are part of the silica pore structure, the O atom is assigned as the bond attached atom (BAA) and the Si atom is assigned as the bond detached atom (BDA). Fragmentation schemes for each of the four systems are shown in Figure 3 with each monomer indicated by a different color. Models A-D were fragmented into 32, 30, 26, and 14 monomers. To study the effects of placing two fragmented bonds close to one another, two different approaches are used in the 14 monomer model, referred to as 14a and 14s. The 14a scheme corresponds to an aligned arrangement of bond detached atoms (BDAs) and bond attached atoms (BAAs) while the 14s scheme was designed to stagger the BAAs and BDAs (Figure 4). The average number of atoms/monomer in structures A-D for fragmentation schemes 14a/s, 26, 30 and 32 are 126, 68, 59, and 55 atoms, respectively.

FMO properties are computed for FMO2 (including up to dimer corrections) and FMO3 (including up to trimer corrections) at the restricted Hartee-Fock (RHF) level of theory. FMO and full RHF (un-fragmented system) gradient computations are performed using the STO-3G basis set.¹⁹ The FMO energy, dipole moment, and energy gradient are compared to the full RHF results. The AFO method is used to construct all inter-fragment bonds.

Since the FMO method divides a large chemical system into smaller, more manageable monomers, the chemical bonds that interconnect monomers must be carefully considered. The AFO method is used to construct the chemical bonds that interconnect monomers. The AFO method constructs bonding orbitals that interconnect monomers from model systems that include both the BDA and BAA. The detached bond orbitals are extracted from the localized orbitals of these model systems and consequently frozen in FMO calculations. The size of the AFO model systems was varied to understand the effects on FMO properties. Both a small and large AFO model system was used. The small model system ($\text{H}_3\text{Si-OH}$) contains just the BDA (Si) and BAA (O), which were capped with hydrogen atoms oriented in the direction of the atoms previously bonded to the BDA and BAA. The large model system $[(\text{OH})_3\text{Si-O}(\text{SiH}_3)_3]$ incorporates the nearest neighbors to the BDA and BAA, the nearest neighbor atoms are similarly capped with hydrogen atoms.

The performance of FMO2-RHF and FMO3-RHF is compared to the full RHF computation. More specifically, the error in the FMO total energy, dipole moment, and gradient are compared with the RHF results. In Equations 2-5, n refers to the FMO n level (i.e. FMO2), $E^{\text{FMO}n\text{-RHF}} (E^{\text{RHF}})$ is the FMO n -RHF (RHF) energy, $\mathbf{d}_n^{\text{FMO}n\text{-RHF}} (\mathbf{d}^{\text{RHF}})$ is the FMO n -RHF (RHF) dipole vector, and $\nabla E^{\text{FMO}n\text{-RHF}} (\nabla E^{\text{RHF}})$ is the FMO n -RHF (RHF) energy

gradient. ΔE_n represents the error in energy at FMO level n , d_n^{RMS} represents the error in dipole moment at FMO level n , ΔG_n^{RMS} represent the RMS error in the gradient at FMO level n , and ΔG_n^{MAX} represents the maximum error in the gradient at FMO level n .

$$\Delta E_n = E^{\text{FMO}n\text{-RHF}} - E^{\text{RHF}} \quad (2)$$

$$d_n^{\text{RMS}} = \sqrt{\frac{|\mathbf{d}_n^{\text{FMO}n\text{-RHF}} - \mathbf{d}^{\text{RHF}}|^2}{3}} \quad (3)$$

$$\Delta G_n^{\text{RMS}} = \sqrt{\frac{|\nabla E^{\text{FMO}n\text{-RHF}} - \nabla E^{\text{RHF}}|}{3N_{\text{atoms}}}} \quad (4)$$

$$\Delta G_n^{\text{MAX}} = \max(|\nabla E^{\text{FMO}n\text{-RHF}} - \nabla E^{\text{RHF}}|) \quad (5)$$

3. Results and discussion

Table 1 presents the average errors in the energy, the dipole moment, and the gradient among structures A-D. The FMO2 average energy errors are not noticeably affected whether a large or small model system is used to construct the AFOs. The errors in the FMO2 energies depend on the size (or number) of monomers. At the FMO2 level, a systematic decrease in the energy errors is seen going from the largest number of monomers (~225 kcal/mol) to smallest number of monomers (~40 kcal/mol). FMO3 exhibits much smaller energy errors than FMO2. With respect to the various fragmentation schemes, the FMO3 average energy errors have a maximum absolute error of 5.4 kcal/mol and a minimum absolute error of 0.1 kcal/mol. The much smaller errors for FMO3 than for FMO2 clearly indicates that three-body effects are very important in MSN species. From Table 1 it is seen

that the energy errors at the FMO3 level are only slightly sensitive to the fragmentation scheme.

Similar to the average error in the energy, the average error in the dipole moment shows a systematic decrease as the number of monomers decrease (and the cost of the computation increases). The size of the model system used to construct the AFOs also influences the average error in the dipole moment. The average errors in both the FMO2 and FMO3 dipole moments are the smallest when a large model system is used to construct the AFOs.

The FMO3 average ΔG_n^{MAX} and ΔG_n^{RMS} errors are smaller than the FMO2 gradient errors. Using a smaller number of fragments tends to decrease the average gradient errors, since the system is less fragmented. The FMO2 and FMO3 gradients have the smallest errors when large model systems are used to construct the AFOs.

Although the average energy errors among A, B, C and D decrease for FMO3 relative to FMO2, the energy differences among the isomers are also important. Table 2 shows isomerization energies among models B-D compared to model A. From Table 2 it is immediately seen that FMO3 outperforms FMO2, regardless of the number of monomers. The largest FMO3 isomerization error is ~12 kcal/mol for model C when the fragmentation schemes are comprised of 32, 30, or 26 monomers. The agreement for 14 monomers is essentially perfect.

FMO2 overestimates isomerization energies by ~10-50 kcal/mol for all systems that are configured with 32, 30 and 26 monomers, regardless of the size of model space used to construct the AFOs. The most accurate FMO3 isomerization energies are attained when the

smallest number of monomers (scheme 14a/s) is used (errors < 1 kcal/mol). The staggered (14s) and aligned (14a) arrangements of BAAs and BDAs give rise to similar errors.

4. Conclusions

The FMO method has been applied to mesoporous silica nanoparticles (MSN) that mimic a small section of a mesopore consistent with the MCM-41 morphology. As the FMO level is increased from FMO2 to FMO3, the energy, the dipole moment, and the energy gradients approach the full RHF values. The size of the model system used to construct the AFOs does not affect the structural energies, but the AFO model size does affect the errors in the dipole moment and the energy gradients. Both FMO2 and FMO3 calculations that employ AFOs constructed from a large model systems show less error in the dipole moment and the energy gradient than AFOs constructed with small model systems.

Out of all the fragmentation schemes discussed here, the approach that uses the fewest number of monomers (14a/s) has the smallest errors. FMO3 is necessary to achieve results that are comparable to RHF. It is suggested here that using basis sets larger than STO-3G to study MSNs would result in properties close to the full RHF properties.

Acknowledgements

This work was supported by a grant from the Air Force Office of Scientific Research.

References

- ¹J. S. Beck, J. C. Vartuli, W. J. Roth, M. E. Leonowicz, C. T. Kresge, K. D. Schmitt, C. T. W. Chu, D. H. Olson, E. W. Sheppard, S. B. McCullen, J. B. Higgins, J. L. Schlenker, *JACS* **114**, 10834 (1992). C. T. Kresge, M. E. Leonowicz, W. J. Roth, J. C. Vartuli, J. S. Beckm *Nature* **359**, 710 (1992)

- ²H.-T. Chen, S. Huh, J. W. Wiench, M. Pruski, C. S.-Y. Lin, JACS **127**, 13305 (2005). S. Huh, H.-T. Chen, J. W. Wiench, M. Pruski, V. S.-Y. Lin, Angew. Chem., Int. Ed. **127**, 1826 (2005). S. Huh, H.-T. Chen, J. W. Wiench, M. Pruski, V. S.-T. Lin, JACS **126**, 1010 (2004).
- ³Z. Mehraban, F. Farzaneh, Microporous Mesoporous Mater. **88**, 84 (2006). Y. X. Zhao, M. Y. Ding, D. P. Chen, Anal. Chim. Acta. **542**, 193 (2005).
- ⁴V. S.-T. Lin, C.-Y. Lai, K. Huang, S.-A. Song, S. Xu JACS **123**, 11510 (2001). D. R. Radu, C.-Y. Lai, K. Jeftinija, E. W. Rowe, D. Jeftinija, V. S.-Y. Lin JACS **126**, 13216 (2004).
- ⁵C.-Y. Lai, D. G. Trewyn, D. M. Jeftinija, K. Jeftinija, S. Xu, S. Jeftinija, V. S.-Y. Lin, JACS **125**, 4451, (2003). N. K. Mal, M. Fujiwara, Y. Tanaka, Nat. (Lond.) **421**, 350 (2003). T. D. Nguyen, H.-R. Tseng, P. C. Celestre, A. H. Flood, Y. Liu, J. F. Stoddart, J. I. Zink, Natl. Acad. Sci. USA **102**, 10029 (2005). B. G. Trewyn, C. M. Whitman, V. S.-Y. Lin, Nano Lett. **4**, 2139 (2004). M. Vallet-Regi, A. Ramila, R. P. del Real, J. Perez-Pariente, Chem. Mater. **13**, 308 (2001). S. Giri, B. G. Trewyn, M. P. Stellmaker, V. S.-T. Lin, Angew. Chem., Int. Ed. **44**, 5038 (2005). A. Ramila, B. Munoz, J. Perez-Pariente, M. J. Vallet-Regi, Sol-Gel Sci. Technol. **26**, 1199 (2003).
- ⁶K. Mao, T. Kobayashi, J. W. Wiench, H.-T. Chen, C.-H. Tsai, V. S.-Y. Lin, M. Pruski, JACS **132**, 12452 (2010). J. Trebosc, J. W. Wiench, S. Huh, V. S.-Y. Lin, M. Pruski, JACS **127**, 3057 (2005). J. Trebosc, J. W. Wiench, S. Huh, V. S.-Y. Lin, M. Pruski, JACS **127**, 7587 (2005).
- ⁷J. Wang, N. Yu, A. Zheng, J. Yang, D. Wu, Y. Sun, C. Ye, F. Deng Microporous and Mesoporous Materials **89**, 219 (2006).
- ⁸G. Tabacchi, E. Gianotti, E. Fois, G. Martra, L. Marchese, S. Coluccia, A. Gamba J. Chem. Phys. A **111**, 4946 (2007).

- ⁹A. C. T. van Duin, S. Dasgupta, F. Lorant, W. A. Goddard, *J. Phys. Chem. A* **105**, 9396 (2001).
- ¹⁰D. Zorn, V. S.-Y. Lin, M. Pruski, M. S. Gordon, *J. Chem. Phys. A* **112**, 10635 (2008).
- ¹¹J. Gao, *J. Phys. Chem. B* **101**, 657 (1997). J. Gao, *J. Chem. Phys.* **109**, 2346 (1998). W. Xie, and J. Gao, *J. Chem. Theory Comput.* **3**, 1890 (2007).
- ¹²W. Yang, T.-S. Lee, *J. Chem. Phys.* **103**, 5674 (1995). T. Akama, M. Kobayashi, H. Nakai *J. Comput. Chem.* **28**, 2003 (2007). T. Akama, A. Fujii, M. Kobayashi, H. Nakai, *Mol. Phys.* **105**, 2799 (2007).
- ¹³V. Deev, M. A. Collins, *J. Chem. Phys.* **122**, 154102 (2005). M. A. Collins, V. A. Deev, *J. Chem. Phys.* **125**, 104104 (2006). M. A. Collins, *J. Chem. Phys.* **127**, 024104 (2007).
- ¹⁴D. W. Zhang, J. Z. H. Zhang, *J. Chem. Phys.* **119**, 3599 (2003).
- ¹⁵S. R. Gadre, R. N. Shirsat, A. C. Limaye, *J. Phys. Chem.* **98**, 9165 (1994).
- ¹⁶K. Kitaura, E. Ikeo, T. Asada, T. Nakano, M. Uebayasi, *Chem. Phys. Lett.* **313**, 701 (1999). D.G. Fedorov, K. Kitaura, *J. Chem. Phys.* **120**, 6832 (2004). D. G. Fedorov, K. Kitaura, *J. Phys. Chem. A* **111**, 6904 (2007). D. G. Fedorov, K. Kitaura, in: E. B. Starikov, J. P. Lewis, S. Tanaka (Eds.), *Modern Methods for Theoretical Physical Chemistry and Biopolymers*, Elsevier, Amsterdam, 2006, p. 3. D. G. Fedorov, D. G. Federov, J. H. Jensen, R. C. Deka, K. Kitaura, *J. Phys. Chem. A* **112**, 11808 (2008). P. V. Avramov, J. H. Jensen, K. Kitaura, *Chem. Phys. Lett.* **477**, 169 (2009). D. G. Fedorov, K. Kitaura (Eds.), *The Fragment Molecular Orbital Method: Practical Applications to Large Molecular Systems*, CRC Press, Boca Raton, FL, 2009.
- ¹⁷J. H. Lii, N. L. Allinger, *JACS* **111**, 8566 (1989). J. H. Lii, N. L. Allinger, *JACS* **111**, 8576 (1989). N. L. Allinger, Y. H. Yuh, J. H. Lii, *JACS* **111**, 8551 (1989).

¹⁸C. E. Kundrot, J. W. Ponder, F. M. Richards, J. Comput. Chem **12**, 402 (1991). J. W. Ponder, F. M. Richards, J. Comput. Chem **8**, 1016 (1987).

¹⁹W. J. Hehre, R. F. Stewart, J. A. Pople, J. Chem Phys. **51**, 2657 (1969). W. J. Hehre, R. Ditchfield, R. F. Stewart, J. A. Pople, J. Chem. Phys. **52**, 2769 (1970).

Table 1: Error analysis^a for the fragmentation at the FMO2-RHF and FMO3-RHF level. Errors are averaged over models C1-C4 defined by Figure 1.

AFO Model	Large	Large	Large	Small	Small	Small	Small	Small
# monomers	26	14a	14s	32	30	26	14a	14s
ΔE_2	226.0	49.9	43.1	241.1	230.5	223.1	48.9	41.4
ΔE_3	3.1	-0.2	-0.2	5.0	4.9	5.4	-0.3	-0.1
Δd_2^{RMS}	1.0	0.5	0.5	3.0	2.8	2.7	1.2	0.6
Δd_3^{RMS}	0.6	0.2	0.3	1.4	1.1	1.3	0.5	0.5
ΔG_2^{MAX}	6.6	5.7	5.6	6.8	6.8	6.9	5.7	5.6
ΔG_3^{MAX}	3.2	1.4	1.6	4.8	4.8	4.8	2.1	1.8
ΔG_2^{RMS}	1.2	0.5	0.5	1.5	1.4	1.4	0.5	0.5
ΔG_3^{RMS}	0.5	0.2	0.2	0.7	0.7	0.7	0.3	0.3

^aIn energy ΔE_n (kcal/mol), dipole moment Δd_n^{RMS} (debye), and gradient ΔG_n^{MAX} and ΔG_n^{RMS} (10^{-3} au/bohr).

Table 2: Isomer energies (kcal/mol) of structures B, C, and D relative to structure A for the various fragmentation schemes seen in Figure 3. Both small and large model systems were used to construct the AFOs.

AFO Model # monomers	Small 32	Small 30	Small 26	Large 26	Small 14a	Large 14a	Small 14s	Large 14s	Full RHF
B(FMO2)	43.9	37.0	33.0	52.2	2.9	6.1	-4.5	-2.6	-14.1
B(FMO3)	-13.3	-13.6	-13.6	-14.0	-14.3	-14.3	-14.1	-14.3	
C(FMO2)	70.1	58.7	51.1	43.4	34.5	35.9	38.4	40.1	29.3
C(FMO3)	41.7	41.9	42.1	41.3	29.1	29.5	29.5	29.4	
D(FMO2)	142.4	137.3	133.8	127.6	98.5	99.5	102.8	103.3	91.4
D(FMO3)	95.2	95.1	95.3	95.9	91.0	91.2	91.4	91.2	

Figure 1: Models C1-C4 are four MSN isomers ($\text{Si}_{392}\text{O}_{954}\text{C}_{36}\text{F}_{20}\text{H}_{368}$) whose interior is substituted with four (pentafluorophenyl)propyl functional groups (highlighted for clarity).

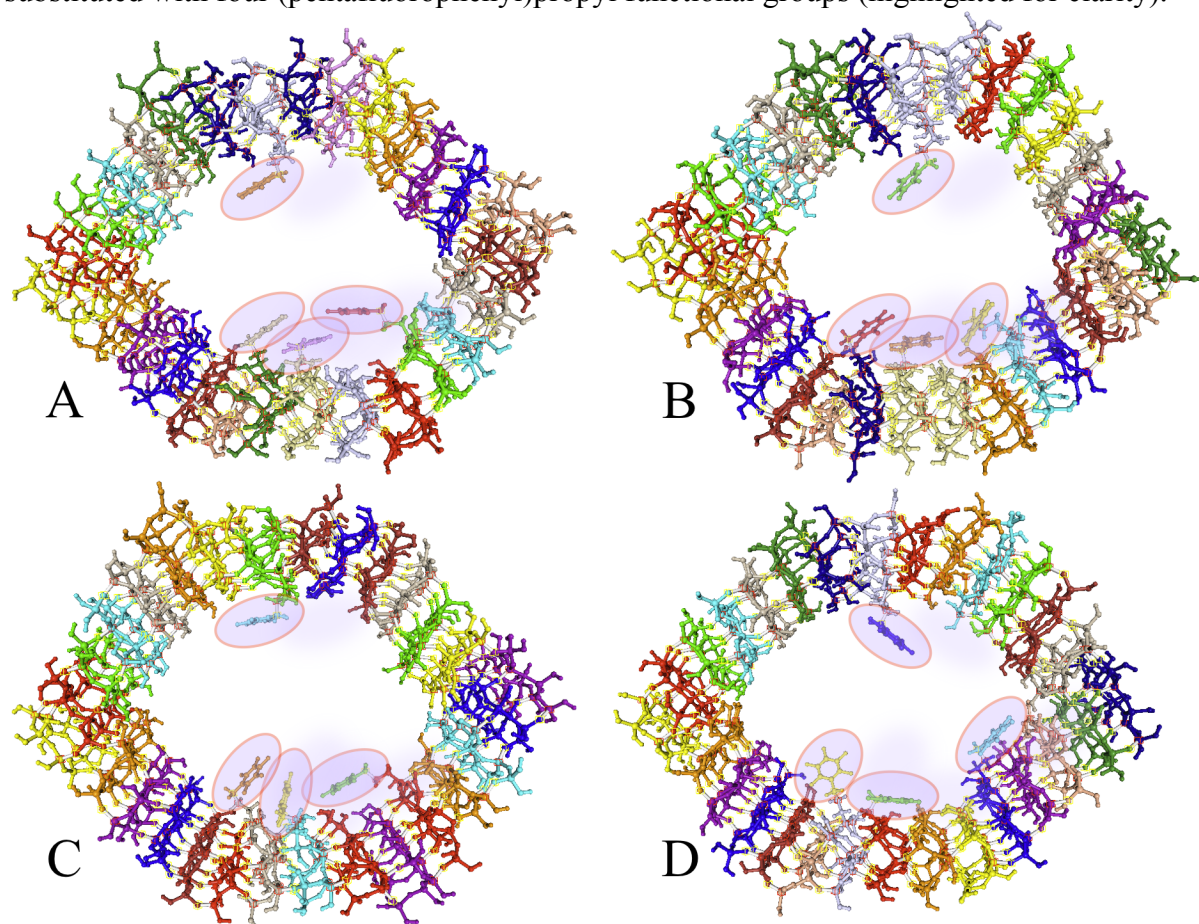


Figure 2: Schematic representation of a hydroxylated MSN pore functionalized with (pentafluorophenyl)propyl substituents.

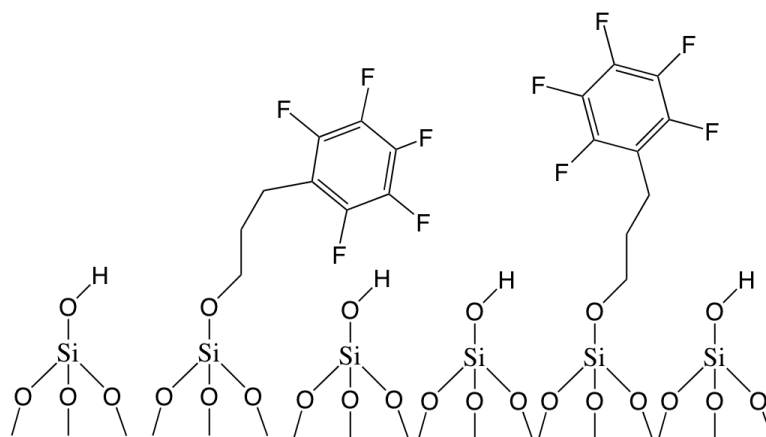


Figure 3: Four fragmentation schemes used for Models A, B, C, and D. A-D are fragmented into 32, 30, 26, or 14 monomers. Each monomer is numbered.

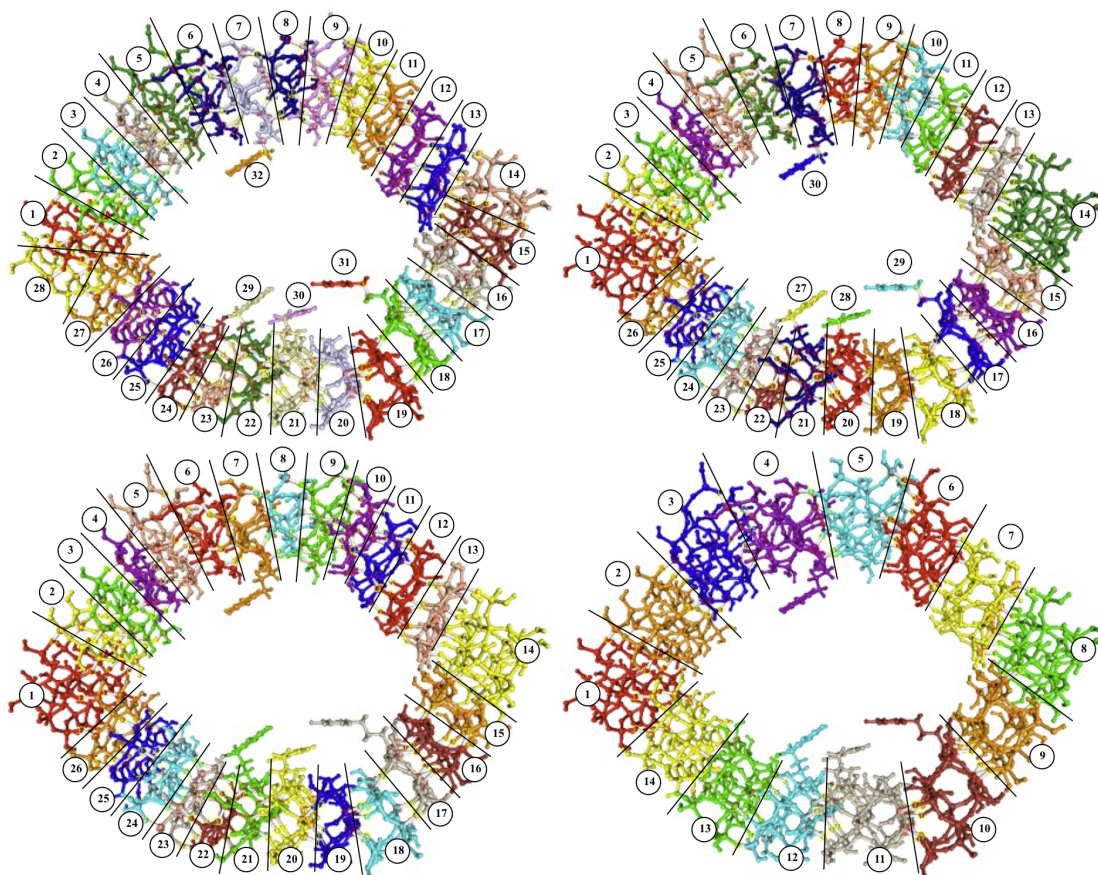
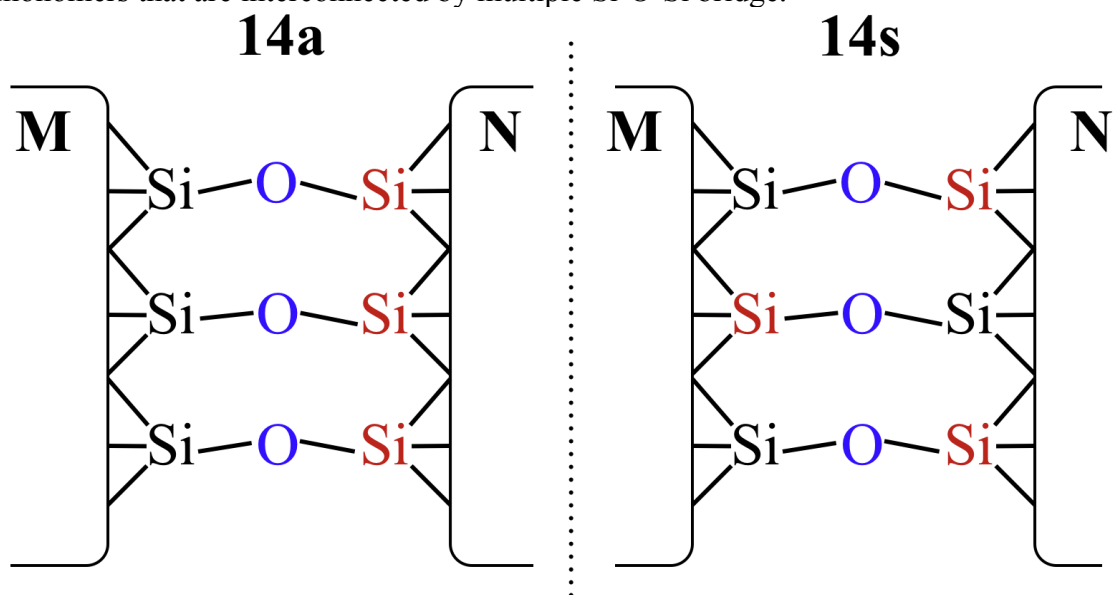


Figure 4: Aligned (14a) vs staggered (14s) arrangement of bond-detached atoms (BDA - red color) and bond-attached atoms (BAA - blue color). M and N refer to monomers that are interconnected by multiple Si-O-Si bridge.



CHAPTER 7. GENERAL CONCLUSIONS

In chapter 2, several Si(100) cluster models were investigated using several MCSCF methods, including full CASSCF, various ORMAS approximations, and GVB-PP. It has been systematically demonstrated that ORMAS determines properties (e.g., bond distances, vibrational frequencies, and natural orbital occupation numbers) for large Si(100) surface clusters that are in excellent agreement with those obtained with full CASSCF. When the CASSCF reference is unavailable, ORMAS properties agree with trends established for smaller, more computationally manageable systems (similar NOON values and dimer bond lengths). When only (2,2) subspaces are considered, ORMAS and GVB-PP are in close agreement with each other. As one would expect, the use of larger ORMAS subspaces (which are often necessary) can significantly reduce the error relative to a full CASSCF calculation, while the GVB-PP error remains larger.

Based on the systems examined, it appears that the Si(100) surface is symmetric in the ground state; however, the calculations reported here do not include dynamic correlation. It is unlikely that larger cluster models at the CASSCF level of theory will cause buckling of the surface dimers via inter-dimer interactions. The success of the ORMAS approach suggests that the distances between dimers is simply too large to allow inter-dimer interactions that are large enough to qualitatively alter the results presented here. This large inter-dimer distance is responsible for the negligible contributions from the excitations between dimers in ORMAS MCSCF wavefunctions. It is likely that only subspaces that contain overlapping orbitals would require electronic excitations between them.

The discrepancy between buckling mode frequencies for ORMAS partitioning

Schemes 2 and 3 indicate that reliable ORMAS Hessians require CI contributions from determinants corresponding to excitations between σ and π orbitals. This observation should be carefully considered when implementing ORMAS in mechanistic studies involving Si(100).

In general, developing an ORMAS may not be as clear-cut as it is for Si(100). For more complex systems, reliable ORMAS calculations will undoubtedly rely on chemical intuition and validation through preliminary tests. For example, a suitable ORMAS for atomic diffusion of Ga on Si(100) will incorporate dimer orbitals that are strongly interacting with Ga orbitals into the same orbital subspace. Orbitals from spectator dimers will remain in separate subspaces since their interaction with the “action region” is less significant.

In chapter 3, a quasi-degenerate perturbation theory based on the ORMAS reference wavefunction has been described. For a complete active space MRPT, the effective Hamiltonian considers singly and doubly excited configurations, into the external orbital space of the MCSCF. For ORMAS-PT, the effective Hamiltonian was reformulated to also include internally excited configurations (IECs). A scheme was presented that directly enumerates the IECs to allow for efficient computation of the IECs contributions to the energy and wavefunction. The ORMAS-PT method has been applied to four different systems, with the following key conclusions:

- 1) For the two lowest $^1\Sigma^+$ states of LiF, ORMAS-PT reproduces the MCQDPT avoided crossing between the two state-averaged potential energy surfaces. The energy splitting between the two states shows the largest error for LiF bond lengths less than the equilibrium distance. Starting from the LiF equilibrium bond distance and longer, the energy splitting showed an error less than 0.2 kcal/mol along the reaction coordinate to the

dissociated products.

2) ORMAS-PT correctly reproduces the MRMP potential energy surface along the symmetric and anti-symmetric dimer buckling modes for a $\text{Si}_{15}\text{H}_{16}$ cluster. As the $\text{Si}_{15}\text{H}_{16}$ cluster geometry is perturbed along the symmetric and anti-symmetric buckling modes, the energy increases at both the ORMAS-PT and MRMP levels of theory. This indicates the symmetric structure is the global minimum.

3) ORMAS-PT was applied to the oxoMn(salen) species to examine its performance with transition metal complexes. ORMAS-PT reproduces the MRMP neutral singlet-triplet energy splitting and anionic doublet-quartet energy splitting with errors less than 0.6 kcal/mol.

4) ORMAS-PT reproduces the MRMP ionization potentials for *trans*-polyacetylene polymers of various lengths. For the longer polymers, ORMAS-PT was shown to systematically converge to the MRMP results as the number of configurations used to construct the reference wavefunctions is systematically increased.

ORMAS-PT is an efficient approximation to the MRMP/MCQDPT level of theory. ORMAS-PT is able to attain a high level accuracy and reduce the number of determinants required for a typical MRMP/MCQDPT by 1-2 orders of magnitude. It follows that ORMAS-PT reduces the system memory needed to handle large active spaces. The highly efficient ORMAS-PT approach opens the door for MRPT treatments of highly correlated systems that are otherwise computationally prohibited by CASSCF/FORS references.

In chapter 4, *Ab initio* electronic structure calculations were performed to develop an understanding of the diffusion of Ga and Ga_2 on the Si(100)-2x1 reconstructed surface.

These processes were modeled using QM ($\text{Si}_{15}\text{H}_{16}$) and SIMOMM QM/MM ($\text{Si}_{199}\text{H}_{92}$)

molecular clusters. The diffusion of Ga adatoms and the Ga₂ dimer along the Si(100) dimer row was investigated.

Structures similar to the ones found by Takeuchi and AHPC were observed in this work, with differences primarily in the energy ordering among the structures. Both Takeuchi and AHPC reported the off-center structure as a minimum energy structure, but in the present work the off-center structure is found to be a transition state by both the QM and QM/MM cluster models. Both Takeuchi and AHPC predicted that the off-center structure is the global minimum; here the three-fold structure is found to be the QM minimum while the on-dimer structure is predicted to be the QM/MM minimum. AHPC predict that the on-dimer structure is a transition state, which agrees with the QM cluster model used here. On the other hand, the QM/MM cluster model predicts the on-dimer site to be a minimum energy structure. In any event, the low MRMP2 relative energies from both the QM and QM/MM models would seem to indicate that the on-dimer site is a minimum on the potential energy surface.

The order of stability for structures that are common to both QM and QM/MM models is inconsistent. QM/MM energies predict that the 3-4B structure is the singlet global minimum. No QM/MM energy barriers were found for structures that lead to the 3-4B structure. This indicates Ga adatoms self-assemble into atomic wires, consistent with experimental observations. On the other hand, MRMP2//CASSCF relative energies indicate an energy penalty in the QM-only cluster as the Ga₂ dimer is rotated from the 5-4B position to the 3-4B position. This demonstrates the need for surface models that consider bulk effects.

The doublet/quartet surfaces that depict Ga adatom diffusion indicate the QM-only on-dimer sites are transition states while the QM/MM model indicates they are minima. In

addition, the QM-only and QM/MM geometries have noticeable differences, because the QM cluster does not have sufficient structural rigidity. Compared to the SIMOMM model, the QM structures in which a Ga adatom or a Ga₂ dimer span more than one surface dimer have the largest distortions in geometries.

Some aspects of the QM-only and QM/MM potential energy surfaces are in qualitative agreement. Relative energies for structures in which Ga adatoms are separated appear to be insensitive to the presence of bulk MM atoms. Both the QM and QM/MM models demonstrate that pairs of Ga adatoms spontaneously form a Ga₂ dimer when they approach one another. Both models also predict that a Ga adatom freely diffuses along the dimer row.

In both QM and QM/MM models, the most energetically stable structures correlate with small diradical (i.e., nearly closed shell) character. These structures correspond to arrangements of Ga adatoms or Ga₂ dimer that maximize the interaction with the dangling dimer bonds. In addition, the formation of the Ga₂ dimer bond surely plays an important role in the stabilization of the surface clusters investigated here.

In chapter 5, three criteria were presented as guidelines to validate KS orbital interpretations in excited state chemistry:

- 1) The TDA-TDDFT properties, particularly the excitation energy, must be in good agreement with the full TDDFT method*
- 2) If criterion 1 is satisfied and if there is a dominant TDA-TDDFT coefficient (e.g., $X_{i \rightarrow a} > |0.9|$), then the excited state may be interpreted in terms of the corresponding excitation $i \rightarrow a$.*
- 3) The spectrum predicted by TDDFT and TDA-TDDFT must be in good agreement with experiment.*

Since KS orbitals are not physical observables, the use of KS orbitals in the interpretation of photochemical behavior must be carefully considered. Like CIS, TDA-TDDFT coefficients can clearly indicate which orbital pairs contribute to a particular excited state transition.

For the platinum(II) complexes, the TDA-TDDFT predictions of the lowest absorption energies were in agreement the TDDFT absorption frequencies (criterion #1). The lowest energy transitions for the series of platinum(II) complexes were shown to be dominated by a single excitation (HOMO→LUMO) (criterion #2). Both the TDA-TDDFT and TDDFT calculated absorption energies of the platinum(II) complexes are in agreement with experimental measurements (criterion #3). Since all three criteria were satisfied for the platinum(II) complexes, a Kohn-Sham orbital interpretation of the absorption trend is valid and shown to successfully predict the trend in absorption energies. Conversely, a series of Mg-porphyrins was shown to have double excitation character. Thus, the series of Mg-porphyrin systems does not satisfy criterion #2 for an orbital interpretation of the absorption trends.

In chapter 6, the FMO method was been applied to mesoporous silica nanoparticles (MSN) that mimic a small section of a mesopore consistent with the MCM-41 morphology. As the FMO level is increased from FMO2 to FMO3, the energy, the dipole moment, and the energy gradients approach the full RHF values. The size of the model system used to construct the AFOs does not affect the structural energies, but the AFO model size does affect the errors in the dipole moment and the energy gradients. Both FMO2 and FMO3 calculations that employ AFOs constructed from a large model systems show less error in the dipole moment and the energy gradient than AFOs constructed with small model systems.

Out of all the fragmentation schemes discussed here, the approach that uses the fewest number of monomers (14a/s) has the smallest errors. FMO3 is necessary to achieve results that are comparable to RHF. It is suggested here that using basis sets larger than STO-3G to study MSNs would result in properties close to the full RHF properties.